Janus-type and Molecular MOF-based composites

Abraham Ayala Hernández

Universitat Autònoma de Barcelona

Janus-type and Molecular MOF-based composites

Abraham Ayala Hernández

Tesis Doctoral

Doctorat en Química

Directors de la Tesi:

Prof. Dr. Daniel Maspoch

Dr. Inhar Imaz

Institut Català de Nanociència i Nanotecnologia (ICN2)

Departament de Química. Facultad de Ciències.

2017

Memoria presentada per aspirar al Grau de Doctor per Abraham Ayala Hernández.

Vist-i-plau.

Abraham Ayala Hernández

Prof. Dr. Daniel Maspoch
Investigador ICREA.
Supremolecular Nanochemistry and Materials Group.
Institut Catalá de Nanociencia i Nanotecnología (ICN2).

Dr. Inhar Imaz
Investigador Ramon y Cajal
Supremolecular Nanochemistry and Materials Group.
Institut Catalá de Nanociencia i Nanotecnología (ICN2).

Bellaterra, 30 de octubre de 2017

Table of contents

Abstract

The present Thesis has been dedicated to the study, development, and implementations of new methodologies synthesize Metal Organic Frameworks (MOFs) based multifunctional composites. Accordingly, two main lines of work can be distinguished through the lecture of this Thesis: i) the synthesis of Janus metal@MOFs particles and their partial functionalization for applications in removal of heavy metal ions, application in self-propelled and fluorescence; ii) the incorporation of active molecules into the MOFs through of creating controlled defects, and the use of the resulting composites in the removal of heavy metal ions.

In the Chapter 1, we review the evolution of the field of the MOFs including a brief historical introduction and the presentation of the main synthetic routes, properties and applications. We pay special attention to the current methodologies to synthesis MOFs and their miniaturization and their improvements of their properties and their possible applications. We mention the importance of the possibilities as well to create MOF composites combining the intrinsic properties of MOFs and other functional materials (*i.e.* magnetic materials, fluorescence, catalytic).

In Chapter 2, cites the general and specific objectives of this PhD Thesis.

Chapter 3 describes the methodology used for the synthesis of Janus metallic@MOFs particles. This methodology is based on the selective evaporation of metallic components on the MOFs surfaces and is carried out in different steps: i) synthesis of MOFs and their control size; ii) fabrication of MOFs monolayers on surfaces through the controlled deposition based on solvent evaporation; iii) evaporation of metal components through the electron bean evaporation technique, iv) detachment of the MOFs from the surfaces obtaining the Janus metallic@MOFs nanoparticles. The versatility of this methodology has allowed us to synthesis different MOF based composites, and in addition, we present the magnetic, fluorescence and catalytic properties that were evaluated in different Janus metallic@MOFs nanoparticles.

In chapter 4, we explored another kind of composites based on the combination of MOFs and organic functional molecules. We studied the incorporation of functional molecules into the MOFs creating defects into the network of the MOFs. In particular, we evaluated the incorporating of Xylenol Orange (XO) that has coordinative carboxylic groups and a strong capacity to chelate heavy metal ions. We studied the mechanism of the integration of XO into the MOF and their influence on the formation of the MOF, and in addition, we evaluated the final properties and specially the capacity to remove heavy metal ions.

Resumen

La presente Tesis está enfocada al estudio, desarrollo e implementación de nuevas metodologías de síntesis de estructuras metal-orgánicas (MOFs) basadas en compuestos multifuncionales. El trabajo de investigación de esta Tesis se desarrolló en dos líneas de investigación: i) por un lado, la síntesis de partículas metálicas Janus con MOFs y su funcionalización parcial para aplicaciones en eliminación de metales pesados, aplicaciones de auto movilidad y fluorescencia, ii) por otro lado la incorporación de moléculas activas en MOFs a través de la creación controlada de defectos, estudiando la formación del MOF así como su posible aplicación en eliminación de metales pesados

En el capítulo uno, nosotros revisamos la evolución en el campo de los MOFs a partir de un desarrollo histórico, y la presentación de las principales estrategias de síntesis, así como las propiedades y aplicaciones. También, nosotros presentamos especial atención en las metodologías actuales para la miniaturización de MOFs, las mejoras en las propiedades y posibles aplicaciones. También mencionamos la importancia de las posibilidades de crear compuestos de MOF combinando las propiedades intrínsecas de MOFs y otros materiales funcionales, por ejemplo, materiales magnéticos, materiales fluorescentes y catalíticos.

En el capítulo dos, se describen los objetivos de la Tesis.

En el tercer capítulo, se presenta el trabajo llevado a cabo en la síntesis de partículas de tipo Janus basados en MOFs. Una vez introducidos los conceptos de partículas de tipo Janus y la manera de sintetizados se presenta el trabajo experimental llevado a cabo. Este trabajo se basa en la evaporación controlada y selectiva de metales sobre parte de la superficie de MOFs. Esta metodología novedosa se organiza en diferentes pasos: i) Síntesis de MOFs nanoscópicos de tamaño controlado, ii) Deposición controlada en superficie de una monocapa de nanocristales de MOF dispersos, iii) Evaporación sobre las monocapas de nanocristales de MOFs de nanocapas de metal, iv) Separación de las superficies de los MOFs y obtención de las nanopartículas de Janus. La versatilidad de esta metodología nos ha permitido sintetizar diferentes compuestos de partículas Janus metal@MOFs, así como evaluar las propiedades magnéticas, fluorescentes, y catalíticas.

En el capítulo cuatro se describe otro de tipo de composites basados en MOFs y moléculas orgánicas funcionales. Este estudio consiste en introducir moléculas orgánicas funcionales creando defectos dentro de la estructura. En particular, se ha estudiado la capacidad de insertar la molécula xylenol orange; molécula con grupos coordinantes fuertes de tipo carboxílato con capacidad de capturar metales pesados. Se ha estudiado el mecanismo de incoprporación del XO dentro del MOF y su influencia en la formación del MOF, sus propiedades finales y la capacidad de eliminación de metales pesados del composite final fueron evaluados.

Acknowledgments

Quiero agradecer a CONACyT por darme la posibilidad de desarrollar el proyecto de investigación de esta Tesis doctoral. Así mismo, agradezco al Institut Catalá de Nanociencia i Nanotecnología (ICN2), a la Universidad Autónoma de Barcelona y al programa de Doctorado en Química por facilitar en todo momento las mejores condiciones y de calidad durante este proceso de formación.

Agradezco también al Prof. Dr. Daniel Maspoch y al Dr. Inhar Imaz, por su ayuda, guía y constante motivación durante el desarrollo de la Tesis, así como también a todos los integrantes del grupo de NanoUp.

Chapter 1

Introduction

1. Metal Organic Frameworks

1.1. History of Metal Organic Frameworks

In 1704, a Berlin colour-maker named Diesbach made a mistake when he was attempting to synthesize the known cochineal red lake pigment by mixing iron sulphate and potash. Trying to save money, he used contaminated potash with animal oil, obtaining a very pale solution that was converted to a deep blue solid after concentrating this solution. At this moment, instead of the expected strong red pigment, Diesbach accidentally created the first synthetic blue pigment, the Prussian Blue,[1] which was identified 273 years later as the first coordination polymer.[2] Today its known that Prussian Blue is a coordination polymer with a 3-D cubic structure built up from the connection of the heterometallic centres through cyanide organic ligands, resulting in a mix-valence polycyanide compound with a characteristic strong blue colour.

In the intervening years, little attention was paid to coordination polymers in comparison to purely organic and inorganic materials, and only a few scattered structural studies were reported. At the end of 40´s, Powell and Rayner determined the structure of the Hofmann clathrate $[Ni(NH_3)_2(Ni(CN_4))]\cdot 2C_6H_6$,[3] and few years later, Ywamoto´s group extended the description of related groups.[4] Remarkably, in 1959, Y. Saito *et al.* determined the structure of $[Cu(adiponitrile)]\cdot NO_3$, which was formed of six interpenetrating diamond networks.[5]

It can be considered that the interest on coordination polymers really took off at the end of 70´s. In 1977, Prof. A. F. Wells published a revolutionary paper in the Journal Monographs in Crystallography,[6] in which he introduced that inorganic crystal structures could be seen as networks by reducing them to well-defined nodes and connections. In a short communication in 1989, and in a subsequent full paper in 1990,[7] Prof. Robson adopted this approach to describe the family of coordination polymers. He proposed that: “a new and potentially extensive range of solid polymeric materials with unprecedented and possible useful properties may be afforded by linking together centers with either a tetrahedral or an octahedral array of valences by rod-like connecting units”.

In this study, the structure of an open diamond-like network was first described, in which tetrahedral Cu(I) centres and 4-connecting tetra(4-cyanophenyl)methane molecules were connected to form a solid in which the cationic framework represents only 1/3 of the crystal volume.

Since that progress, nobody could imagine that this new concept would open a new world in the field of chemistry, materials science and nanotechnology. But only five years later, in 1995 Prof. Yaghi confirmed the high potentiality of these pioneering studies. He reported the synthesis of an extended network with formula $Cu(4\text{-}4'\text{-}BPY)_{1.5}\cdot NO_3(H_2O)$ (where 4,4´-BPY is 4,4´-bypiridine), containing large rectangular channels filled by nitrate ions. He showed that these nitrates could be changed by other anions, demonstrating for the first time that channels in coordination polymers could be accessible. In this study, Prof. Yaghi named this porous coordination polymer as Metal Organic Framework (MOF).[8]

1.2. Definition of Metal Organic Framework (MOF)

International Union of Pure and Applied Chemistry (IUPAC) define a MOF as a coordination compound continuously extending in 1, 2 or 3 dimensions through coordination bonds, with an open framework containing potential voids, and a coordination compound is any compound that contains a coordination entity. A coordination entity is an ion or neutral molecule that is composed of a central atom, usually that of a metal, to which is attached a surrounding array of atoms or groups of atoms, each of which is called ligands.[9]

The literature shows that MOFs are focused on the assembly of organic and inorganic building blocks to form porous structures. and they are also known as coordination polymers (**Figure 1**).

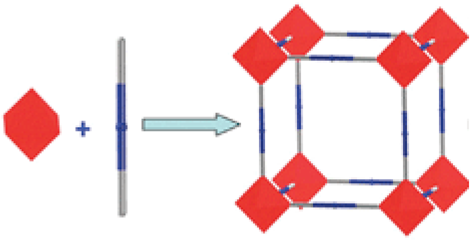

Figure 1. Schematic representation of the self-assembly between metal ions (red shape) and organic ligands (blue shape) to form a MOF.

1.3. MOFs design and their infinite possibilities

In the last 20 years, a great variety of MOFs has been described, showing mainly two key attributes: i) extremely large surface areas given by its ultra-micro-porosity, the highest among any known material; and ii) the flexibility in which their structures and compositions can be varied, offering a diversity of pore sizes and shapes. Both attributes confer MOFs with potential for myriad applications.

Most of these applications are obviously related to its ultra-high porosity (up to 7000 m^2/g; **Figure 2**),[10] and mainly include their use in storage, separation, and catalysis. A tasting of the performance of MOFs in these applications is given below. Also, the progress made in the MOF field in terms of their synthesis, topologies and applications have today been included in many reviews.[11,12,13,14 15,16,17,18,19,20]

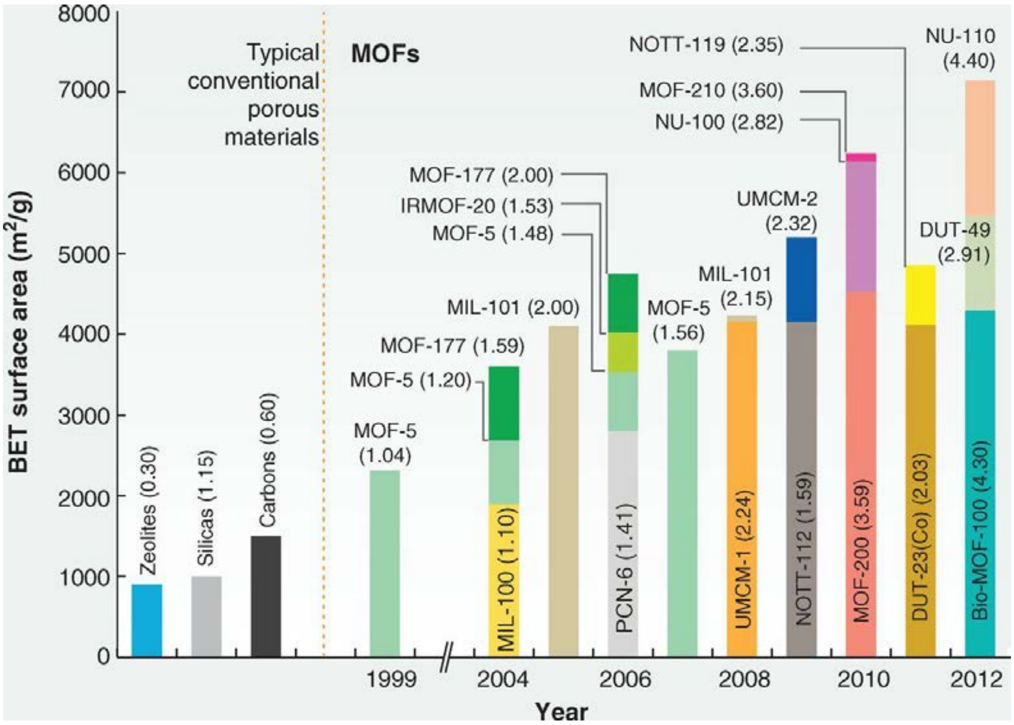

Figure 2. Progress in the synthesis of ultrahigh-porosity MOFs. BET surface areas of MOFs and typical conventional materials estimated from gas adsorption measurements. The values in parentheses represent the pore volume (cm^3/g) of these materials.

1.4. Properties and applications of MOFs

1.4.1. Gas storage and separation

The porous structure of MOFs enables using them as adsorbents of small molecules. However, this is only possible if guest species (such as solvents or unreacted precursors) located into the pores are removed after their synthesis. The first indication of reversible adsorption in MOFs was provided by Kitagawa *et al.* in 1997, who studied the porosity of a 1D coordination polymer with a general formula of $M_2(4,4'\text{-}BPY)_3(NO_3)_4$ (where M is Co, Ni or Zn, and 4,4′-BPY is 4,4′bypiridine). They proved that this MOF could adsorb gas molecules (O_2, CH_4 and N_2) in its crevices at a high pressure.[21] Then, permanent porosity of MOFs was further demonstrated in the layered zinc terephthalate $Zn_2(BDC)_4(H_2O)$ (nowadays known as MOF-2; where BDC is benzene-1,4-dicarboxylic acid) by conducting N_2 gas isotherms at low pressures and temperatures.[22] A subsequent step forward in the development of MOF as materials with gas storage capacities was the synthesis of the first robust 3D MOF with formula $Zn_4O(BDC)_6$ (known as MOF-5).[23] MOF-5 exhibited a very high potential porosity of 63% of the volume of the unit cell and a surface area of 2320 m^2/g, which largely outperformed zeolites.

First findings in gas sorption of MOFs and the increasing control of their synthesis motivated scientists to increase the porosity of these materials, reaching today unprecedented surface areas. One of the strategies that allow increasing the pore volume of MOFs is based on their design using the reticular chemistry approach. This strategy is based on taking an existing MOF as a reference and replacing the original ligand by an expanded version of it. Following this approach, the topology and the secondary building unit (SBU) of the "parental" MOF are maintained and therefore, the pore volume is increased. In fact, this strategy has allowed for the preparation of reveal families of MOFs (e.g. MOF-5,[24] Zr-MOF,[25] and IRMOF-74[26] (**Figure 3**a-c)), some of them with pore size larger than 20 Å, thereby entering to the world of "mesoporous materials".[27]

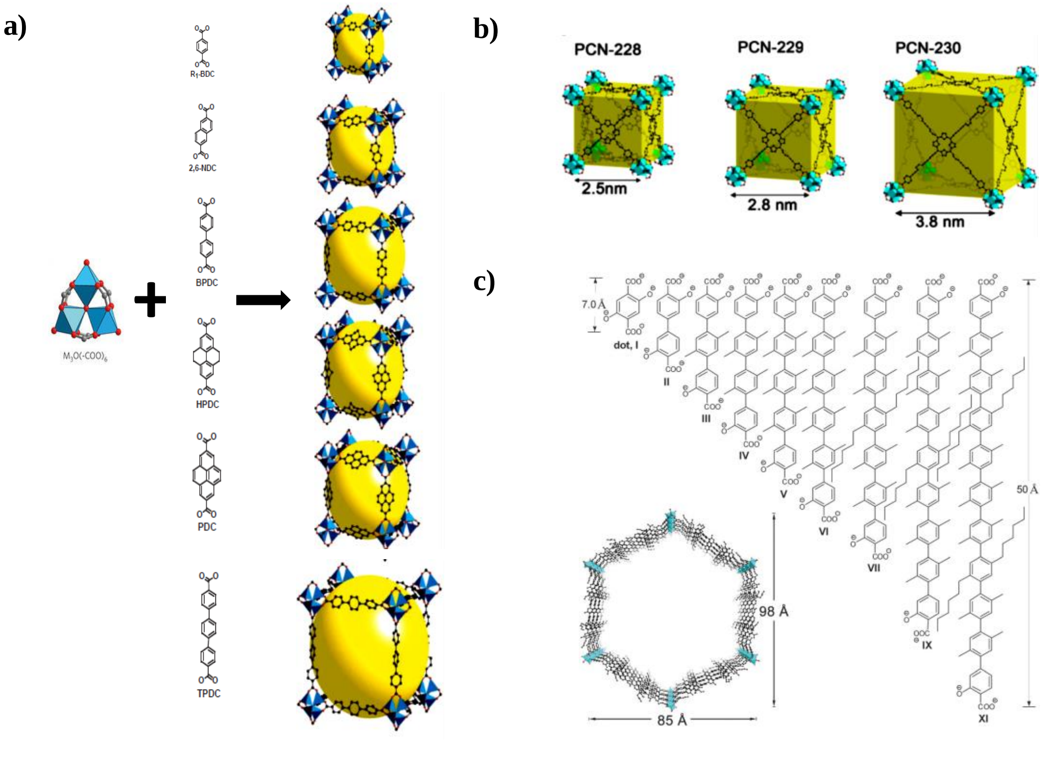

Figure 3. Isoreticular expansion of archetypical MOFs with different topologies through reticular chemistry: a) MOF-5, b) Zr-MOF, and c) IRMOF-74 families.

1.4.2. H_2 adsorption

H_2 is an ideal carrier and is considered the future fuel due to its abundance, its high heat of adsorption (20 Mj/Kg of H_2 compared to 44.5 Mj/kg of gasoline) and its non-polluting post combustion products (mainly water). However, its storage and transport present safety and economic challenges. To date, H_2 storage is based in chemisorption, which gives high storage capacity but slow kinetic release and poor reversibility. For instance, metal hydrides such as $LaNi_5H_{6.5}$ bind strongly to H_2 with ahead of the adsorption reaching 200 $KJ \cdot mol^{-1}$. However, this high heat of the adsorption makes H_2 release kinetically unfavourable and only possible at high temperatures (400 k).[28]

As an alternative, MOFs can physisorb H_2, which would ensure a reversible loading and release of H_2, demanding less energy input in the desorption than the current chemisorbants. Since physisorption has a good correlation with the surface area, one of the main strategies to increase H_2 uptake is to increase the surface area of MOFs. For instance, low density MOFs made of carboxylate-based ligands such as NU-100,[29] and MOF-210[30] have shown a high H_2 adsorption of 9% (weight %) at 56 bar and 77 k.

Structural features of the network can also have an impact on H_2 storage. Network catenation seems to have a positive effect in H_2 storage, as demonstrated by the comparison of the H_2 adsorption of two otherwise isostructural MOFs with formula ($Cu_6(H_2O)_6(TATB)_4$) (known as PCN-6; where TATB is 4,4′,4′-s-triazine-2,4,6-triyltribenzoate).[31] The catenated structure showed an uptake of 95 $mg \cdot g^{-1}$ at 50 bar and 77 k, whereas the non-catenated structure had an uptake 58 $mg \cdot g^{-1}$ at the same conditions.

Also, exposition to open metal sites can increase enthalpy of adsorption for H_2. For example, the Ni(II) analogue of ($M_2(DHTA)$) (known as MOF-74 where DHTA is 2,5-dihydroxiterephtalic acid) presents and ordered arrangement of opened metal sites facing the 1D channels in its structure. This feature is responsible for its high enthalpy of H_2 adsorption, which results in high H_2 uptake, particularly at low pressure.[32]

However, the promising storage capacities demonstrated by MOFs have only been achieved at low temperatures (77k) so far, becoming negligible when the room temperature is approached. For this reason, MOFs are still far from the targets (5.5 weight% at 233k) set for their practical application in H_2 storage.

1.4.3. CO_2 sequestration

Global CO_2 emissions exceeded 32.1 gigatons in 2016 and the 44% of CO_2 emissions comes from the burning of coal in electricity plants.[33] CO_2 is one of the main gases responsible for the anthropogenic effect of the greenhouse. The major component of the flue gas is nitrogen (~70%), followed by CO_2 (10-15%), water vapour (10-12%) and other minor gases. Therefore, high selective adsorbents are required to sequestrate CO_2 from the gas mixture. However, if the affinity of the adsorbent is too high, the energy required to remove the adsorbed CO_2 and regenerate the adsorbent increases, thereby resulting in an energy penalty for the sequestration of CO_2. For example, in the current technologies based on alkanolamine aqueous solutions, approximately 70% of the overall cost of CO_2 sequestration is attributed to the adsorbent regeneration.[34]

MOFs can contribute to address this cover cost as their guest removal is less energy demanding while still achieving high selectivity for CO_2. Preferential adsorption for CO_2 can be achieved by two means: (i) size-based selectivity by which MOFs with small pores would allow only the diffusion of molecules up to a certain size into their pores (kinetic effect); for example, tuning the window size to allow CO_2 (kinetic diameter = 3.3 Å) to pass through the framework, but not nitrogen (kinetic diameter = 3.64 Å);[35] and (ii) adsorptive selectivity arising from the difference in the affinity of the various components in the mixture to be adsorbed on the pore surface of the MOFs (thermodynamic parameter).[36] Regarding the kinetic-based selectivity, the small size of the molecules in the gas stream would require MOFs with very small pores. However, almost all MOFs with high surface areas and high storage capacities for CO_2 have pores with apertures larger than the CO_2 molecules, invalidating them for molecular sieving.[37,38,39]

Therefore, the strategy based on differential heat of adsorption of the molecules composing the gas mixture seems to be the most promising one. Here, the higher quadrupolar moment of CO_2 compared with the other gases (specially N_2 and O_2) opens the door to design MOFs with pore surfaces having higher affinity for CO_2. For example, this affinity can be increased when unsaturated metal sites are decorating the pore walls. Unsaturated metal ions can act as a charge dense binding sites that induce the polarization of the adsorbed CO_2, and therefore, increase the selectivity for CO_2 over other gases less polarizable.

In 2015, Long's group reported a series of "phase changing" MOF adsorbents.[40] These MOFs are extended MOF-74 materials with their open metal sites functionalized by N,N´-dimethylethylenediamine, rather than forming carbamates with dangling uncoordinated amine groups (as originally thought).[41,42] In this example, a strong interaction between the unsaturated Lewis metal sites decorating the pores and the CO_2 molecules were observed. This interaction contributed to the high adsorption of 20 w% CO_2 at 1 atm and 303 K.[43]

1.4.4. CH_4 sequestration

In the last years, economic and environmental considerations have increased the interest in natural gases, comprising mainly CH_4 as a fuel for transportation and specially, as a replacement for petrol (gasoline). From an environmental point of view, CH_4 delivers roughly twice the energy of coal with the same amount of CO_2 released. From an economical point of view, the price of natural gas has lived a spectacular recent drop in price due to deployment of inexpensive technologies for its recovery from shale.

The remaining challenge to use CH_4 as a source of energy is its mass-and volume-efficient storage at ambient temperature and its delivery. Currently, CH_4 is stored at very high pressures (250 bar) in most natural gas-powered vehicles. While it is suitable for large vehicles such as buses, this solution is less than satisfactory for cars. The U.S. Department of Energy (DOE) estimated that a storage of 263 v/v is required for practical on board applications. Therefore, finding alternative storing systems is today a priority.

In this sense, MOFs are known to be useful in the storage of gases including CH_4. Among the MOFs studied for methane storage, the most promising are HKUST-1, Ni-MOF-74, MOF-5, MOF-177, MOF-205, MOF-210, and PCN-14, which stand out as having some of the highest total volumetric storage capacities.

Since the automobile industry requires that 5 bar of methane pressure remains unused in the fuel tank, a parameter termed working capacity is the key to evaluating the performance of methane storage materials. MOF chemistry offers great potential to address challenging issues to the CH_4 storage. Here, HKUST-1 was reported to be the best performing material at intermediate pressures (35–65 bar). [42] This MOF shows a total volumetric uptake of 267 cm^3 (STP) cm^{-3} at 298 K and 65 bar, with a corresponding working capacity (5–65 bar) of 190 cm^3 (STP) cm^{-3}. Although HKUST-1 exhibits remarkable performance in comparison to the best storage media, it is still far below the gravimetric and volumetric DOE target of 0.5 g/g and 264 $cm^3 \cdot cm^{-3}$ in the range of temperatures between −40°C and 85 °C, typical for a vehicle in real operation.[44]

1.4.5. Gas purification

The preferential adsorption of one gas over another can be exploited to purify or separate gas mixtures. One way of promoting gas selectivity is based on the relative size of the molecule compared to the pore (i.e. based on kinetics).

Therefore, the possibility to tune the pore size in MOFs can be used to prepare molecular sieving. For instance, $Zn(PhIm)_2$ (known as ZIF-7; where PhIm is bezimidazole) with an estimated pore size in between H_2 and CO_2 has been used to separate mixtures of these gases.[45] The presence of metal open sites can also promote preferential interaction with gases depending on their chemical formulation (thermodynamic effect). Long *et al.* demonstrated the potential of this approach by studying the different hydrocarbon affinity towards unsaturated Fe(II) ions in the Fe-MOF-74.[41] It was observed that the adsorption capacity increased with the unsaturation, being acetylene the most adsorbed gas. This selectivity can therefore be exploited for separating pure gases from naphtha cracker. In conclusion, both topology and functionality in the pores of MOFs can be exploited to resolve gas mixtures.

1.4.6. Catalysis

MOFs are very attractive for applications in the liquid phase, since they possess catalytic site characteristics and the advantages of easy separation and recycling. The properties of MOFs are an ordered arrangement of the active metals centres along with a potential porosity and chirality. In principle, the active sites of MOF catalysts can be:[46]

(i) Metal centres with an unsaturated coordination environment
(ii) Other catalytic species encapsulated in the pores
(iii) The sites inherent in the framework

To date, it has been described that several MOFs can be employed as solid catalysts or catalyst supports for a variety of organic transformations. These reactions include Knoevenagel condensation,[47] aldol condensation,[48] oxidation reactions,[49] epoxide formation,[46] hydrogenation,[50] Suzuki coupling,[51] alkylation of amines,[52] cyclopropanation reactions,[53] Henry reactions,[54] Friedel–Crafts reactions,[55] cyanosilylation,[56] etc.

2. Nanoscaled Metal Organic Frameworks (NMOFs)

Currently, there has been an increasing interest in controlling of zise of MOFs at the submicrometer level (100–1000 nm) and further down to the nano scale (1-100 nm).[57,58] This is because although MOFs show high promise for many of the aforementioned research areas, they do not always cover the relevant requirements for the device material fabrication in nanotechnology. NanoMOFs may exhibit different and/or enhanced properties and reactivity compared to the traditional bulk materials, and they could be used in a number of novel and emerging application areas such as nanomedicine,[59,60] where nanoscale dimensions are necessary for the internalization of functional materials into cells,[61] sensor technology, functional membranes thin films, traditional storage and separation, catalysis applications, or molecular electronics, where, if properly scaled down, each structure may represent information.[62,63]

In this section, we summarize the huge efforts that have been recently dedicated to develop new methodologies to synthesize NMOFs and their potential properties and applications.

2.1. Synthesis of NMOFs

There are two main approaches that can be considered when one wants to synthesize NMOFs:

(i) Confinement of the supramolecular assembly that leads to MOF formation at nanoscopic locations; for example, by using emulsions or templates.
(ii) Favouring the nucleation versus crystal growth; for example, by using fast precipitation methods or by using microwave and ultrasound synthesis.[64]

2.1.1. Emulsion confinement

Nanoemulsion is a suspension of small droplets with diameters ranging from 50 to 1000 nm, in which the droplets are usually stabilized by a surfactant. In other words, a nanoemulsion is one liquid in a second liquid when combined do not mix with each other. Because of their dimensions, these droplets can be used as “nanoreactors” to confine the self-assembly, nucleation and growth of NMOFs (**Figure 5**). Briefly, this approach usually consists of first dissolving each precursor in the solvent that will be dispersed. A water-in-oil emulsion, or reverse emulsion is then prepared from a surfactant, and the collisions between droplets containing those precursors or the application of an external stimulus, such as temperature, light, or microwave radiation, spontaneously induce their polymerization thus delimiting their growth inside the nanodroplet.

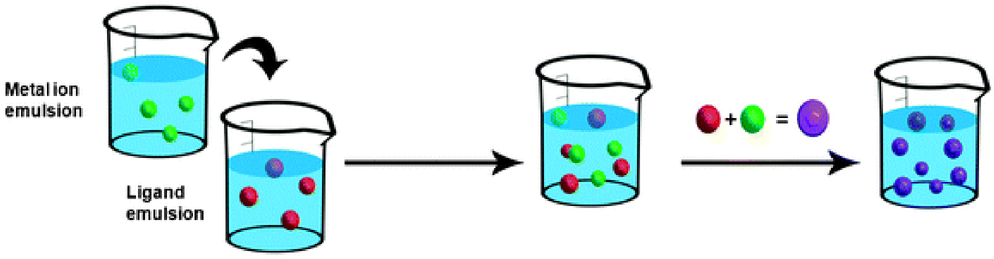

Figure 4. Schematic representation of the micro- and nanoemulsion strategy for synthesizing NMOFs.

For example, by dissolving Prussian blue precursors in water, using this solution to create a water-in-oil emulsion and further exposing this emulsion to daylight, Mann *et al*. synthesized the first examples of NMOF: Prussian blue cubic nanocrystals.[65] Since then, emulsions have been successfully used to produce nanocrystals of heterometallic cyanometalates, Prussian Blue analogues using triazole instead of cyano groups and Gd(III)-based NMOFs.

Besides the utility of their internal volume as "nanoreactors", nanodroplets of these emulsions have also the potential to be used as "soft templates" to prepare MOF-based nanoshells. In this case, the polymerization must be concentrated on the interface of the droplets by using, for example, a chemical affinity surfactant. Thus far, this strategy has been used by Wang *et al*. who synthesized the first examples of Prussian blue nanoshells.[66] These shells were synthesized by preparing an oil-in-water emulsion with an organometallic surfactant terminated with pentacyano(4-(dimethylamino)pyridine)ferrate. Then, the addition of Fe(III) ions to the aqueous solution induced the coordinative polymerization between them and the surfactant, thereby creating a MOF-based shell on the interface of each droplet.

2.1.2. Template confinement

Nanomaterials are also excellent candidates to be used as templates for fabricating NMOFs. In this methodology, the NMOF precursors are deposited on the template by using a deposition technique, such as layer by layer (LBL) growth. This deposition followed by the removal of the template using thermal or chemical techniques can leave behind NMOFs that mimics the shape and size of this template (**Figure 5**).

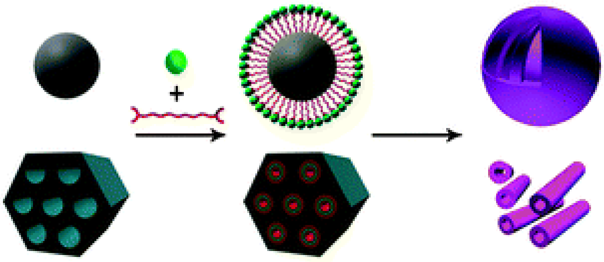

Figure 5. Schematic representation of the template confinement synthetic strategy for synthesizing NMOFs. Green ball represents the metal ion while the red shape represents organic ligand.

For instance, Martin *et al.* reported the LBL growth of a film composed of Zr(IV) metal ions and diorganophosphonate ligands on the pores of an alumina membrane, followed by the removal of this membrane using phosphoric acid allowing the fabrication of highly uniformed metal–organic nanotubes.[67] In this case, the interaction between the alumina and Zr(IV) ions was exploited to attach the metal organic structure on the template during the growing process.

The intrinsic supramolecular character of NMOFs makes them very responsive systems towards weak interactions present in the reaction media. For example, metal nanoparticles fuctionalized with different active groups can be used to induce seed nucleation by selective interaction with the building blocks, altering the formation rate and the size of the final product. Oh *et al.* employed the template strategy to induce the nucleation of NZIF-8 (Zn(MIM)$_2$; where MIM is 2-methylimidazole), on the surface of carboxylated polystyrene (PS) microspheres.[68]

2.1.3. Controlled precipitation

Another strategy to prepare NMOFs is based on mixing the precursors under certain reaction conditions that induce the fast nucleation to increase the seed number and reduce the crystal growth rate. In most of the cases, these conditions involve the use of capping agents, microwave radiation, ultrasounds, temperature, and pH modulators (**Figure 6**).

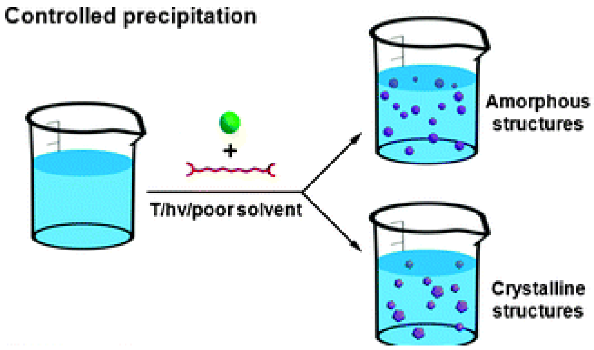

Figure 6. Schematic representation of the controlled precipitation of NMOFs.

For example, Horcajada, Gref *et. al.* showed a series of NMOFs ($Fe_3O(H_2O)_2Cl(BTC)_2$) known as MIL-100, MIL-101, and Fe_3O(fumarate) known as MIL-88, by simply mixing Fe(III) metal ions with different multitopic carboxylate ligands, BDC, BTC, fumaric acid, *etc*., in a variety of solvents above 100 ºC.[60] Here, it was found that the temperature and the reaction time usually play a major role in the crystal size under solvothermal conditions. Later, the effect of both parameters was studied in detail in the synthesis of NMIL-88A showing that low temperatures and reaction times promote the formation of sub-200 nm crystals.[69]

The use of microwave irradiation and ultrasonic irradiation can also be exploited to produce NMOFs. Zheng, Ni *et. al.* showed for the first time the use of microwave radiation to induce the precipitation of an already known isoreticular Zn(II)-based MOFs (IRMOF-1, IRMOF-2, and IRMOF-3), at the nanometer scale.[70] Similarly, sonochemical synthesis can lead to homogeneous nucleation and a substantial reduction in crystallization time. The well-known MOF-5 was miniaturized to 5-25 micrometres using this approach.[71]

In some cases, the use of an excess of ligand can also induce fast nucleation and reaction times. ZIF-8 nanocrystals of 70 nm were prepared in aqueous media and room temperature by mixing $Zn(NO_3)_2$ and an excess of ligand MIM. In this case, the excess of ligand may have two roles; (i) induce a faster reaction with the metal precursor; and (ii) inhibit the growth of the formed seeds.[72] Also, the use of capping agents or modulators is an alternative method to synthesize NMOF. In principle, the capping agent can alter the coordination equilibrium between the metal ion and the organic linker, and the competition between the ligand and capping agent offers the possibility to modulate the rate of the framework extension and the crystal growth.[73]

2.2. NMOFs on surfaces

The fabrication of functional materials into appropriate devices will advance the development of important technologies arising from the need to rapidly process data, to efficiently produce and store energy, and to improve human health through the early detection of diseases.[74]

For this reason, one of the current challenge is to control the growth of NMOFs directly on surfaces. The fabrication of NMOF films focuses on the attempt to deposit or control the homogeneous growth of NMOF crystals on a substrate.

Nowadays, some strategies have been explored to fabricate NMOFs membranes and thin films including the direct assembly and growth of NMOFs on surfaces, the Liquid Phase Epitaxy (LPE) Layer by Layer synthesis, the use of Langmuir-Blodgett (LBL) monolayer transfer technique, *in-situ* crystallization, colloidal and seeding deposition, electrochemical deposition and gel-layer techniques (**Figure 7**).[64]

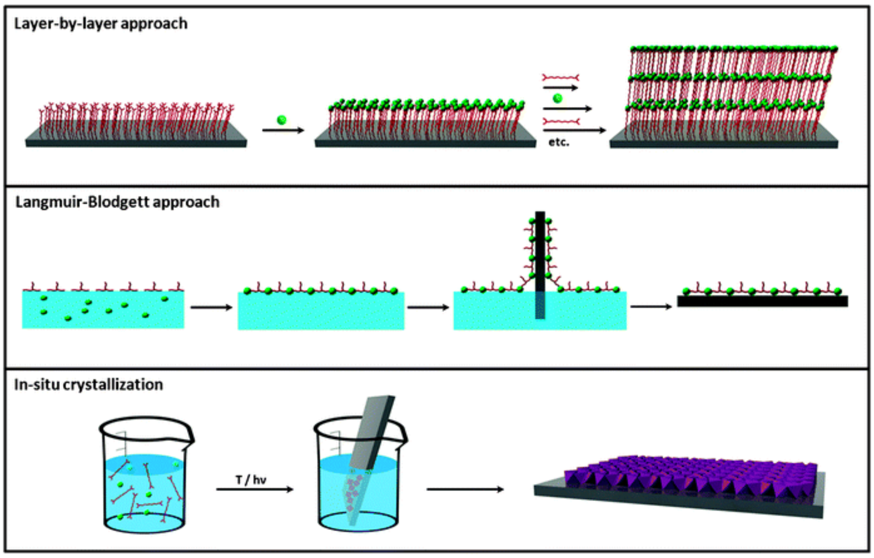

Figure 7. Schematic illustration of the three principal synthetic strategies used for preparing 2-D metal–organic nanomaterials, including the layer-by-layer approach, the Langmuir–Blodgett approach and the in-situ crystallization.

In the fabrication of NMOF thin films there are some important features to be considered depending of the final application. Some of them are lattice interpenetration, film roughness, crystal alignment (in-plane and out-of plane orientations), crystal density and crystal size, crystal domain size, distribution, cohesion, and adhesion to the substrate.

2.3. Applications of NMOFs

A broad range of promising properties of NMOFs can be obtained by taking advantage of the multiple inorganic and organic building blocks that can be combined to prepare NMOFs. One can use the intrinsic properties of either the organic and inorganic components. The ability of metals ions to interact with phonons and electrons, to show luminescence, to have strong absorptions, and to have interesting magneto-optical properties makes NMOFs suitable as functional materials in devices. The organic components can also exhibit their own functionalities. For example, organic chromophores, radicals, and biomolecules are excellent building units to prepare optical, magnetic, and biocompatible NMOFs.

The aforementioned synthetic approaches and functionalities of NMOFs can optimize their potential in gas storage and separation,[75,76,77] drug delivery,[78] catalysis,[79] magnetism,[13] and as sensors,[80,81,82] offering a abroad view of this class of nanomaterials.[83,84,85,64] **Figure 8** summarises and illustrates significant examples of the state of the art related to NMOFs and their applications.[86,69]

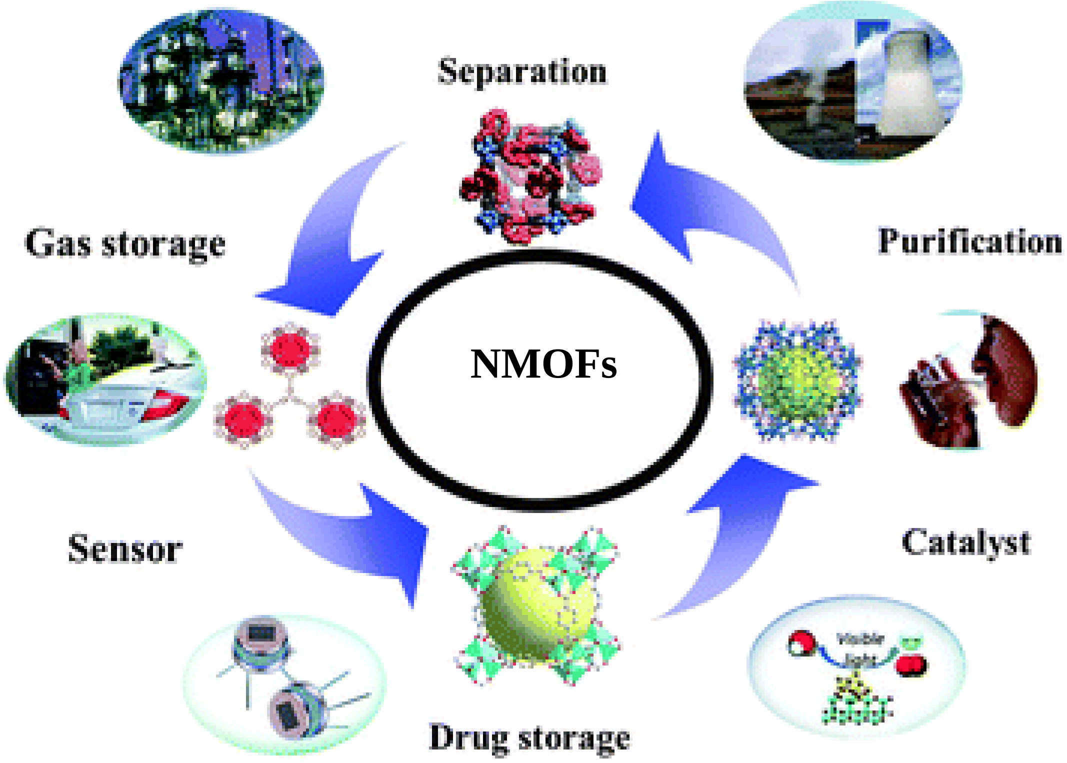

Figure 8. Representative scheme of the NMOFs in applications; gas storage, separation and purification, catalyst, sensor, drug storage.

2.3.1. Gas sorption in NMOFs

Materials with a high gas adsorption capacity are gaining interest due to the need to store and handle new environmentally friendly fuels or remove greenhouse gases. Therefore, the exceptional porous characteristics already exhibited by bulk MOFs make them excellent components for creating NMOFs-based membranes or thin films with potential applications in gas separation, gas storage, and fabrication of novel sensors.

The first NMOF-based membrane showing separation performance was reported by Qiu *et al.*[77] This membrane, which was created with N-HKUST-1 crystals on an oxidized copper grid, showed a higher permeation flux and excellent permeation selectivity for H_2 in comparison with CO_2, N_2, and CH_4. This fact can be explained by the size selectivity occurring in the HKUST-1 channels. The relatively small H_2 molecule goes through the membrane more easily than CO_2, N_2, and CH_4. Also, the fabrication of N-ZIF-90 membranes on polymeric hollow-fiber support resulted in high surface area membrane modules. The gas separation factors, permeances and selectivities of the polymeric-supported N-ZIF-90 membrane indicated that it should able to separate liquid alkenes.[87]

NMOF built up from Zn(II) metal ions connected through isophthalate and 4,4′-bipyridyl ligand is yet another example reported.[88] These porous nanocrystals reported by Groll *et al.* showed adsorption capacities almost identical to their bulk counterparts, but the shapes of the sorption isotherms differed significantly and the adsorption kinetics increased dramatically. Also, Oh *et al.* successfully synthesized NMOFs based on In(III) metal ions and BDC ligands that showed an H_2 and CO_2 uptake of 140 $cm^3 \cdot g^{-1}$ and 333 $cm^3 \cdot g^{-1}$, respectively.[89]

2.3.2. Catalysis in NMOFs

Several applications have been proposed for NMOF-based catalysis. For example, N-HKUST-1 was embedded into silica monoliths for a continuous flow Friedländer reaction for the synthesis of substituted quinolines. Thanks to the coordinatively unsaturated copper metal centers, N-HKUST-1 was regarded as a suitable catalyst for the Lewis acid reaction, and it was obtained a steady 85% conversion after 4 h flow and a yield of 826 g of product per g of catalyst per day. The immobilized N-HKUST-1 was 2.5 times more productive than a commercial N-HKUST-1 powder, thanks to the high efficiency of the MOF crystal size in the monolith.[89]

2.3.3. Sensing in NMOFs

MOF-based sensors have been developed not only by their luminescent properties, if not also, by the electrochemical responses towards small molecules, gas molecules, ions (cations and anions), pH, humidity, temperature, and biomolecules.[81]

In this area the photoluminescence in MOFs have received growing attention; especially for nitroaromatics (NACs) sensing that is important in the areas of homeland security, environmental cleaning and military applications.[90,91] For example, $[Cd_2Cl(H_2O)(L)]\cdot 4.5DMA$ (DMA=N,N-dimethylacetamide; NENU-503, NENU=Northeast Normal University) displayed highly selective and recyclable properties in the detection of nitroaromatic explosives as a fluorescent sensor. In addition, this MOF was the first to distinguish between nitroaromatic molecules with different numbers of $-NO_2$ groups (**Figure 9**).[92]

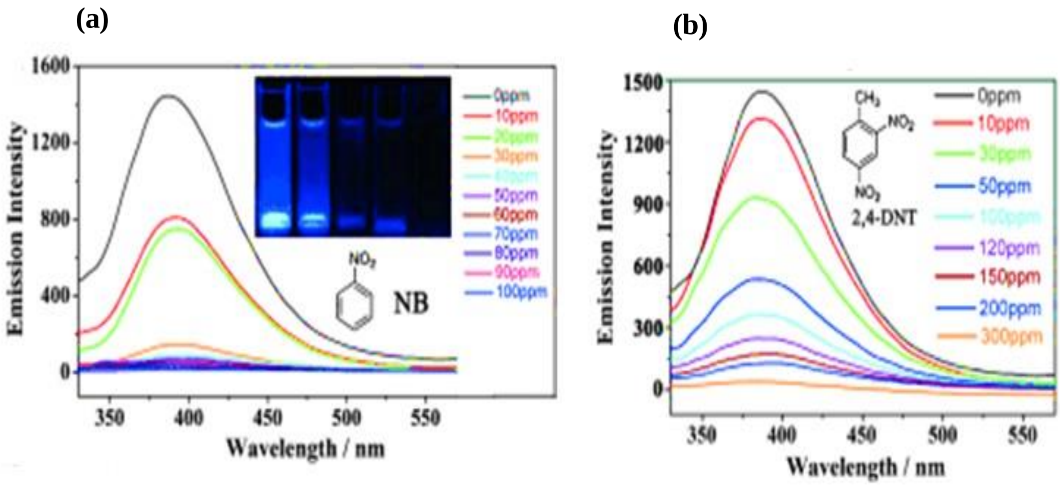

Figure 9. (a) Emission spectra of NENU-503 in different concentrations of nitrobenzene in DMA (excited at 295 nm). Inset: a photograph taken under UV light (365 nm), showing the fluorescence quenching upon addition of nitrobenzene to NENU-503. (b) Emission spectra of NENU-503 in different concentrations of 2,4-DNT in DMA (excited at 295 nm).

Also, thin films of HKUST-1, NOTT-100, NOTT-101 and PCN-14 have been deposited on quartz crystal microbalance devices. The films showed an effective mechanical coupling to the substrate, which responded reversibly to vapors of water, acetone, and *n*-hexane by changing the surface acoustic wave (**Figure 10**).[93]

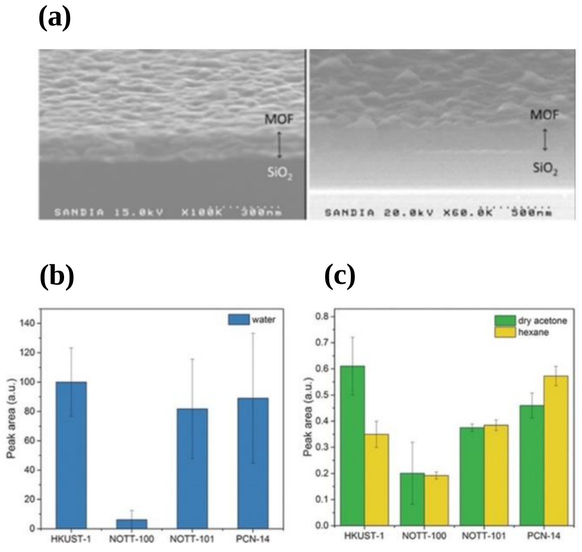

Figure 10. a) SEM images of the MOF films deposited on SiO_2: NOTT-100, NOTT-101, PCN-14, b) Phase shift intensity (normalized for easier viewing) versus time for SAW devices coated with HKUST-1, NOTT-100, NOTT-101, and PCN-14 upon injection of water, and c) acetone and hexane.

Another interesting example resulted from printing, photoluminescent lanthanide−organic frameworks (Ln-MOFs) were printed onto plastic, paper, and foils with a conventional inkjet printer. Ln-MOF inks were used to reproduce color images that can only be observed under UV light irradiation. This approach opens a new window for exploring Ln-MOF materials in technological applications, such as optical devices (e.g., lab-on-a-chip), and as proof of authenticity of official documents (**Figure 11**).[94]

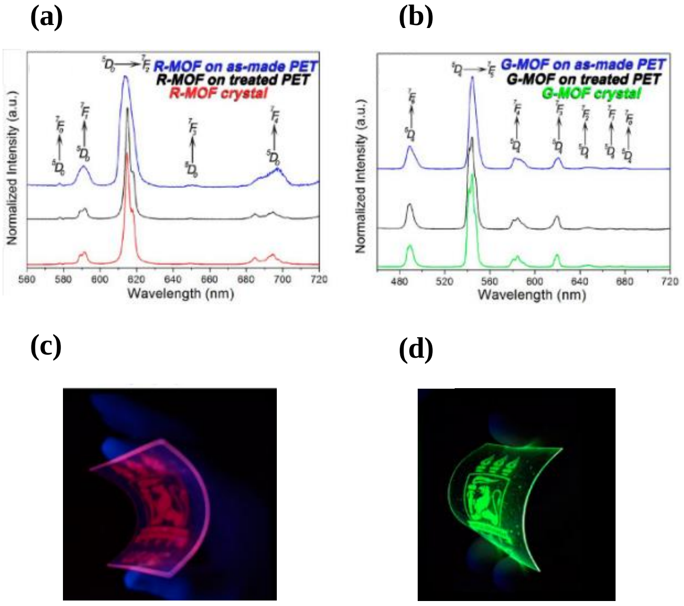

Figure 11. (a and b) Emission spectra of R- and G-MOF inks. Solid red and green lines represents the emission spectra of the R- and G-MOF crystals, respectively, and solid black and blue lines denote the emission spectra of R- and G-MOF inks deposited onto treated and as-made transparency PET foils, respectively. (c and d) LnMOF inks deposited onto treated transparency PET substrates under UV light irradiation (λ_{exc} = 254 nm).

Another example that shows the optical properties of NMOF thin film is a ZIF-8 interferometer, which was fabricated and used as a selective sensor for gases and vapours.[95] The relation between the thickness of the film and its luminescent properties was subsequently proven by deposition onto an ITO substrate (**Figure 12**a).[96] A white emitting LED was fabricated merging a blue emitting cadmium based MOF with a yellow emitting iridium complex (**Figure 12**b).[97] Electrochromic films on FTO were prepared using zinc based MOFs with variously functionalized pyrazolate ligands, exhibiting colors from green to red,[98] or with a zirconium based MOF film showing a drastic and reversible blue (**Figure 12**c).[99]

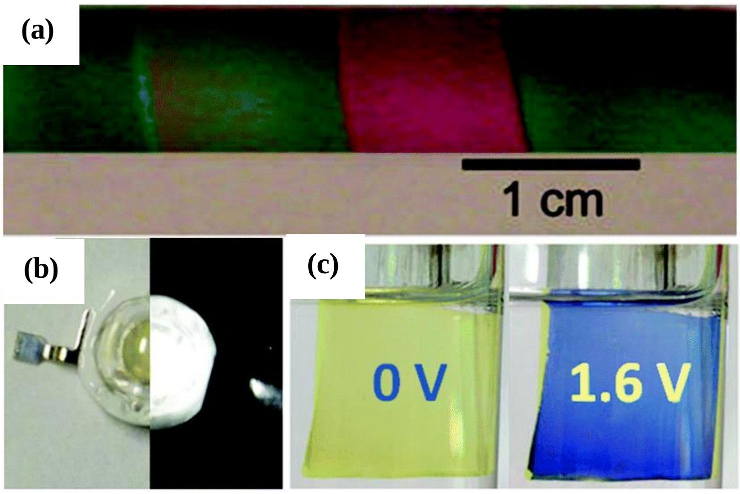

Figure 12. (a) A series of ZIF-8 films of different thickness on a silicon substrate; (b) photograph of a white LED fabricated using a cadmium based MOF loaded with an iridium base complex without (left) and with a 150 mA current applied (right); (c) photos of the electrochromism of a zirconium based MOF thin film on FTO electrode before (left) and after (right) applying a 1.6 V potential.

2.3.4. Drug delivery in NMOFs

Employing NMOFs as carriers for drug delivery is an emerging field largely owing to unique advantages that MOFs can offer in comparison to other drug carriers. The tunable nature of the chemical composition, surface area, and pore sizes, makes these materials ideal candidates for loading a range of drugs and biomolecules. The need for controlling the loading and release of drugs from NMOFs on demand is a prerequisite for designing the next generation of NMOF-based delivery devices.

In this sense, Furukawa *et al.* positioned Au nanorods inside aluminum-based MOFs to form a stimuli-responsive device (**Figure 13**). This strategy takes advantage of the highly efficient conversion of optical energy into heat that occurs when the Au nanorods are irradiated into their plasmon band.[100]

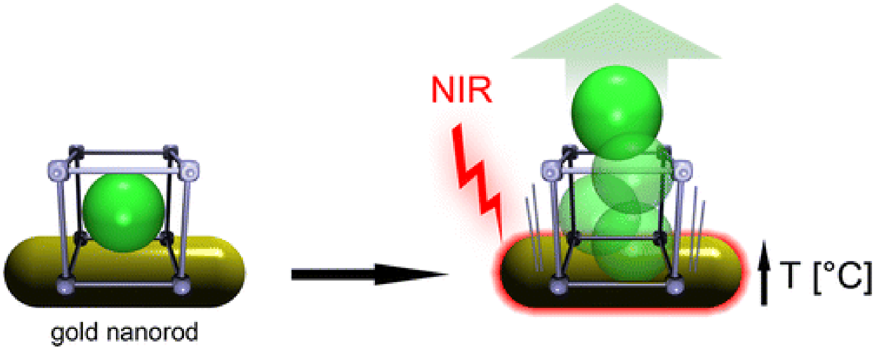

Figure 13. The light-induced molecular release is based on the unique hybrid system where the optical switch gold nanorod (GNR) is incorporated within porous coordination polymer (PCP).

Another example of using NMOFs as drug delivery system is the family of isoreticular ZnBDP-X based on Zn(II) metal ions and the functionalized organic linkers (1,4-bis(1H-pyrazol-4-yl)-2-X-benzene (H_2BDP_X; X = H, NO_2, NH_2, OH)), which were used to deliver antitumor drug [Ru(p-cymene)Cl_2(pta)] (RAPTA-C), pta = 1,3,5-triaza-7-phospaadamantane). In this case, the antitumor was previously encapsulated in the pores of the ZnBDP_X series. Among these materials, ZnBDP-OH and ZnBDP-NH_2 matrices showed a slower rate of delivery and higher percentage of release than ZnBDP_NO_2 and ZnBDP-H systems (**Figure 14**).[78]

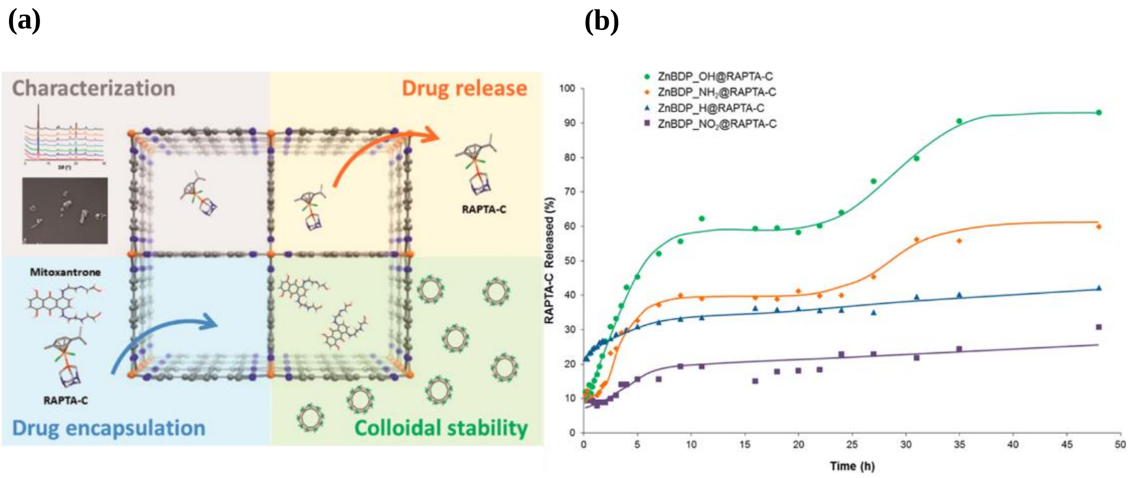

Figure 14. (a) Schematic representation of using nanocrystals of ZnBDP-X as drug delivery system, (b) RAPTA-C release from ZnBDP-X@RAPTA-C (X = H, NH_2, NO_2, OH).

2.4. NMOF composites

The advent of controlling the synthesis of NMOFs has recently inspired researches to conceive methods for combining NMOFs with other materials to obtain complex hybrid nanocomposites that many the best prospects of each component; in some cases, enabling magnetic effects. To date, NMOFs have been integrated with several functional materials including as small bio-molecules (e.g. enzymes), metal nanoparticles (NPs), nanowires (NWs), quantum dots (QDs), carbon nanotubes (CNTs), oxides, nanofibers, polymers, polyoxometalates (POMs), and organic dyes (**Figure 15**).[101,102]

Figure 15. Schematic representation of MOF based composites

2.4.1. Synthesis of MOF composites

To date several fabrication methods have been developed to synthesize NMOF based composites (**Figure 16**).[19] The main methods are;

<u>Solution blending method</u>. This method consists of mixing polymers and functional species of NMOFs by mechanical stirring or sonication, enhancing the homogeneity of the incorporated materials in solution before solvent evaporation from the polymer based composite. For example, flexible NMOF/polymer membranes, such as HKUST-1/PMMA,[103] ZIF-8/matrimid,[104] ZIF-90/matrimid,[105] MOF-5/matrimid,[106] and HKUST-1/matrimid,[107] have been produced using this method. The ease of mass production puts these MOF/polymer membranes in high demand for industrial applications. However, the variation in the NMOF lattice resulting from the host–

guest interactions of the MOF structures leads to a weak adhesion between the polymers and the NMOFs when the solvents are removed. Moreover, the MOF/polymer membranes formed are often highly defective with unpredictable voids inside their structures.

Electrospinning method. This method consists of the formation of fibers when a high voltage is applied to a liquid droplet that makes it charged. Then, the high cohesion of the molecules to liquid leads to the formation of a charged liquid jet and the fast vaporization of the solvent during the liquid jet flight. The diameters of the fibers and the NMOF loadings can also be tuned by varying the polymer concentration, and the polymer to NMOF ratio in the spun mixtures, ZIF-8/PVP,[108] ZIF-8/PS and MIL-101(Fe)/PS.[109]

In situ growth of NMOFs in the matrices. In this approach, the matrices are immersed in a solution containing MOF precursors and then heated. This process induces the growth of the NMOFs on the internal and/or external surface of the matrices. For example, UiO-66 over the polyurethane foam template,[110] and HKUST-1 and ZIF-8 on a polysulfone[111] have been produced using this method.

Surface coating. This method consists of the coating of silica or bio-polymer on the MOF surfaces to optimize their performance. The silica/polymer coating can also be used to control the release of loaded drugs in the MOF cavities during drug delivery applications.[112]

Impregnation of NMOFs with functional species. Direct adsorption, incipient wetness, and ion exchange are three loading strategies utilized to impregnate the precursors into the MOFs under solvent conditions. This method involves MOF powders which are immersed in a solution containing metal ions, dyes, functional organic molecules and/or NPs.

Encapsulation of pre-synthesized structures into NMOFs. This strategy is based on encapsulating pre-synthesized nano-objects into NMOFs. To achieve this encapsulating, there are three mayor methods:

i) The “build-bottle-around-ship” method to encapsulate clusters into MOF composites.
ii) Selective nucleation and growth of MOFs on the surface of an inorganic nanostructure.
iii) The heteroepitaxial growth of MOF shells on another MOF crystal surface.

In a typical "build-bottle-around-ship", the desired catalytic metallic-complex is encapsulated inside the nanopores/channels of porous materials in the presence of the synthetic precursors, such as is the case with metallic-complexes encapsulated by the cage of zeolites.[113] Following this method for example, polyoxometalates (POMs) have been encapsulated forming POM/HKUST-1,[114] and POM/MIL-101(Cr) composites.[115]

The selective nucleation and growth of MOFs on inorganic nanostructures as metallic nanoparticles consists in the chemical modifications of the surfaces of the nanoparticles with organic molecules such as surfactants or polymers. The modified nanoparticles are added into the growth solution containing the MOF precursors and subsequently the MOF shells are formed around the surfaces of the nanoparticles. With this method, several composites Au NP@HKUST-1,[116] Au NP@MIL-100(Fe),[117] and Pt NP@ZIF-8,[118] have been produced. Also, many other kinds of metal NPs such as (CdTe, Fe_3O_4, $NaYF_4$, Ag) have been encapsulated.[119]

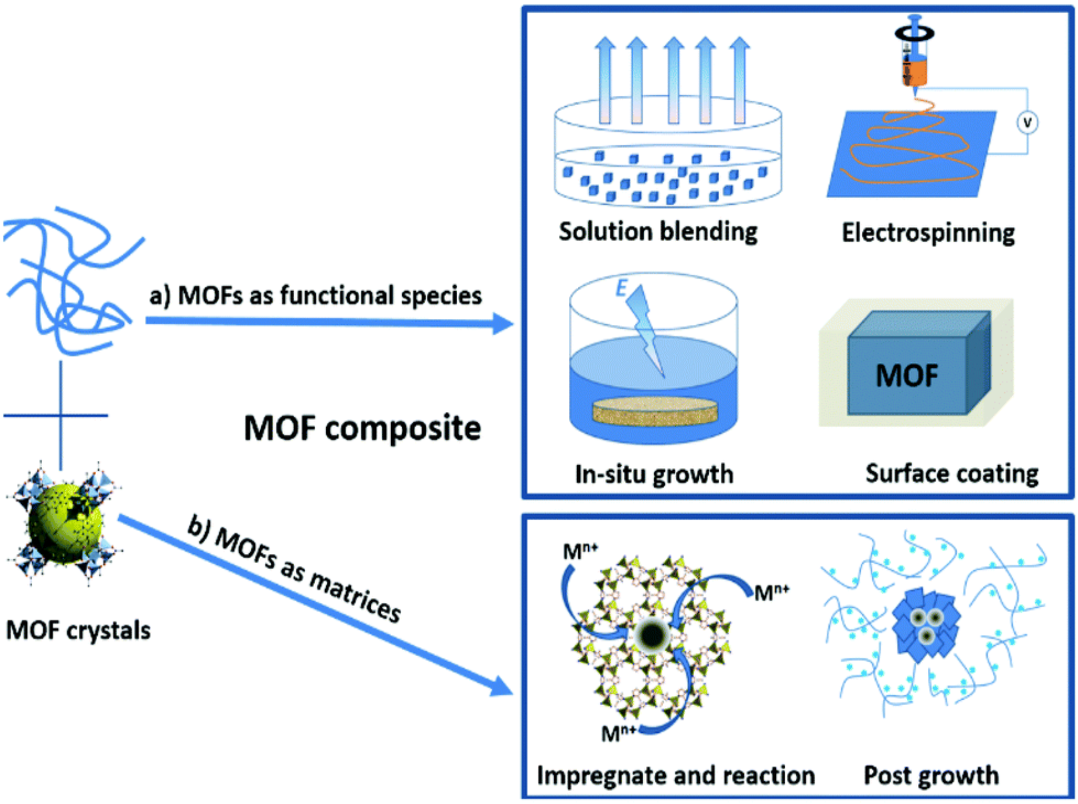

Figure 16. An overview of the MOF composites and their corresponding synthesis methods. The composites are categorized as (a) MOFs as functional species and (b) MOFs as matrix materials.

2.5. Applications of NMOF- based composites

In this section, main applications of NMOFs based composites are described.

2.5.1. Hydrogen storage

Hydrogen is considered an environmentally attractive energy carrier that enable a secure and clean energy future. However, the controlled storage and release of hydrogen in a safe and efficient way remains one of the most difficult challenges. When tasked with the preparation of metal nanoparticles-doped MOFs for enhance hydrogen storage, Yang and colleagues have demonstrated that MOF-5 and MOF-2 impregnated with Pd led to an increase of reversible hydrogen storage from 1.15 to 1.86 weight% and 1.03 to 1.48%, respectively, at 1 bar and 77 K.[120,121] Other composites have been made such as Pt-doped MOF/graphene oxide (GO), which was synthesized by the impregnation of colloidal Pt nanoparticle (NP). Their H_2 adsorption isotherms clearly show that the uptake on the Pt@HKUST-1/GO composites is better than HKUST-1 alone (**Figure 17**).[122]

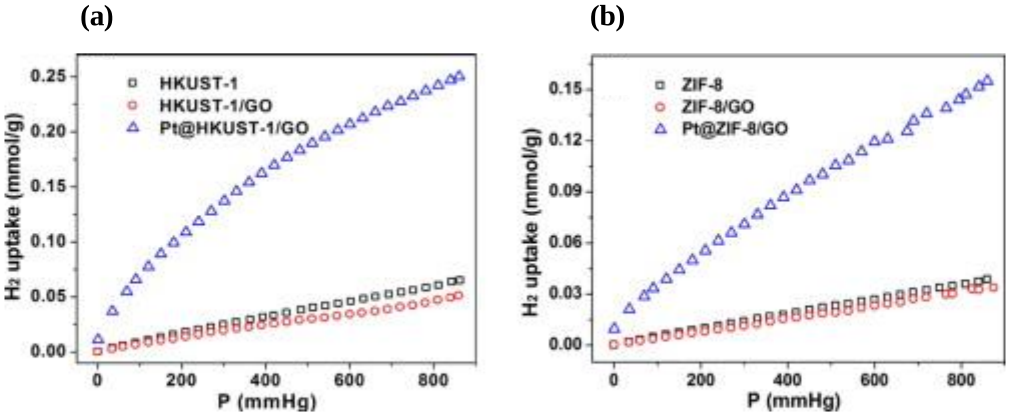

Figure 17. Hydrogen adsorption isotherms for (a) Pt@HKUST-1/GO and (b) Pt@ZIF-8/GO systems at 298 K.

2.5.2. Catalysis

Metal nanoparticles are highly attractive materials for catalysis due to the larger surface area/unit volume ratio as compared to their bulk metal analogues that are traditionally used in industrial catalysis.[123] However, there are still some major barriers for the widespread use of nanoparticles as catalysts. Some of these drawbacks include a tendency to aggregate, low recyclability, and difficulty recovering the nanoparticles from the reaction media. To overcome these problems, metal nanoparticles are typically immobilized on or in supports. A common strategy is to use porous materials with well-defined pore characteristics; in this way, the partition between the exterior and the interior pore structure permits the selective gating of the molecules that reach, and therefore react with the nanoparticles.[124] Porous materials also have the advantage of confining and protecting the nanoparticles, thus facilitating their recovery from the bulk solution and preventing particle aggregation. In this context, the regular porosity of MOFs together with the possibility to tailor their pore size, shape and chemical functionality makes them an excellent platform to support active metal nanoparticles for heterogeneous catalysis.[125]

In 2016, Paolo *et al.* summarized some reactions already tested using MOF-supported metal nanoparticles as catalysts, highlighting the nature of the MOF and the nanoparticle, the nanoparticle size, and the weight percentage of the nanoparticle in the MOF. The catalytic applications of NPs@MOFs composites are largely based on oxidation, hydrogenation, C–C coupling and H_2 production reactions.[79] Other catalysis involves also, complex cascade reactions involving Knoevenagel condensations and subsequent hydrogenations that were successfully catalyzed using IRMOF-3 supported Pd nanoparticles.[125]

In oxidation processes, MOF supported nanoparticles have shown good performances for carbon monoxide oxidation at elevated temperatures. For example, Xu, Hupp, and Gascón groups reported that Au and Pt nanoparticles supported in ZIF-8 and NH_2-MIL-101(Al) afford the total conversion of carbon monoxide to carbon dioxide at around 200 ºC.[126,127] Importantly, the reaction temperature can be reduced to 100–150 ºC by incorporating Pt, Pd and Cu nanoparticles within MIL-101 and Pd nanoparticles within MOF-5.[128,129]

Catalytic hydrogen generation begins with chemical hydrides, and the reaction speed can be controlled using metal nanocatalysts. The immobilization of metal nanoparticles (nanocatalyst) on MOFs surfaces to form composites, also has shown improvements on the catalytic effect. This was demonstrated with the hydrolysis of aqueous ammonia borane (NH_3BH_3),[130] with 2 wt% Pt@MIL-101 (an ultrafine Pt NPs (1.8 ± 0.2 nm) in the pores of MIL-101). The dehydrogenation reaction was completed within only 2.5 min.

We found also, an interesting example were combining two kind of NPs as Ni and Au into the MOF composite (AuNi@MIL-101) the catalytic hydrogen generation process is enhanced compared to using only Ni or Au NPs into the MOF composite (**Figure 18)**.[131]

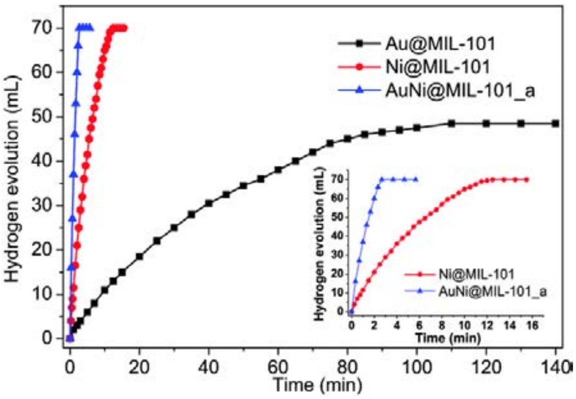

Figure 18. Plots of time versus volume of hydrogen generated from ammonia borane (NH_3BH_3). Hydrolysis at room temperature catalyzed by the Au@MIL-101, Ni@MIL-101 and AuNi@MIL-101 catalysts.

2.5.3. Other applications

The chemical and physical selectivity of MOFs composites can also provide a response to external stimuli such as heat, light and magnetic forces.

Some MOF composites, such as the core-shell Au NPs@MOF-5, in which a single Au NP core is coated with a uniform MOF-5 shell by impregnation method are considered to be chemo sensors due to the selectivity. The diameter of the Au NP core and the thickness of the MOF-5 were easily tuned by controlling the reaction conditions, and the results showed that nanoparticles are selective sensors of CO_2 in gas mixtures.[132] This study was followed through the surface-enhanced Raman scattering (SERS) due to a highly sensitive detection and selectivity of MOF-5 to CO_2 as well as by the Au NPs response to the SERS. An example of such a photoluminescent phenomenon is an luminescent europium-based MOF (EuOF) which was integrated with CdSe quantum dots (QDs) by impregnation. After impregnation, the composite was exposed to trinitrotoluene showing that the photoluminescence was quenched (**Figure 19**).[133]

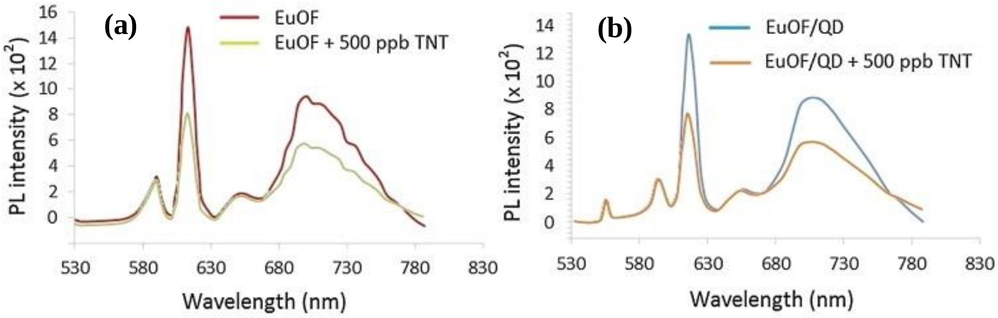

Figure 19. (a) PL spectra of 5 mg/mL dispersion of EuOF and the PL quenching effect in presence of 500 ppb TNT (b) PL spectra of 5 mg/mL dispersion of EuOF/QD and the PL quenching effect in presence of 500 ppb TNT; excitation wavelength = 300 nm.

In addition, luminescent MOFs have been used as sensors for detection of small molecules, including water because of water´s vibration nodes. Water is a typical quencher for luminescence, but actually the quenching is associated with the degradation of the MOF. The quenching allows monitoring the concentration of water by an intensity decrease of the luminescence. The luminesce MOF named $_{\infty}^{2}[Ln_2Cl_6(bipy)_3]\cdot 2bipy$ (where Ln is Eu, Tb, and bipy is 4,4′-bipyridine) and Fe_3O_4/SiO_2 microparticles were integrated into this application. The configuration consists of in a superparamagnetic core and a luminescent shell which has been tested to determine the presence of H_2O in different solvents (hexane and toluene). In this case, an emission/excitation intensity decrease was noted at the same water concentrations, but it was more prominent for toluene (**Figure 20**).[134]

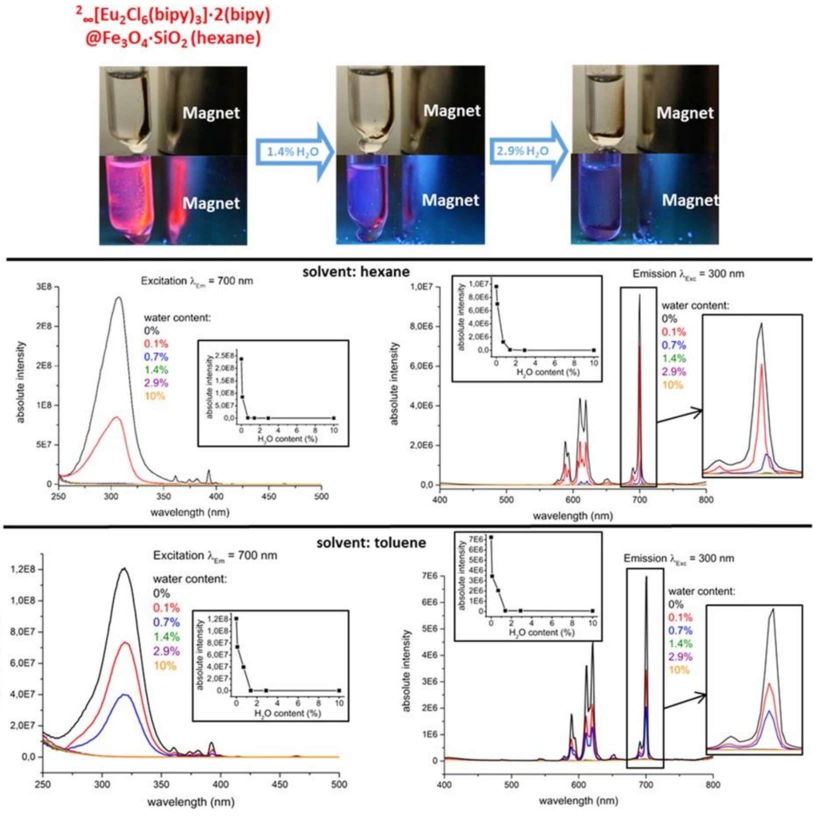

Figure 20. Exemplary detection of water with the composite particles $\infty 2[Eu_2Cl_6(bipy)_3]\cdot 2bipy@Fe_3O_4/SiO_2$: From magnetic harvesting of the red luminescent particles (top left) to the on-the-fly "turn-off" detection of the luminescence after contact with hexane (water content of 1.4% (top mid) and 2.9% (top right)). Referring excitation and emission spectra of the modified composite particles after contact with defined amounts of H_2O in hexane (mid) and toluene (bottom) and the quantitative determination of the reduction in excitation and emission intensity starting from 0.1% H_2O (insets depict the absolute course of intensity for increasing water concentrations).

In general, the combination NMOFs and magnetic materials such as ferromagnetic metal nanoparticles (*e.g.* Co, Ni and Fe), and superparamagnetic metal oxide nanoparticles (*e.g.* Co_3O_4, g-Fe_2O_3, and Fe_3O_4) appears to be of tremendous interest owing to the versatility of the functionalities.[79] Based on other applications, Doherty and coworkers engineered magnetic MOF composites with applications for pollutant remediation. In this case, magnetic nanofibers of cobalt and nickel ferrite were embedded into MOF-5. Then, the magnetic nanofibers were used for sequestration of polycyclic aromatic hydrocarbons (PAHs), such as 1,2-benzanthracene. Reasonably, this pollutant showed a high tendency to be absorbed into the porous crystal and to stack due to π–π interactions (**Figure 21**).[135]

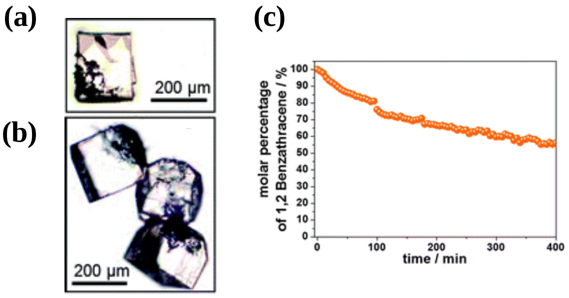

Figure 21. Optical image of framework composite crystals based on $NiFe_2O_4$ (a) and $CoFe_2O_4$ (b) fibers and MOF-5 showing the typical cubic crystal shape, and the partially or totally embedded fibers within the crystal. (c) A correlation between the detected intensity and the molarity has been used to calculate the 1,2-benzanthracene percentage change with time in the system where MOFs are sequestrating the four aromatic ring molecule.

Another interesting example is the integration of dyes into MOFs. For example, the red-light emitting dye 4-(p-dimethylaminostyryl)-1-methylpyridinium (DSM) and the green-light emitting dye acriflavine (AF) were encapsulated when mixed with the MOF ($(Me_2NH_2)_3[In_3(BTB)_4]\cdot 12DMF\cdot 22H_2O$ (ZJU-28)) solution precursors. These MOF⊃dye composites (ZJU-28⊃DSM/A) offered a great flexibility and potential to rationally design white phosphorus, and thus to develop high-performance white light-emitting diodes as shown in **Figure 22**.[136]

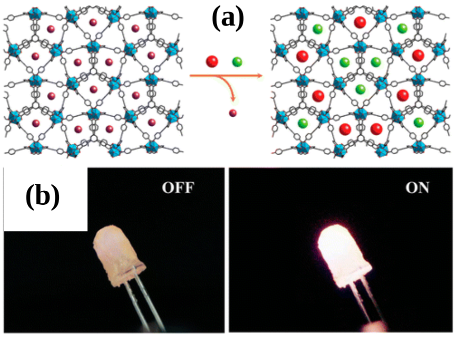

Figure 22. (a) Schematic illustration of the encapsulation of cationic dyes into ZJU-28 via ion-exchange process. (b) Photographs of the 365 nm ultraviolet LED coated with ZJU-28⊃DSM/AF (0.02 wt % DSM, 0.06 wt % AF) phosphor when the LED is tuned off and tuned on.

3. References

1 B. H. K. A., *Chem.,* 2008, 61–68.

2 H. J. Buser, D. Schwarzenbach, W. Petter and A. Ludi, *Inorg. Chem.*, 1977, **16**, 2704–2710.

3 H. M. P. J. H. RAYNER, *Nature*, 1949, **163**, 566–567.

4 T. M. andY. S. T. Iwamoto, T. Nakano, M. Morita, T. Miyoshi, *Inorg. Chim. Acta*, 1968, 313–316.

5 T. H. and Y. S. Y. Kinoshita, I. Matsubara, *Chem. Soc. Jpn.*, 1959, 1221–1226.

6 A. F. Wells, *Three-Dimensional Nets Polyhedra, Wiley, New York*, 1977.

7 B. F. Hoskins and R. Robson, *J. Am. Chem. Soc.*, 1990, **112**, 1546–1554.

8 O. M. Yaghi and H. Li, *J Am Chem Soc*, 1995, **117**, 10401–10402.

9 S. R. Batten, N. R. Champness, X.-M. Chen, J. Garcia-Martinez, S. Kitagawa, L. Öhrström, M. O'Keeffe, M. Paik Suh and J. Reedijk, *Pure Appl. Chem.*, 2013, **85**, 1715–1724.

10 H. Furukawa, K. E. Cordova, M. O'Keeffe and O. M. Yaghi, *Science*, 2013, **341**, 974.

11 S. Kitagawa, *Chem. Soc. Rev.*, 2014, **43**, 5415–5418.

12 M. O. F. Topologies, N. Stock and S. Biswas, *Chem. Rev.*, 2012, **112**, 933–969.

13 R. Ricco, L. Malfatti, M. Takahashi, A. J. Hill and P. Falcaro, *J. Mater. Chem. A*, 2013, **1**, 13033.

14 A. U. Czaja, N. Trukhan and U. Müller, *Chem. Soc. Rev.*, 2009, **38**, 1284.

15 J. R. Long and O. M. Yaghi, *Chem. Soc. Rev.*, 2009, **38**, 1213–1214.

16 H.-C. 'Joe' Zhou and S. Kitagawa, *Chem. Soc. Rev.*, 2014, **43**, 5415–5418.

17 C. Wang, X. Liu, N. Keser Demir, J. P. Chen and K. Li, *Chem. Soc. Rev.*, 2016, **45**, 5107–5134.

18 J. Liu, L. Chen, H. Cui, J. Zhang, L. Zhang and C.-Y. Su, *Chem. Soc. Rev.*, 2014, **43**, 6011–6061.

19 S. Li and F. Huo, *Nanoscale*, 2015, **7**, 7482–7501.

20 J. Lei, R. Qian, P. Ling, L. Cui and H. Ju, *TrAC - Trends Anal. Chem.*, 2014, **58**, 71–78.

21 M. Kondo, T. Yoshitomi, H. Matsuzaka, S. Kitagawa and K. Seki, *Angew. Chemie Int. Ed. English*, 1997, **36**, 1725–1727.

22 H. Li, M. Eddaoudi, T. L. Groy and O. M. Yaghi, *J. Am. Chem. Soc.*, 1998, **120**, 8571–8572.

23 H. Li, M. Eddaoudi, M. O'Keeffe and O. M. Yaghi, *Nature*, 1999, **402**, 276–279.

24 S. Pullen, H. Fei, A. Orthaber, S. M. Cohen and S. Ott, *J. Am. Chem. Soc.*, 2013, **135**, 16997–17003.

25 T. F. Liu, D. Feng, Y. P. Chen, L. Zou, M. Bosch, S. Yuan, Z. Wei, S. Fordham, K. Wang and H. C. Zhou, *J. Am. Chem. Soc.*, 2015, **137**, 413–419.

26 F. G. H. Deng, S. Grunder, K. E. Cordova, C. Valente, H. Furukawa, M. Hmadeh, A. C. W. ́ndara and J. F. S. and O. M. Y. Z. Liu, S. Asahina, H. Kazumori, M. O'Keeffe, O. Terasaki, *Science.*, 2012, **336**, 1018–1023.

27 O. K. Farha, I. Eryazici, N. C. Jeong, B. G. Hauser, C. E. Wilmer, A. A. Sarjeant, R. Q. Snurr, S. T. Nguyen, A. Ö. Yazaydın and J. T. Hupp, *J. Am. Chem. Soc.*, 2012, **134**, 15016–15021.

28 L. Schlapbach and A. Zuttel, *Nature*, 2001, **414**, 353–358.

29 O. K. Farha, A. Özgür Yazaydın, I. Eryazici, C. D. Malliakas, B. G. Hauser, M. G. Kanatzidis, S. T. Nguyen, R. Q. Snurr and J. T. Hupp, *Nat Chem*, 2010, **2**, 944–948.

30 H. Furukawa, N. Ko, Y. B. Go, N. Aratani, S. B. Choi, E. Choi, A. Ö. Yazaydin, R. Q. Snurr, M. O'Keeffe, J. Kim and O. M. Yaghi, *Science*, 2010, **329**, 424–428.

31 S. Ma, J. Eckert, P. M. Forster, J. W. Yoon, Y. K. Hwang, J.-S. Chang, C. D. Collier, J. B. Parise and H.-C. Zhou, *J Am Chem Soc*, 2008, **130**, 15896–15902.

32 J. L. C. Rowsell and O. M. Yaghi, *J. Am. Chem. Soc.*, 2006, **128**, 1304–1315.

33 https://www.iea.org/newsroomandevents/pressreleases/2016/march/decoupling-of-global-emissions-and-economic-growth-confirmed.html, 2015.

34 R. S. Haszeldine, *Science,* 2009, 1644–1645.

35 T. Li, J. E. Sullivan and N. L. Rosi, *J. Am. Chem. Soc.*, 2013, **135**, 9984–9987.

36 K. Sumida, D. L. Rogow, J. A. Mason, T. M. McDonald, E. D. Bloch, Z. R. Herm, T.-H. Bae and J. R. Long, *Chem. Rev.*, 2012, **112**, 724–781.

37 Y. Lin, Q. Yan, C. Kong and L. Chen, *Sci. Rep.*, 2013, **3**.

38 Q. Yan, Y. Lin, C. Kong and L. Chen, *Chem. Commun.*, 2013, **49**, 6873–6875.

39 S. Yang, J. Sun, A. J. Ramirez-Cuesta, S. K. Callear, I. F. DavidWilliam, D. P. Anderson, R. Newby, A. J. Blake, J. E. Parker, C. C. Tang and M. Schröder, *Nat Chem*, 2012, **4**, 887–894.

40 T. M. McDonald, J. A. Mason, X. Kong, E. D. Bloch, D. Gygi, A. Dani, V. Crocella, F. Giordanino, S. O. Odoh, W. S. Drisdell, B. Vlaisavljevich, A. L. Dzubak, R. Poloni, S. K. Schnell, N. Planas, K. Lee, T. Pascal, L. F. Wan, D. Prendergast, J. B. Neaton, B. Smit, J. B. Kortright, L. Gagliardi, S. Bordiga, J. A. Reimer and J. R. Long, *Nature*, 2015, **519**, 303–308.

41 E. D. Bloch, W. L. Queen, R. Krishna, J. M. Zadrozny, C. M. Brown and J. R. Long, *Science.*, 2012, **335**, 1606–1610.

42 F. Gándara, H. Furukawa, S. Lee and O. M. Yaghi, *J. Am. Chem. Soc.*, 2014, **136**, 5271–5274.

43 S. C. and R. B. P.D.C. Dietzel, R. E. Johnsen, H. Fjellvag, S. Bordia, E. Groppo, *Chem. Commun*, 2008, 5125–5127.

44 I. Spanopoulos, C. Tsangarakis, E. Klontzas, E. Tylianakis, G. Froudakis, K. Adil, Y. Belmabkhout, M. Eddaoudi and P. N. Trikalitis, *J. Am. Chem. Soc.*, 2016, **138**, 1568–1574.

45 w.-S. Y. and J. C. Y.-S. Li, F.-Y. Liang, H. Bux, A Feldhoff, *Angew. Chem. Int. Ed*, 2010, 548–551.

46 A. H. Chughtai, N. Ahmad, H. A. Younus, A. Laypkov and F. Verpoort, *Chem. Soc. Rev.*, 2015, **44**, 6804–6849.

47 R. Srirambalaji, S. Hong, R. Natarajan, M. Yoon, R. Hota, Y. Kim, Y. Ho Ko and K. Kim, *Chem. Commun.*, 2012, **48**, 11650–11652.

48 X. W. and C. D. W. Zhu, C. He, *Inorg. Chem. Commun*, 2014, **39**, 83–85.

49 A. Dhakshinamoorthy, A. M. Asiri and H. Garcia, *Chem. – A Eur. J.*, 2016, **22**, 8012–8024.

50 D. T. Genna, L. Y. Pfund, D. C. Samblanet, A. G. Wong-Foy, A. J. Matzger and M. S. Sanford, *ACS Catal.*, 2016, **6**, 3569–3574.

51 X. Li, R. Van Zeeland, R. V. Maligal-Ganesh, Y. Pei, G. Power, L. Stanley and W. Huang, *ACS Catal.*, 2016, **6**, 6324–6328.

52 P. V Dau and S. M. Cohen, *Chem. Commun.*, 2013, **49**, 6128.

53 A. Ferguson, L. Liu, S. J. Tapperwijn, D. Perl, F.-X. Coudert, S. Van Cleuvenbergen, T. Verbiest, M. A. van der Veen and S. G. Telfer, *Nat. Chem.*, 2016, **8**, 250–257.

54 X. Yu and S. M. Cohen, *Chem. Commun. (Camb).*, 2015, **51**, 9880–9883.

55 X. Zhang, Z. Zhang, J. Boissonnault and S. M. Cohen, *Chem. Commun.*, 2016, **52**, 8585–8588.

56 J.-M. Gu, W.-S. Kim and S. Huh, *Dalt. Trans.*, 2011, **40**, 10826–10829.

57 M. E. Davis, *Nature*, 2002, **417**, 813–821.

58 L. Zhang and T. J. Webster, *Nano Today*, 2009, **4**, 66–80.

59 F. Novio, J. Simmchen, N. Vázquez-Mera, L. Amorín-Ferré and D. Ruiz-Molina, *Coord. Chem. Rev.*, 2013, **257**, 2839–2847.

60 P. Horcajada, T. Chalati, C. Serre, B. Gillet, C. Sebrie, T. Baati, J. F. Eubank, D. Heurtaux, P. Clayette, C. Kreuz, J.-S. Chang, Y. K. Hwang, V. Marsaud, P.-N. Bories, L. Cynober, S. Gil, G. Ferey, P. Couvreur and R. Gref, *Nat Mater*, 2010, **9**, 172–178.

61 F. Novio, J. Lorenzo, F. Nador, K. Wnuk and D. Ruiz-Molina, *Chem. – A Eur. J.*, 2014, **20**, 15443–15450.

62 I. Imaz, D. Maspoch, C. Rodríguez-Blanco, J. M. Pérez-Falcón, J. Campo and D. Ruiz-Molina, *Angew. Chemie Int. Ed.*, 2008, **47**, 1857–1860.

63 A. Bousseksou, G. Molnár, L. Salmon and W. Nicolazzi, *Chem. Soc. Rev.*, 2011, **40**, 3313.

64 A. Carné, C. Carbonell, I. Imaz and D. Maspoch, *Chem. Soc. Rev.*, 2011, **40**, 291–305.

65 S. Vaucher, M. Li and S. Mann, *Angew. Chemie Int. Ed.*, 2000, **39**, 1793–1796.

66 G. Liang, J. Xu and X. Wang, *J. Am. Chem. Soc.*, 2009, **131**, 5378–5379.

67 S. Hou, C. C. Harrell, L. Trofin, P. Kohli and C. R. Martin, *J. Am. Chem. Soc.*, 2004, **126**, 5674–5675.

68 H. J. Lee, W. Cho and M. Oh, *Chem Commun*, 2012, **48**, 221–223.

69 E. a. Flügel, A. Ranft, F. Haase and B. V. Lotsch, *J. Mater. Chem.*, 2012, **22**, 10119.

70 Z. Ni and R. I. Masel, *J Am Chem Soc*, 2006, **128**, 12394–12395.

71 W.-J. Son, J. Kim, J. Kim and W.-S. Ahn, *Chem Commun*, 2008, 6336–6338.

72 Y. Pan, Y. Liu, G. Zeng, L. Zhao and Z. Lai, *Chem Commun*, 2011, **47**, 2071–2073.

73 A. Schaate, P. Roy, A. Godt, J. Lippke, F. Waltz, M. Wiebcke and P. Behrens, *Chem. - A Eur. J.*, 2011, **17**, 6643–6651.

74 R. G. Baraniuk, *Science (80-.).*, 2011, 717–719.

75 X. Yang and Q. Xu, *Cryst. Growth Des.*, 2017, **17**, 1450–1455.

76 P. Kumar, A. Deep and K.-H. Kim, *TrAC Trends Anal. Chem.*, 2015, **73**, 39–53.

77 I. J. H. and S. Q. H. Gou, G. Zhu, *J Am Chem Soc*, 2009, 1646–1647.

78 S. Rojas, F. J. Carmona, C. R. Maldonado, P. Horcajada, T. Hidalgo, C. Serre, J. A. R. Navarro and E. Barea, *Inorg. Chem.*, 2016, DOI: 10.1021/acs.inorgchem.6b00045.

79 P. Falcaro, R. Ricco, A. Yazdi, I. Imaz, S. Furukawa, D. Maspoch, R. Ameloot, J. D. Evans and C. J. Doonan, *Coord. Chem. Rev.*, 2016, **307**, **Part**, 237–254.

80 S.-M. Hu, H.-L. Niu, L.-G. Qiu, Y.-P. Yuan, X. Jiang, A.-J. Xie, Y.-H. Shen and J.-F. Zhu, *Inorg. Chem. Commun.*, 2012, **17**, 147–150.

81 F.-Y. Yi, D. Chen, M.-K. Wu, L. Han and H.-L. Jiang, *Chempluschem*, 2016, **81**, 675–690.

82 L. Liu, X. Chen, J. Qiu and C. Hao, *Dalt. Trans.*, 2015, **44**, 2897–2906.

83 V. Valtchev and L. Tosheva, *Chem. Rev.*, 2013.

84 M. Sindoro, N. Yanai, A. Y. Jee and S. Granick, *Acc. Chem. Res.*, 2014, **47**, 459–469.

85 K. C. Stylianou, I. Imaz and D. Maspoch, in *Encyclopedia of Inorganic and Bioinorganic Chemistry*, John Wiley & Sons, Ltd, 2011.

86 P. Falcaro, R. Ricco, C. M. Doherty, K. Liang, A. J. Hill and M. J. Styles, *Chem. Soc. Rev.*, 2014, **43**, 5513–5560.

87 C. W. J. and S. N. A. J. Brown, J. R. Jhonson, M. E. Lydon, W. J. Koros, *Angew. Chem. Int. Ed*, 2012, 10615–10618.

88 D. Tanaka, A. Henke, K. Albrecht, M. Moeller, K. Nakagawa, S. Kitagawa and J. Groll, *Nat Chem*, 2010, **2**, 410–416.

89 W. Cho, H. J. Lee and M. Oh, *J. Am. Chem. Soc.*, 2008, **130**, 16943–16946.

90 L. Zhang, Z. Kang, X. Xin and D. Sun, *Cryst. Eng. Comm.*, 2016, **18**, 193–206.

91 D. Zhao, Y. Cui, Y. Yang and G. Qian, *CrystEngComm*, 2016, **18**, 3746–3759.

92 S. R. Zhang, D. Y. Du, J. S. Qin, S. J. Bao, S. L. Li, W. W. He, Y. Q. Lan, P. Shen and Z. M. Su, *Chemistry*, 2014, **20**, 3589–3594.

93 V. Stavila, C. Schneider, C. Mowry, T. R. Zeitler, J. A. Greathouse, A. L. Robinson, J. M. Denning, J. Volponi, K. Leong, W. Quan, M. Tu, R. A. Fischer and M. D. Allendorf, *Adv. Funct. Mater.*, 2016, **26**, 1699–1707.

94 L. L. Da Luz, R. Milani, J. F. Felix, I. R. B. Ribeiro, M. Talhavini, B. A. D. Neto, J. Chojnacki, M. O. Rodrigues and S. A. Júnior, *ACS Appl. Mater. Interfaces*, 2015, **7**, 27115–27123.

95 G. Lu and J. T. Hupp, *J. Am. Chem. Soc.*, 2010, **132**, 7832–7833.

96 F. Hinterholzinger, C. Scherb, T. Ahnfeldt, N. Stock and T. Bein, *Phys. Chem. Chem. Phys.*, 2010, **12**, 4515–4520.

97 C.-Y. Sun, X.-L. Wang, X. Zhang, C. Qin, P. Li, Z.-M. Su, D.-X. Zhu, G.-G. Shan, K.-Z. Shao, H. Wu and J. Li, *Nat Commun*, 2013, **4**.

98 C. R. Wade, M. Li and M. Dincă, *Angew. Chemie Int. Ed.*, 2013, **52**, 13377–13381.

99 C.-W. Kung, T. C. Wang, J. E. Mondloch, D. Fairen-Jimenez, D. M. Gardner, W. Bury, J. M. Klingsporn, J. C. Barnes, R. Van Duyne, J. F. Stoddart, M. R. Wasielewski, O. K. Farha and J. T. Hupp, *Chem. Mater.*, 2013, **25**, 5012–5017.

100 K. Khaletskaya, J. Reboul, M. Meilikhov, M. Nakahama, S. Diring, M. Tsujimoto, S. Isoda, F. Kim, K. Kamei, R. A. Fischer, S. Kitagawa and S. Furukawa, *J Am Chem Soc*, 2013, **135**, 10998–11005.

101 Q.-L. Zhu and Q. Xu, *Chem. Soc. Rev.*, 2014, **43**, 5648–5512.

102 I. Ahmed and S. H. Jhung, *Mater. Today*, 2014, **17**, 136–146.

103 T. Ben, C. Lu, C. Pei, S. Xu and S. Qiu, *Chem. – A Eur. J.*, 2012, **18**, 10250–10253.

104 M. J. C. Ordoñez, K. J. Balkus, J. P. Ferraris and I. H. Musselman, *J. Memb. Sci.*, 2010, **361**, 28–37.

105 T. Bae, J. S. Lee, W. Qiu, W. J. Koros, C. W. Jones and S. Nair, *Angew. Chemie Int. Ed.*, 2010, **49**, 9863–9866.

106 E. V Perez, K. J. Balkus Jr, J. P. Ferraris and I. H. Musselman, *J. Memb. Sci.*, 2009, **328**, 165–173.

107 S. Basu, A. Cano-Odena and I. F. J. Vankelecom, *J. Memb. Sci.*, 2010, **362**, 478–487.

108 L. Fan, M. Xue, Z. Kang, H. Li and S. Qiu, *J. Mater. Chem.*, 2012, **22**, 25272–25276.

109 Y. Wu, F. Li, H. Liu, W. Zhu, M. Teng, Y. Jiang, W. Li, D. Xu, D. He, P. Hannam and G. Li, *J. Mater. Chem.*, 2012, **22**, 16971–16978.

110 M. L. Pinto, S. Dias and J. Pires, *ACS Appl. Mater. Interfaces*, 2013, **5**, 2360–2363.

111 D. Nagaraju, D. G. Bhagat, R. Banerjee and U. K. Kharul, *J. Mater. Chem. A*, 2013, **1**, 8828–8835.

112 Y. Cui, B. Chen and G. Qian, *Coord. Chem. Rev.*, 2014, **273–274**, 76–86.

113 B.-Z. Zhan and X.-Y. Li, *Chem Commun*, 1998, 349–350.

114 C.-Y. Sun, S.-X. Liu, D.-D. Liang, K.-Z. Shao, Y.-H. Ren and Z.-M. Su, *J. Am. Chem. Soc.*, 2009, **131**, 1883–1888.

115 J. Juan-Alcañiz, E. V Ramos-Fernandez, U. Lafont, J. Gascon and F. Kapteijn, *J. Catal.*, 2010, **269**, 229–241.

116 T. Tsuruoka, H. Kawasaki, H. Nawafune and K. Akamatsu, *ACS Appl. Mater. Interfaces*, 2011, **3**, 3788–3791.

117 F. Ke, J. Zhu, L.-G. Qiu and X. Jiang, *Chem Commun*, 2013, **49**, 1267–1269.

118 P. Wang, J. Zhao, X. Li, Y. Yang, Q. Yang and C. Li, *Chem Commun*, 2013, **49**, 3330–3332.

119 G. Lu, S. Li, Z. Guo, O. K. Farha, B. G. Hauser, X. Qi, Y. Wang, X. Wang, S. Han, X. Liu, J. S. DuChene, H. Zhang, Q. Zhang, X. Chen, J. Ma, S. C. J. Loo, W. D. Wei, Y. Yang, J. T. Hupp and F. Huo, *Nat. Chem.*, 2012, **4**, 310–316.

120 M. Sabo, A. Henschel, H. Frode, E. Klemm and S. Kaskel, *J. Mater. Chem.*, 2007, **17**, 3827–3832.

121 Y. E. Cheon and M. P. Suh, *Angew. Chemie Int. Ed.*, 2009, **48**, 2899–2903.

122 H. Zhou, J. Zhang, J. Zhang, X.-F. Yan, X.-P. Shen and A.-H. Yuan, *Inorg. Chem. Commun.*, 2015, **54**, 54–56.

123 L. LLoyd, *Handbook of Industrial Catalysts*, Springer US, Boston, MA, 2011.

124 J. R. A. D. Astruc, F. Lu, *Angew. Chem. Int. Ed.*, 2005, **44**, 7852.

125 R. A. F. S. Hermes, M.-K. Schröter, R. Schmid, L. Khodeir, M. Muhler, A. Tissler, R.W. Fischer, *Angew. Chem. Int. Ed.*, 2005, **44**, 6237.

126 Q. X. H.-L. Jiang, B. Liu, T. Akita, M. Haruta, H. Sakurai, *J. Am. Chem. Soc.*, 2009, **131**, 11302.

127 F. K. E.V. Ramos-Fernandez, C. Pieters, B. van der Linden, J. Juan-Alcañiz, P. Serra-Crespo, M.W.G.M. Verhoeven, H. Niemantsverdriet, J. Gascon, *J. Catal.*, 2012, 42.

128 Q. X. A. Aijaz, T. Akita, N. Tsumori, *J. Am. Chem. Soc.*, 2013, **135**, 16356.

129 A. B. W. Kleist, M. Maciejewski, *Thermochim. Acta.*, 2010, 71.

130 A. Aijaz, A. Karkamkar, Y. J. Choi, N. Tsumori, E. Rönnebro, T. Autrey, H. Shioyama and Q. Xu, *J. Am. Chem. Soc.*, 2012, **134**, 13926–13929.

131 Q.-L. Zhu, J. Li and Q. Xu, *J. Am. Chem. Soc.*, 2013, **135**, 10210–10213.

132 Y. L. and Z. T. L. He, Y. Liu, J. Liu, Y. Xiong, J. Zheng, *Angew. Chem. Int. Ed*, 2013, **52**, 3741–3745.

133 R. Kaur, A. K. Paul and A. Deep, *Forensic Sci. Int.*, 2014, **242**, 88–93.

134 T. Wehner, K. Mandel, M. Schneider, G. Sextl and K. Müller-Buschbaum, *ACS Appl. Mater. Interfaces*, 2016, **8**, 5445–5452.

135 C. M. Doherty, E. Knystautas, D. Buso, L. Villanova, K. Konstas, A. J. Hill, M. Takahashi and P. Falcaro, *J. Mater. Chem.*, 2012, **22**, 11470–11474.

136 Y. Cui, R. Song, J. Yu, M. Liu, Z. Wang, C. Wu, Y. Yang, Z. Wang, B. Chen and G. Qian, *Adv Mater*, 2015, **27**, 1420–1425.

Chapter 2

Objectives

As is demonstrated in the present introduction, the development of Metal organic frameworks have been very continuous and rapid in the past 20 years. The careful choice of the building blocks in the synthesis of Metal-Organic Frameworks (MOFs) have allowed to synthesis thousands of new structures. Over this period, a vast catalogue of MOFs with a great variety of structures and properties has been reported, which have been proposed for myriad applications such as gas sorption and catalysis. Beyond the improvements that an adequate design can induce in the MOF properties, the optimization and the presence of MOFs in new applications is also coming from their combination with other type of materials, thereby creating composites. The interest on these composites is recent but the potential high. In this context, the main objective of this thesis has been the exploration and the development of new methodologies to prepare original and multifunctional MOF based composites that combine the intrinsic porosity of MOFs and other properties incorporated through other materials such as magnetism, fluorescence, and catalysis among others.

Two main research line have been opened in this thesis. First, we proposed a novel methodology, based on the desymmetrization at surfaces, to prepare MOF based Janus nanoparticles. As we reported before, most of the resulting MOF-based composites are isotropic core–shell materials in which the metallic component is embedded within the MOF. To date, no suitable method for the preparation of submicron-sized metallic Janus particles comprising single MOF particles has been described. Thus, in the first part of this thesis we aim to implement a precise general strategy to synthesise MOF based Janus nanoparticles. This strategy has been organised around five partial objectives:

- Selection and synthesis of MOFs with highly monodispersity to get homogeneous colloidal dispersion.
- Deposition of highly monodisperse MOFs on surfaces to form homogeneous monolayers of MOF nanocrystals
- Deposition of metals on an MOF monolayer trough E-beam Evaporation, to cover selectively the surface of MOFs
- Detachment of Janus metal@MOF particles from the substrate,
- Evaluation of the extension of the strategy to different MOF and metals and the study of functionalities of Janus metal@MOF particles.

Second, in this thesis we also aim to synthesis composites combining MOFs with functional molecules. Beyond the use of general absorption and postsynthetic modification methods, in this part of the Thesis, the functional molecules into the MOFs have been integrated by in-situ defect creation using functional molecules with coordinative capacities. This strategy has been organised around three partial objectives:

- Synthesis and characterization of Xylenol Orange@MOF by in situ defect creation on MOF in presence of xylenol orange (XO) co-precipitation
- Optimization of the maximum integration of XO chelating agents into the MOFs.
- Evaluation of removal capacity of a heavy metal ion such as Gd^{3+} by the synthesized XO@MOF composite.

Chapter 3

Introducing asymmetric functionality into MOFs via the generation of metallic Janus MOF particles

1. **Janus Particles**

The Janus particles (JPs) term comes from the ancient Roman god “Janus” and represents the beginnings and transitions (**Figure 1** centered image). The term of JPs was introduced for the first time to the scientific community by Pierre-Gilles de Gennes, who received the Nobel Prize in physics in 1991.[1,2,3] JPs are defined as a type of multicompartmental and asymmetric particles whose surface has two chemically distinct regions. This characteristic confers anisotropy in terms of shape, size, reactivity, and directionality providing functions not possible for particles with uniform composition.

Figure 1 summarizes the different configurations that JPs can adopt. The first type are JPs with a spherical shape, which half of the particle has a different composition. This type of JPs is also known as bicompartmental particles (**Figure 1**a**)**. The second type of JPs are spherical half raspberry like particles, where unimolecular micelles or NPs are on the half site of the JPs (**Figure 1**b**)**. The third class are snowman-like particles, which show asymmetry in both size and composition (**Figure 1**c**)**. Finally. **Figure 1**d-e illustrates two types of cylindrical JPs.

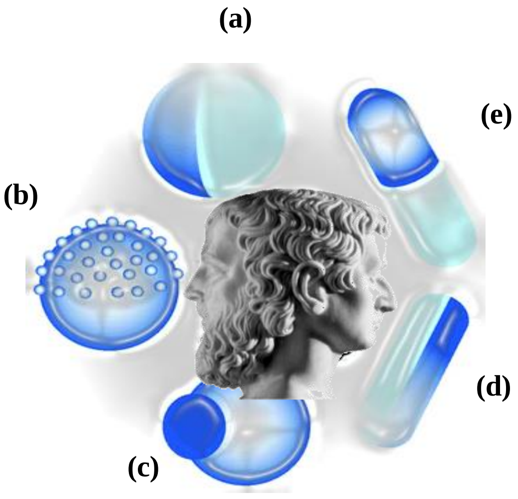

Figure 1. Schematic illustration of the two-faced Roman god Janus (middle) and **JPs** of different morphologies and shapes.

1.1. Approaches for fabricating Janus Particles

JP synthesis is still a major challenge that often requires complex and ingenious strategies. During recent years several methods have been described to synthesize JPs with specific geometries, shapes and compositions.[4,5,6,7,18] These different strategies can be grouped into three main categories: self-assembly, masking and phase separation, schematically represented in **Figure 2**.[8,7]

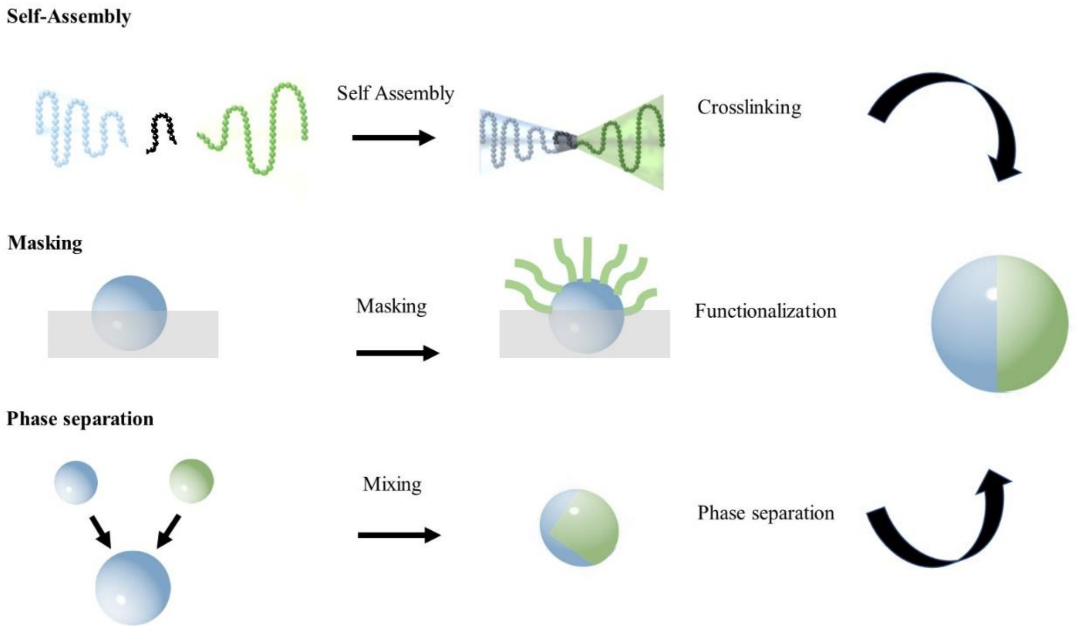

Figure 2. Schematic representation of the three general synthetic strategies used to make of JPs: Self-Assembly, Masking, and Phase separation.

1.1.1. Self-Assembly

Historically, self-assembly has been the first approach used to prepare JPs. Self-assembly describes the spontaneous arrangement of building blocks (polymers or ligands) into larger structures with well-defined symmetry, complex architecture, and long-range order. To date, different JPs have been synthesized by controlling the parameters that influence the self-assembly processes, such as temperature, polarity, pH and ionic strength. There are two main self-assembly strategies have been followed to prepare JPs: (i) the self-assembly of block copolymers; and (ii) the competitive adsorption of incompatible ligands.[9]

A well-known property of block copolymers is that they phase-segregate into distinct domains in selective solvents or in bulk. For this reason, the self-assembly of block copolymer is a very used tool in soft matter nanotechnology to create a multitude of precisely defined structures in bulk and thin films. In the case of JPs, the idea consists on controlling the self-assembly of block copolymers in solution, or on surfaces. Then, “freeze-in” one part of the micelle to obtain asymmetric nanoparticles (**Figure 3**).

In a general experiment, the self-assembly of block copolymers is first induced in solution or in a film. Then, the blocks are crosslinked and finally, the JPs are obtained by a dissolution of one of the components. Following this route, the first results were published by Müller's group in 2001, in which crosslinked Janus polymer NPs were prepared by the self-assembly of terpolymers.[10] They sefl-assembled a triblock polymer from polymethylacrylate (PMMA), polystyrene (PS) and low-molecular-weight polybutadiene. In this polymer, PS and PMMA formed alternating lamellae, and polybutadiene formed small spheres located in between the lamellae (**Figure 3**a). The blocks were then crosslinked and dissolved in THF, yielding spherical JPs with a polybutadiene core and PS on one face and PMMA on the other. Recently, the same authors also explored to get different JPs staring from differentes architectures.[10] By changing the molecular weight of the blocks, two other JPs were obtained, including as lamellae-cylinders[11] and fully lamellar structures (**Figure 3**b).[12]

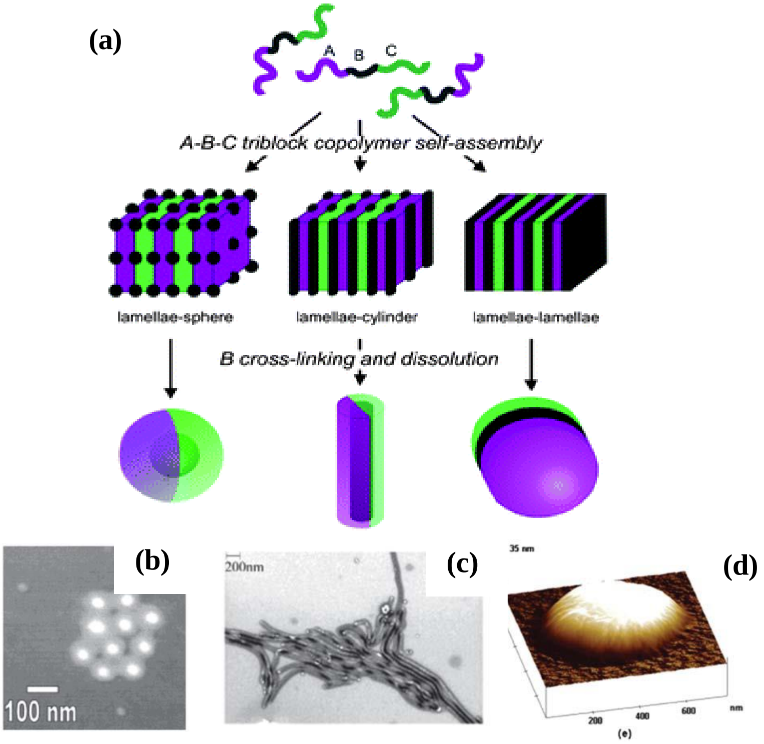

Figure 3. (a) Schematic of the preparation of JPs from triblock copolymers. The process starts with the self-assembly of the triblock copolymers, followed by cross-linking from and by a dissolution process. (b) SFM image of spherical Janus micelles, (c) SEM images of Janus cylinders, (d) 3D-plotted SFM image of a Janus disk.

The introduction of different chemical or physical properties of polymers or surfactants can also induce different self-assemblies and spontaneous symmetry breaking. This strategy, called competitive adsorption of mixtures of ligands, is based on the adsorption of incompatible molecules on the surface of nanoparticles that is followed by a spontaneous rearrangement of these molecules on the surface of the NPs and a symmetry breaking that leads to JPs. Following this approach, Vilain *et al.* used a set of two ligands phosphinine and thiol ligands with little affinity between them. Ligands like phosphinine come from π-stacking, thus further increasing the tendency to phase segregate. Moreover, the electronic interactions of both ligands with the Au atoms were very different. Whereas phosphinines are strong electron acceptors, thiols behave as electron donors. With these differences, after the functionalization of a Au NPs with both ligands, their incompatibility resulted in a spontaneous phase separation on the surface of the NPs. Careful monitoring of the plasmon peak upon ligand exchange reactions using the same parent Au-NPs revealed an unprecedented blue-shift for the mixed ligand systems in comparison with the homogenously functionalized Au-NPs these differences were attributed to bipolar partitioning of the ligands around the particle (**Figure 4**).[13] Chen *et al.* also utilized the competitive coordination of incompatible ligands, Poly acrylic acid (PAA) and 4-mercaptophenylacetic acid (MPAA) in a propanol-water solution in order to create an asymmetric functionalization on the surfaces of Au NPs. Silica was grown only on the portion of the surface of Au NPs covered by MPAA, since PAA inhibits SiO_2 nucleation. Additionally, the authors showed that Ag could be grown on the exposed Au portions of the Au-SiO_2 heterodimers, creating Ag-Au-SiO_2 trimers.

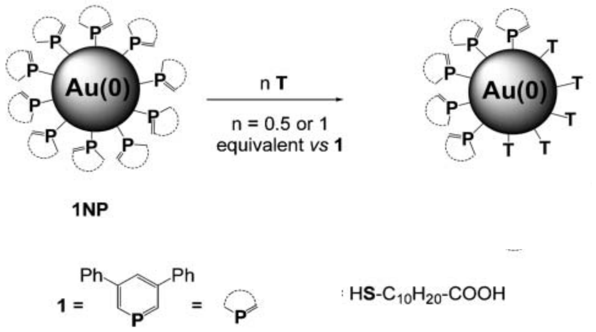

Figure 4. Scheme of the synthesis of Au JPs by partial substitution of phosphinine (1) with T; thiol.

1.1.2. Masking

Masking technique is undoubtedly the most intuitive method to prepare JPs. In this approach, the asymmetric functionalization of the particles is achieved by exposing only a portion of their surface to the environment. Where the reaction is carried out, while the remaining part of the surface is protected. The major advantage of this approach is that it is applicable to virtually any type of material, offering the possibility to modify the surfaces of the particles with a very wide variety of functional groups.

The masking of particles can be achieved by depositing them or adsorbing them on a solid surface, or trapping them at the interface between two fluid phases. Thus, this process can be classified in terms of the way used for immobilizing the NPs and enable their asymmetric functionalization: hard substrates, soft flat substrates, particle dispersion, and Pickering emulsion (**Figure 5).**

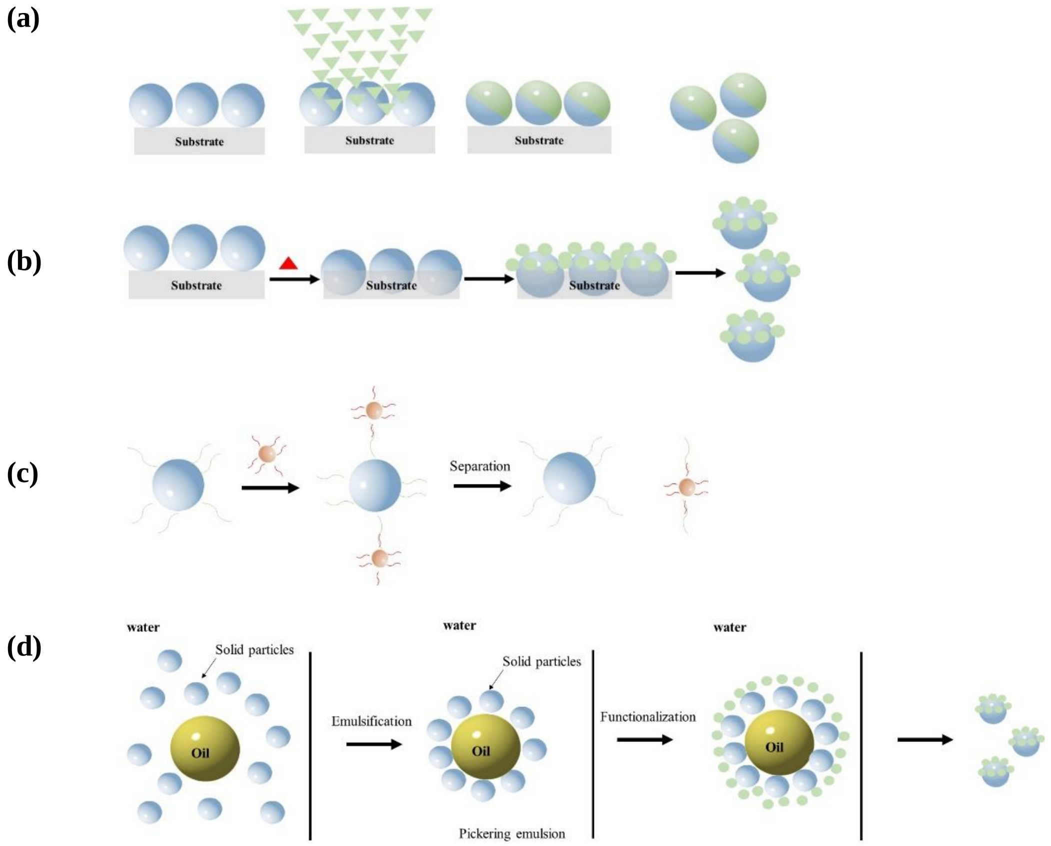

Figure 5. Schematic representation of the masking process using a) hard substrates, b) soft flat substrates, c) particles dispersion, d) Pickering emulsion.

The use of masking to functionalize micrometer-sized JPs was first reported by Shimizu *et al*., who evaporated gold on large latex spheres that were previously deposited on a hard substrate (glass substrate) (**Figure 6**a-e). Then, they used this adhered gold to chemisorb a thiol modified molecule from a liquid phase.[14] Few years after, Whitesides *et al*. reported the first example of sub-micrometer JPs using an analogous technique. They drop-casted silica particle suspensions on a glass surface and then, they partially coated these particles with gold, palladium, titanium or platinum layers.[15] Also, they prepared half-micron sized heterodimers by first depositing a layer of gold onto the silica spheres lying on a planar surface and then, by annealing them at high temperature at 700 ◦C for a few hours. During annealing, the gold layer on a particle surface, which initially formed a hemisphere, beaded up into a microcrystal by a dewetting process that consumed the thinnest part of the layer first (**Figure 6**f).

The use of hard substrates to prepare JPs by masking offer many possibilities because they are applicable for a variety of particle materials (silica and polymers), which can be immobilized on different hard substrates (glass substrates, silicon wafer) and functionalized by the evaporation of many different metals such as Ti, Ag, Ni, and Co[16] and the attachment of substances in liquid. For example, Velegol *et al.* reported the coating of microsized polystyrene particles by other nanoscopic particles. The method consisted on the preparation of positively charged silica particles, which were electrostatically adsorbed on a glass substrate in order to protect a portion of their surface. Subsequent addition of negatively charged sulfate colloidal latex nanoparticles resulted in decoration of the exposed silica particle surfaces. The procedure could be repeated multiple times, by first reversing the charge of the JPs through the addition of poly acryl amide, followed by addition of more negatively charged particles (**Figure 6**g).[17]

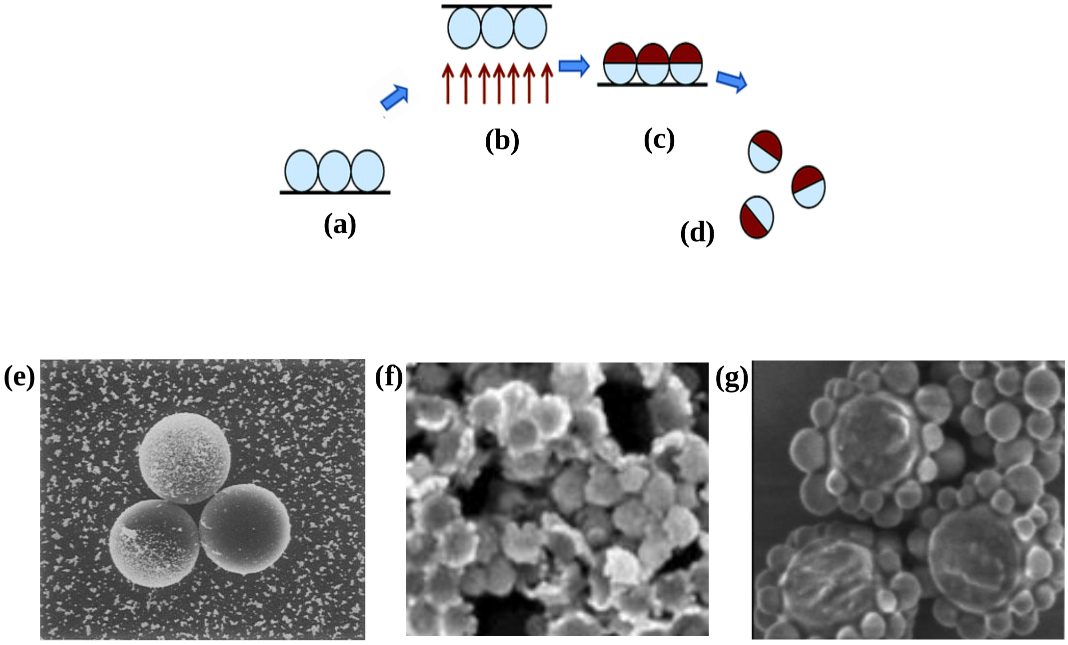

Figure 6. (a-d) Schematic illustration showing the fabrication of half-coated JPs by vapor deposition, (e) Representative SEM image of three 20 µm Janus Au-latex spheres. (f) FESEM image of 8 nm thick gold half-shells (100 nm diameter), (g) FESEM image of 520 nm amidine-functionalized of silica nanoparticles patterned.

The functionalization of non-masked surfaces can also be carried out using stamping methods. In this procedure, the particle monolayer is deposited on a substrate. Then, a elastomer stamp is “inked” with molecules, and then pressed against a monolayer of particles to transfer the “ink” to the exposed surface of the particles. The “ink” molecules may directly react with the particle surfaces or non-specifically adsorb onto the particles (**Figure** 7a).[18] The resulting JPs are partially peeled all from the surface. A major advantage of this method is that does not require an expensive and specialized equipment, and it allows various sizes of the patch created on the JPs.[19] For example, Cayre *et al.* fabricated dipolar JPs using the microcontact printing of cationic surfactants onto immobilized negatively charged PS beads. For this purpose, they deposited a monolayer of PS latex particles onto a glass slide, which was subsequently lifted with 1% glucose solution in water and redried to produce a film of glucose with a monolayer of latex particles protruding from its surface. The glucose film stuck the particles to the glass interface and protected the bottom part of the particle surface from exposure to the surfactant during the stamping. Subsequently, octadecyltrimethylammonium bromide in ethanol was spread on the surface-modified polydimethylsiloxane stamp and applied onto the PS latexes (**Figure** 7a). The surfactants adhered via *electrostatic interaction*s, and the successful preparation was visualized via fluorescence microscopy of the redispersed fluorescently tagged JPs (**Figure** 7b).[19]

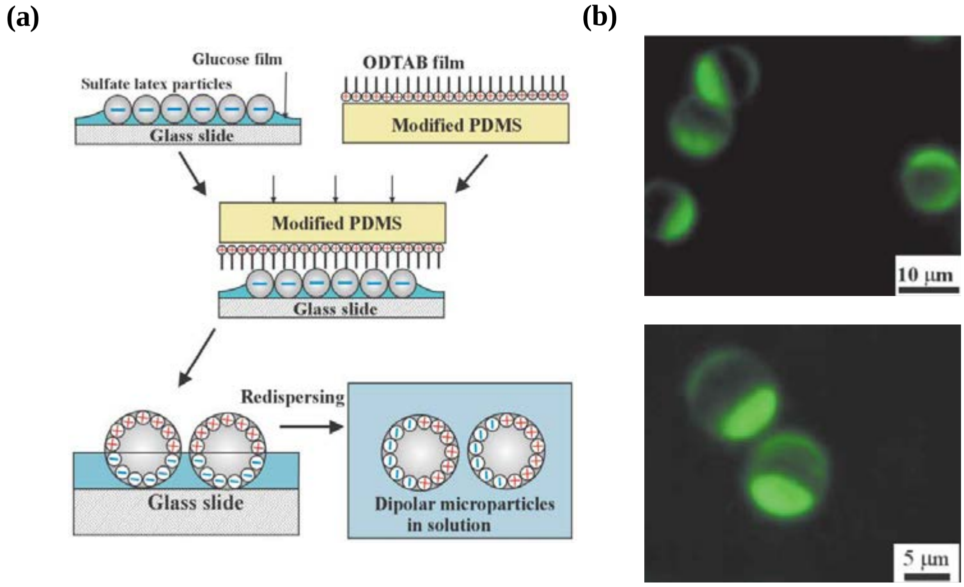

Figure 7. (a) Scheme of the preparation of dipolar colloid particles by microcontact printing of water-insoluble cationic surfactant octadecyltrimethylammonium bromide (ODTAB) on a monolayer of sulfate latex particles. (b) High magnification fluorescent microscopy images of 9.6 µm sulfate PS latex particles stamped with a film of Neuro Dio (hydrophobic fluorescent cationic dye) deposited on an elastomer stamp, and redispersed in milliQ water. The anionic and cationic amphiphilic molecules stick equally well on the PS latex particles predominantly due to hydrophobic interactions with the PS surface.

Hard substrates such as glass or silicon surfaces can also replaced by soft-flat substrates, in which adsorbed particles can be trapped by a curation process. In this case, one portion of the particle is trapped on the polymer, whereas the other part is exposed to a reaction media enabling its functionalization (**Figure 8**a). Ho *et al.* used PMMA-co-poly(4-vinylpyridine) (P4VP) fibers to electrostatically adsorb silica particles on their surfaces (**Figure 8**b). Then, the particles were trapped inside the polymer matrix and cured by increasing the temperature. The exposed surfaces of the silica particles were silanized, and gold colloids were asymmetrically adsorbed on them. Finally, the JPs of Au@Silica particles were recovered by dissolving the polymer fibers in co-solvent of acetone/ethanol (**Figure 8**c).[20]

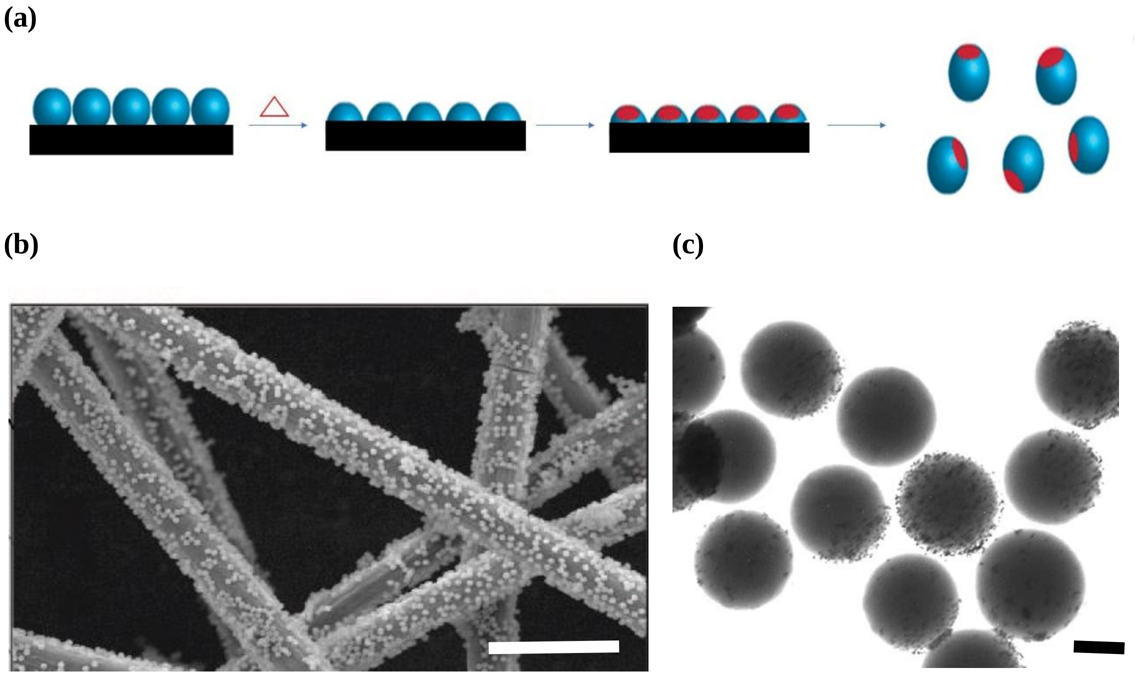

Figure 8. (a) Schematic representation of the synthesis of JPs using soft-flat substrates, b) Representative SEM image of silica particles adsorbed on polymeric fiber surfaces. Scale bar; 10 µm, and (b) TEM images of silica colloids hemispherically coated with Au NPs. Scale bar: 0,2 µm.

Another way of making JPs is using particles as masking agents. Hatton *et al.* applied this approach to synthesise polymer-coated magnetic JPs. For this purpose, they synthesised monodisperse 8-10 nm magnetic nanoparticles, which were coated with a uniform brush of polyacrylic acid (PAA) grown *via* surface-initiated atom transfer radical polymerization. To prepare the JPs, monolayers of the negatively charged PAA coated magnetic nanoparticles were adsorbed electrostatically onto positively charged silica beads. Amino-end functionalized polymers, either charged or temperature responsive, were then anchored to the non-masked hemispheres of the nanoparticle surfaces using amidation chemistry. The polymer coated magnetic JPs were finally recovered by increasing the pH of the solution, which reversed the charge on the silica beads and repelled the adsorbed nanoparticles. A schematic of the procedure is shown in **Figure 9**.[21]

Also, JPs can be created from particles by functionalizing the nanoparticles when they contact the surface of a bigger particle. In other words, the bigger particle act as a stamp. Mirkin group was pioneer developing this procedure to asymmetrically functionalize nanoparticles using oligonucleotides.[22] They used the sequence-dependent differences in the melting points of DNA double helices in combination with an intermediate immobilization on targets for desymmetrization. Precisely, 7-mer oligonucleotide-modified SiO_2 particles were first hybridized with 27-mer oligonucleotides, which showed a 7-mer complementary sequence at one end. Subsequently, Au-NPs carrying a 12-mer oligonucleotide were attached to the 20-mer overhanging ends of the SiO_2 beads, leading to complementary double helix formation of a few oligonucleotides on the bound Au-NP hemisphere. Afterwards, the remaining non-immobilized oligonucleotide parts of the free faces of the Au-NPs were blocked by hybridization with free 12-mers. Because the melting point of the complementary region of the 7-mer (silica bead) and the 12-mer (Au-NP) differed by 12 °C, it was possible to deliberately release the asymmetrically modified AuNPs from the SiO_2 targets *via* simple control of the temperature. The intermediately introduced 27-mer oligonucleotides were thus transferred onto one hemisphere of the AuNP, yielding free sticky ends.[23]

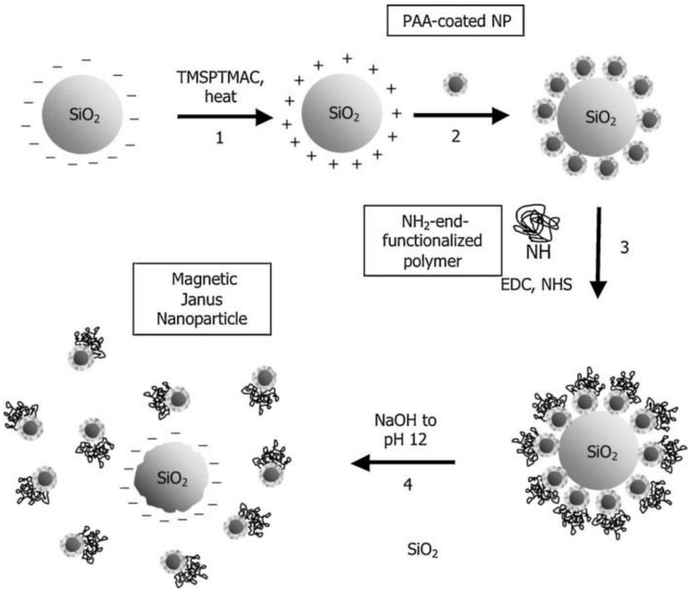

Figure 9. Schematic of the masking procedure for the asymmetric functionalization of PAA-coated magnetic nanoparticles.

Finally, asymmetric functionalization of nanoparticles can also be obtained by confining them at the interface between two fluids. In this case, masking generally occurs at the interface of a droplet in a normal emulsion or in a Pickering emulsion (stabilized by solid particles which are adsorbed onto the interface between two phases; hydrophilic and hydrophobic). Then, the solid particles surfaces exposed to the interfaces can be functionalized to form the JPs.[24] Among them, the utilization of Pickering emulsions as immobilization strategy has been a considerable advance regarding the preparation strategies of JPs, allowing today a easy access to a large quantity of (sub) micrometer JPs *via* simple solution-phase chemistry. For example, Gu *et al.* prepared silver magnetic heterodimers by first creating colloidosomes, *i.e.*, a Pickering water emulsion of oil droplets stabilized by either magnetite or FePt nanoparticles, and then nucleating silver nanoparticles in the aqueous phase. The second particle nucleation proceeded through the catalytic reduction of silver ions (**Figure 10**a).[25]

One of the limitations of using Pickering emulsions is the rotational diffusion or the resorption-desorption process observed on the surface of the droplet. Granick *et al.* solved this problem using wax as the oil phase in the oil-in-water emulsion. In this case, after the initial formation of the Pickering emulsion at high temperature (when the wax is liquid), the emulsion is cooled, inducing the solidification of the wax and entrapping the silica beads at the interface. Then, the particles are totally immobilized at the surface of wax droplets. Furthermore, non-adsorbed silica beads, if any present, can be easily separated from the wax Pickering dispersion *via* filtration.

Using this method, the successful silane-mediated binding of amine groups on the exposed surface of immobilized silica particles on the Pickering emulsion droplets was demonstrated. In addition, after liberation of the trapped silica particles via dissolution of the wax phase, the newly exposed surfaces could be further reacted with a hydrophobic silane to create hydrophobic/cationic Janus beads. The successful preparation was shown via fluorophore binding and subsequent fluorescence microscopy (**Figure 10**b).[26]

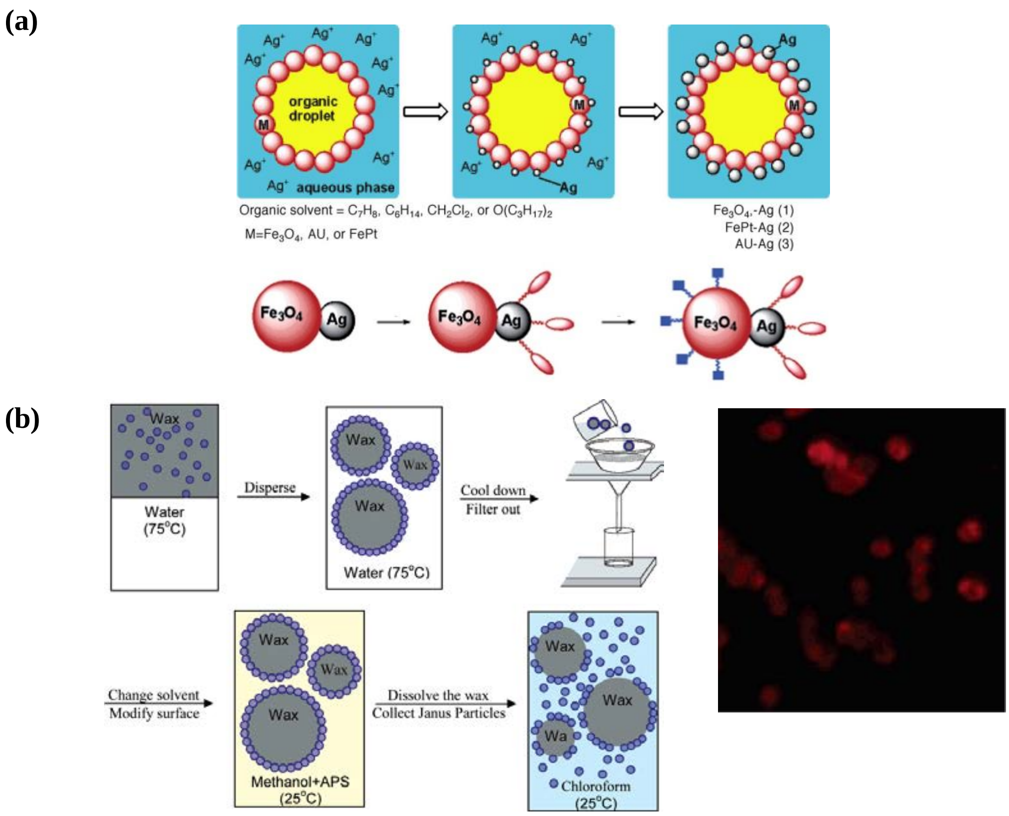

Figure 10. (a) Schematic of the preparation of various M-Ag heterodimers, with M denoting FePt, Au, or Fe_3O_4 nanoparticles. A colloidosome of an organic solvent droplet stabilized by M nanoparticles is first prepared, followed by nucleation of Ag nanocrystals in the aqueous phase on the outer side of the colloidosome, leading to the formation of the heterodimers. (b) Schematic procedure used to create JPs by functionalizing particles adsorbed onto wax-in-water emulsion and then cooling the sample so that the wax solidifies (left). Epifluorescence image of the obtained JPs (right). The particle diameter was 1.5 µm.

1.1.3. Phase separation

The third general method for the preparation of JPs relies on the phase separation of two or more incompatible components in a mixture. JPs by phase separation can be induced by the chemical reactions or crystallisation within core-shell inorganic particles, by evaporation or seeded polymerization in emulsion and by electrodynamic jetting.

Phase separation was first exploited on inorganic nanoparticles. The mechanism consists on the epitaxial growth of one particle from the surface of another. In this method, a core-shell particle is initially formed, in which the core works as a seed. The intrinsic incompatibility of the crystal lattices of the two materials makes difficult that the second material maintains a stable core-shell structure, leading to a phase separation and the formation of inorganic heterodimers. Using this approach, Gu *et al.* reported the synthesis of PtFe-CdS heterodimers. After PtFe particles were prepared, their surfaces were coated homogeneously with sulfur and then, they were reacted with a cadmium precursor to form a metastable core-shell particle. A high temperature treatment leaded to a reorganization of the crystalline lattices forming heterodimers (**Figure 11**a).[27] Similar procedures have been also utilized by Kwon *et al.* for the synthesis of Fe_2O_3-CdS JPs[28] and by Selvan *et al.* the synthesis of Fe_2O_3-CdSe and other semiconductor materials, such as zinc and lead sulphides.[29]

The phase separation can also be induced or accelerated by a chemical reaction. For example, molecular iodine I_2, which is a strong oxidant towards metallic silver, can be used to induced the phase separation of Ag-silica particles. Here, the precursor core-shell particles were first prepared from Ag nanoparticle dispersions and tetraethylorthosilicate. In such conditions, the silica shell is known to be microporous. Therefore, chemical exchanges between Ag cores and iodine were possible, leading to a rapid evolution from the Ag-silica core-shell morphology to AgI-silica snowman like morphology (**Figure 11**b).[30]

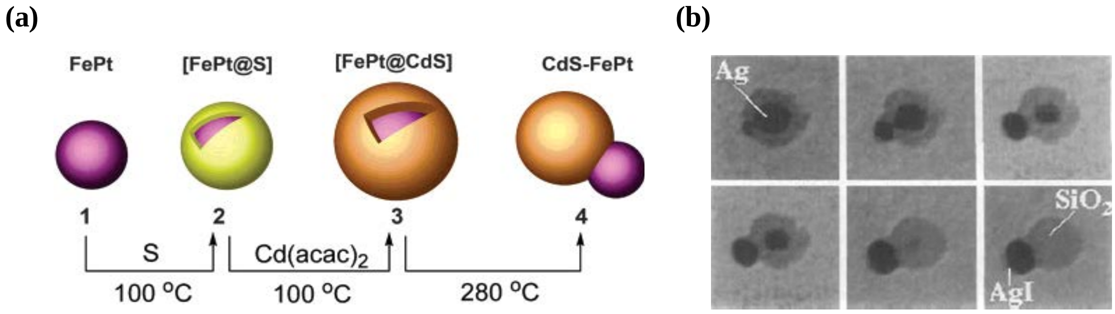

Figure 11. (a) Schemes showing the preparation of CdS-FePt heterodimers. A FePt nanoparticle (1) is first coated with elemental sulfur (2), followed by reaction with cadmium acetylacetonate, leading to a uniformly coated FePt@CdS particle (3). A final high temperature annealing leads to the formation of the heterodimer (4). (b) TEM images of a single 30-nm Ag–silica particle as a function of the time after exposure to 2 mM I_2. The final image was taken about 20 min after the first one.

Beyond the use of inorganic nanoparticles as templates to grow JPs, the phase separation can also be induced in emulsions. For example, when a mixture of incompatible homopolymers is confined inside an emulsion droplet, a phase separation can be expected. In this sense, the work developed by Okubo *et al.* was pioneering on the investigation of phase separation of PS/PMMA homopolymer mixtures inside microemulsion droplets.[31] They fabricated a surfactant-stabilized emulsion droplets of toluene containing PS and PMMA homopolymers. Then, the phase segregation was induced by the evaporation of the toluene. This phase segregation could be modulated using different surfactants and their concentration. Using this methodology, thereafter prepared micrometer-sized, monodisperse, and “mushroom-like” polymeric JPs (**Figure 12**).[31] These JPs were formed in two steps. The first step was the preparation of spherical PMMA/poly(styrene-2-(2-bromoisobutyryloxy)ethyl methacrylate) (P(S-BIEM)) JPs based on the internal phase separation induced by solvent evaporation from the solvent droplets dissolving the polymers. The second step was surface-initiated by atom transfer radical polymerization (ATRP) of 2-(dimethylamino)ethyl methacrylate (DM) using the JPs with ATRP initiator groups at one side of the surface as macroinitiator. As a consequence, mushroom-like PMMA/P(S-BIEM)-graft-poly(DM) JPs were prepared.

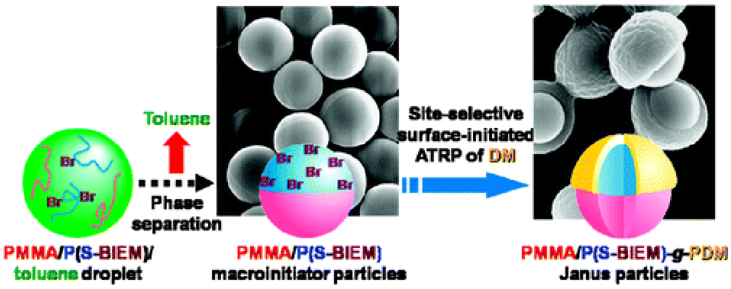

Figure 12. Scheme for synthesis of mushroom-like JPs by the phase separation in emulsion.

Microemulsions can also be used as reactors for polymerizations. Thus, they can also be used to generate JPs by seeded-growth emulsion polymerization. In this method, after the preparation of an initial latex particles, which will act as a seed, the polymerization is continued by the addition of a second monomer. The occurring polymerization of the second polymer within the latex seed leads to the onset of phase separation and, under feasible conditions, to the development of completely phase-separated latex particles. This process was first applied to the preparation of acrylic composite particles containing a hard PMMA part and a soft poly n-butylacrylate (PnBuA) side. By emulsion polymerization (using different monomers at different stages in a seeded emulsion polymerization) of straight acrylic composite, Kirsch *et al.* reported the preparation of mushroom-like JPs consisting of a soft PnBuA phase with a cap like PMMA hard phase covering one side of the particle.

In a related work, Misra and Urban published the development of Janus-type acorn-shaped latexes with PMMA/PnBuA and PnBuA/Pentafluorostyrene (p-PFS) phases, prepared via semi-batch emulsion polymerization procedures.[32] Using the same method, Weitz *et al.* showed how micron-size polymer dumbbells acting as colloidal surfactants could be prepared according to the procedure of phase separation. These polymer dumbbells were prepared starting with cross-linked particles with an additional monomer and initiating the polymerization. The stress created inside the first particle promoted phase separation of the monomer that formed a second polymer lobe (**Figure 13**a).[33]

Finally, JPs with nanoscale anisotropy can be prepared through electrodynamic jetting of two liquid solutions containing immiscible polymers (**Figure 13**b-d).[34] For example, Rho *et al*. prepared sub-micrometer JPs via electrohydrodynamic co-jetting of two almost identical polymer solutions in water, one containing a dye and the other gold nanoparticles, followed by thermal cross-linking. Also, they synthesized JPs with two different nanocrystals (TiO_2 and Fe_3O_4) segregated in the two hemispheres. Additionally, the same group reported on the preparation of JPs with spatially controlled affinity for cells by co-jetting two different solutions of PAAm-b-PAA, and functionalizing one of them with biotine moieties.[34]

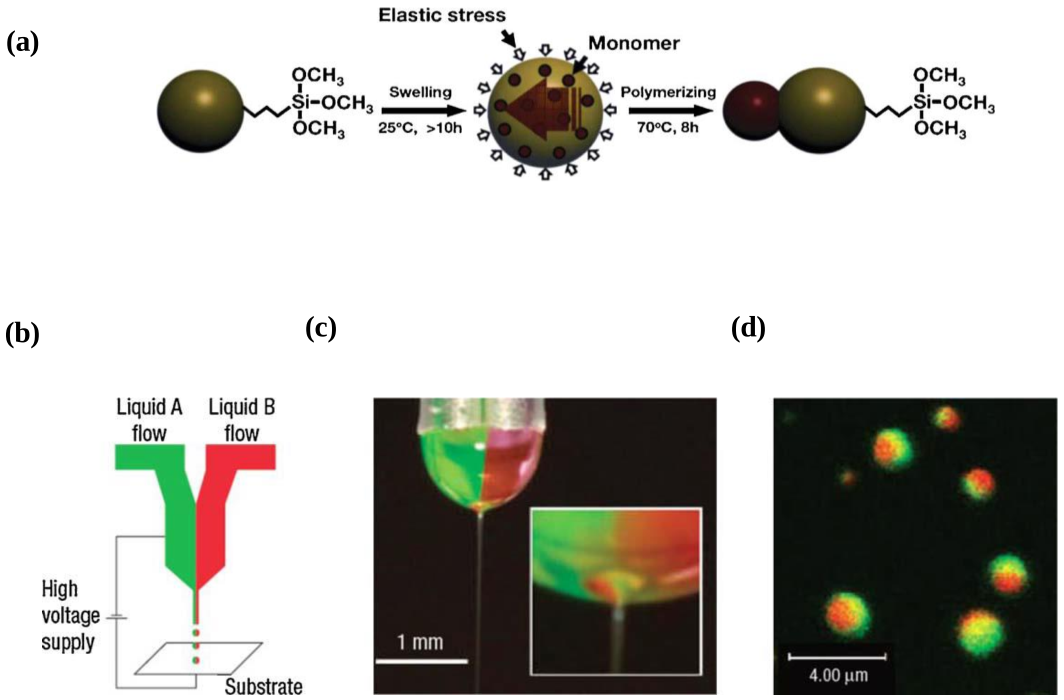

Figure 13. (a) Scheme for the synthesis of amphiphilic dimer particles by using the seeded monomer swelling and polymerization technique. (b) A schematic diagram of the experimental setup used for biphasic electrified jetting using side-by-side dual capillaries. (c) A digital image of a typical biphasic Taylor cone with jet. PEO (Mw = 600,000 g mol^{-1}) dissolved in distilled water (2% w/v) was used in both jetting fluids. Each phase was labelled by addition of 0.5%, w/v of a fluorescent dye, that is, fluoresce in isothiocyanate-conjugated dextran (green) and rhodamine-B-conjugated dextran (red). (d) Confocal micrograph of biphasic particles shown at the fluorescence emission range of FITC and rhodamine B. The overlays of these two phases reveal the biphasic character of the nanocolloids.

1.2. Properties and applications of Janus Particles

The asymmetric character of JPs allows the combination of different properties (even opposite properties, *e.g.* Hydrophilicity and hydrophobicity within a single particle, thereby confering them unique functions to be for different applications that confers them unique physical properties in different applications. Some of these applications are summarized next.

1.2.1 E-paper technology

If a particle is coated black on one side and white on the other side and an externally applied electric field can make it flip, this particle can act as a switchable optical element that can be used as a pixel in a display. Nisisako *et al.* demonstrated that microspheres died black and white with carbon black and titania pigments, respectively, can be actuated by reverting AC-electrical fields when transparent electrodes are sandwiched on top and below a monolayer of these particles (**Figure 14**a).[35] In the 70's, Sheridon *et al.* reported on a reflective light E-paper display based on bichromal (black/white) Gyricon beads. This display, which was developed at Xerox's Palo Alto Research, was considered the first electronic paper. It was composed of polyethylene Janus spheres (diameter =100 µm) that were white on one side and black on the other, carrying opposite charges. These particles were embedded in a transparent silicone sheet, dispersed in a bubble of oil, so that they could rotate freely. Remarkably, the text or pattern displayed could be altered by the presence of an electric field, with the particles facing up or down (**Figure 14**b).[36,37]

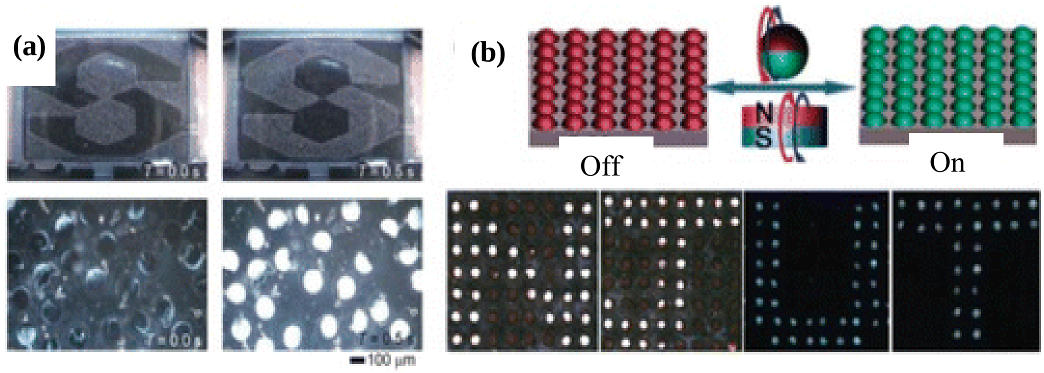

Figure 14. E-Paper panel displays based on (a) alternating current-field-based switching of Janus microspheres with black and white sides. (b) Magnetic actuation of JPs with one superparamagnetic and one fluorescent side. Each particle serves as an individual pixel in the latter example. The lower images depict optical reflection (N,J) and fluorescence (U,T) photographs.

1.2.2. Micromotors

Controlled motion of self-propelled nano-/micrometer scale objects in solution or at interfaces represents a major goal to mimic biological functions and develop vehicles for cargo transport and delivery applications in lab-on-a-chip devices or in the biomedical field. Here, the broken symmetry of JPs provides a unique approach to design self-propelling beads based on spatially confined catalysis (*e.g.* using a metal cap). For instance, the autodegradation of H_2O_2 using metal surfaces such as platinum is the most commonly catalytic reaction to induce this reaction. During this process, H_2O_2 is decomposed into two reaction products ($O_{2(g)}$ and H_2O), inducing a non-equilibrium distribution and local gradients of partly gaseous products propelling the particle forward. Various mechanisms contribute to the propulsion: increased osmotic pressure, bubble detachment due to evolution of gas, diffusophoretic driving, and interfacial tension gradients are considered the most decisive ones.[38]

In 2005, Golestanian *et al.* proposed a theoretical model in which a polystyrene sphere with a platinum cap was placed in hydrogen peroxide solution. In this phase platinum catalysed the local decomposition of hydrogen peroxide into water and oxygen.[39] The resulting asymmetric distribution of reaction products propeled the particle by self-diffusiophoresis. In 2007, the same authors confirmed experimentally the predicted mechanism. Because gas was generated during this catalytic reaction, bubble propulsion could compete with self-diffusiophoresis. Recently, Wu and co-workers compared the swimming behavior of physically deposited and chemically deposited platinum-dielectric particles. They concluded that self-diffusiophoresis usually dominated for JPs with smooth metal films that were deposited by physical methods, whereas bubble propulsion dominates for chemically deposited coatings with rough metal surfaces, whose defects provided nucleation sites for bubbles. In the bimetal nanomotor system, the dominant mechanism is believed to be an electrochemical reaction of H_2O_2 fuel solutions that generate self-electrophoresis.

These “swimming” behaviour of JPs has been used, for example, to accelerate some reactions and adsorptions in solutions. For example, Wang *et al.* reported that self-propelled activated carbon-based JPs micromotors (Pt@Ps) can display efficient locomotion in environmental matrices and offer JP effective ‘on-the-fly’ removal of a wide range of organic (nitroaromatic explosives, organophosphorous nerve agents and azo-dye compounds) and inorganic (heavy metals) pollutants (**Figure 15**).[40]

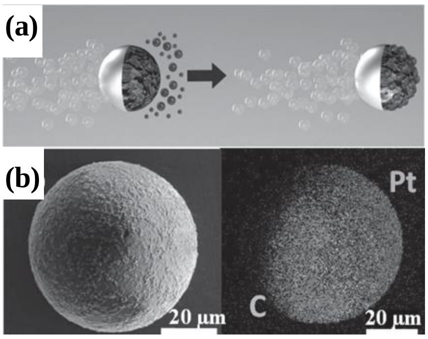

Figure 15. (a) Schematic of the activated carbon/Pt Janus micromotor and its 'on-the-fl y' decontamination use. The dark hemisphere (right) represents the spherical activated carbon, while the grey area (left) corresponds to the catalytic Pt hemisphere patch. (b) Scanning electron microscope (SEM, left) image and energy-dispersive X-ray (EDX, right) spectroscopy images illustrating the distribution of carbon (C) and (Pt) in the Janus micromotor.

1.2.3. Solid surfactant

Anticipated by de Genes, one of the advantage of JPs is that they can form monolayers at the air-liquid and liquid-liquid interfaces acting as surfactants. Thus, JPs can be employed as emulsion stabilization agents because they adsorb strongly at the liquid−liquid interface. Granick and Ohtani showed that amphiphile. JPs synthesized by the wax emulsion method (presented above) can be used to stabilize emulsions, In these JPs, the area of the hydrophobic patches could be controlled using surfactant.[41] These JPs dispersed in toluene were mixed with water. After emulsification, the emulsion was held at room temperature and immediately photographed to capture the state of the phase separation, so that the emulsion stability could be evaluated by monitoring the changes in the suspension with time. For emulsions stabilized by JPs of different geometry, no changes were observed even after 3 weeks. Particles without chemical modification could not stabilize the emulsions, which confirmed the need for Janus functionalization.

Synytska *et al.* reported inorganic silica core particles covered with two distinct polymeric shells, a hydrophilic (poly acrylic acid) and a hydrophobic (polystyrene) shall located on its opposite sides, where gold and silver nanoparticles were immobilized directly into the hydrophilic stimuli-responsive polymer shell through the Pickering emulsion method **(Figure 16**a). These JPs with immobilized metallic nanoparticles demonstrated high interfacial catalytic activity and efficient stabilization of water−oil emulsions, which could be tuned by pH. In addition, these JPs catalysed the reduction of methylene Blue, Eosin Y, and 4-nitrophenol **(Figure 16**b-d), and they could be easily recovered after reaction and reused again.[42]

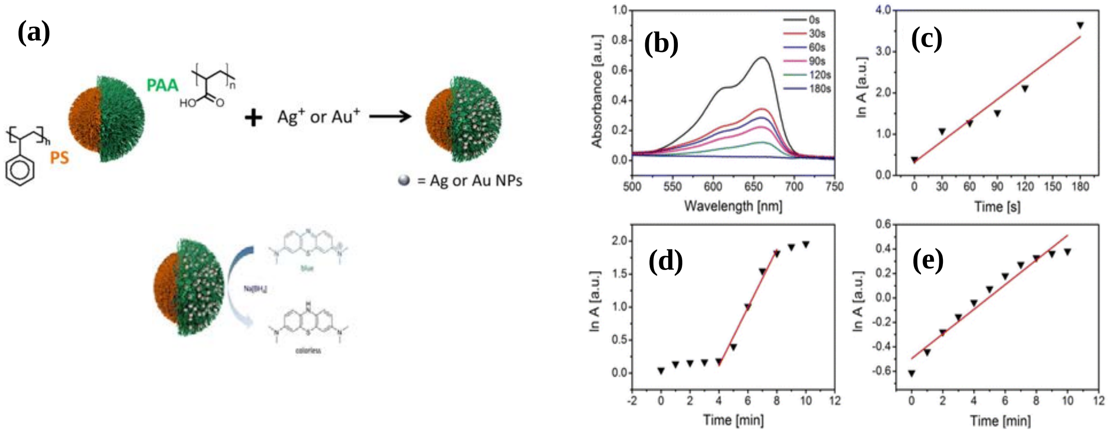

Figure 16. (a) Scheme showing the synthesis of polymer Ag or Au JPs. (b) UV–vis spectra of the catalytic Methylene Blue reduction. (c) Logarithmic plots of the decreasing absorbance over elapsed time for the catalytic reduction of Methylene Blue. (d) Eosin Y in the presence of polymer Janus Ag NPs. (e) Logarithmic plot of the decreasing absorbance over elapsed time for 4-nitrophenol reduction catalyzed by polymer Janus Au NPs.

1.2.4. Surface modifications.

JPs can also be employed to modify the properties of surfaces. For example, Synytska *et al.* reported on tailoring the wettability of substrates by immobilization of amphiphilic JPs. Therein, the JPs bound *via* one side to a surface (e.g. textiles), whereas their hydrophobic side faced the environment. Accordingly, it was found that the immobilization of JPs resulted, in the hydrophobization of hydrophilic textile surfaces, having useful applications for the design of water-repellent fabrics. The further assembly of smaller nanoscale particles onto the hydrophobic side of micrometer-sized Janus beads gave rise to hierarchically structured hemispheres, which could mimic the nano-to-micro roughness known from lotus leaves (**Figure 17**).[43]

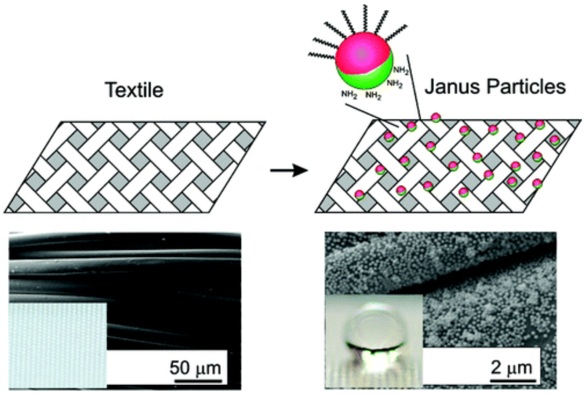

Figure 17. Representative images of morphology and wetting properties of textiles modified by chemically immobilized amphiphilic micrometer and submicrometer large JPs.

1.2.5. Life science

Considering that JPs can combine various inorganic and (bio)organic functionalities on different hemispheres, significant promise arises from using them for applications interfacing the biological world. For example, Lahann *et al*. reported a novel type of microstructured bio-hybrid material comprised of anisotropic polymer particles with spatially-controlled affinity towards human endothelial cells.[34] They used polymer-based Janus spheres, prepared *via* electrohydrodynamic co-jetting, with one side modified with biotin tags and each side additionally labeled with green and red fluorescence emitting dyes, respectively. After streptavidin modification, these beads showed selective binding to human endothelial cells that were labeled with biotinylated antibody against platelet endothelial cell-adhesion molecules (PECAM). PECAM is highly expressed on endothelial cells including the therein-studied human umbilical vein endothelial cells (HUVECs) (**Figure 18**). A control experiment to a biotinisotype antibody revealed no association between the HUVEC cells and the beads. The presence of an additional homogeneous PEG coating on the Janus beads assisted in suppressing any non-specific adhesion.[34]

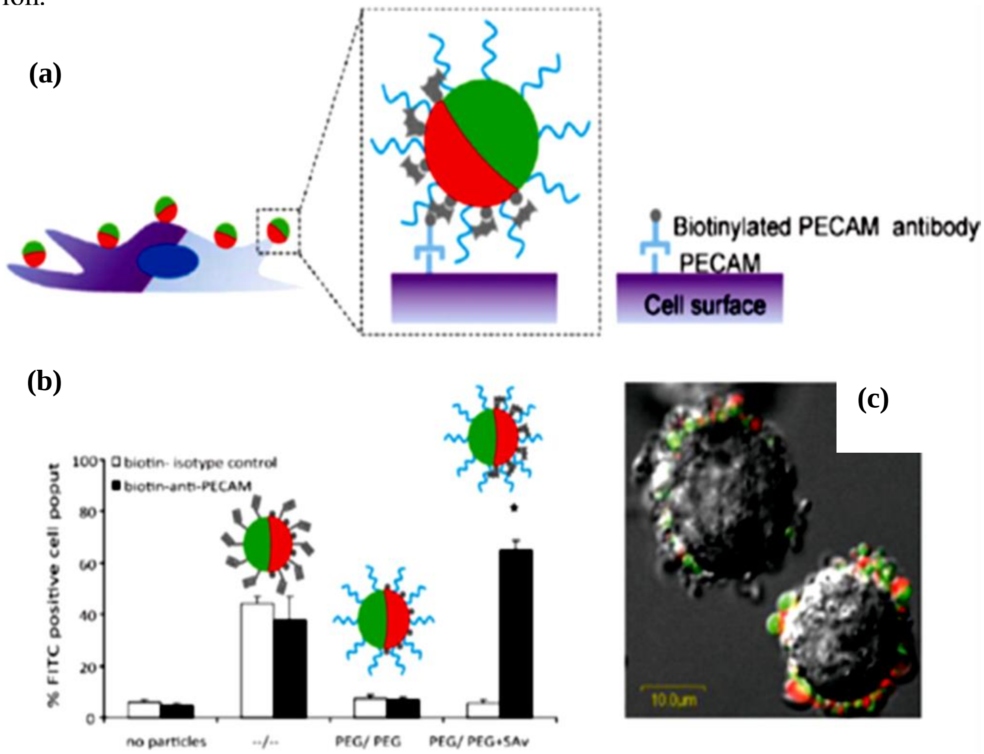

Figure 18. Anisotropic biosensing using dual functional imaging probes: (a) Scheme for the binding of bicompartmental particles to cells via streptavidin present on the particle surface of one compartment with biotinylated cell-specific antibodies (in this case PECAM). Tethered PEG chains (light blue) are homogeneously coated to prevent non-specific adsorption. (b) Quantification of the percentage of cell population with bound bicompartmental particles. From left to right: No particles, unmodified particles containing alkyne groups used during the synthesis where non-specific binding leads to cell-adhesion, fully PEG-modified particles without streptavidin showing suppressed non-specific adhesion, and fully PEG- modified particles containing SAv conjugates on one side that specifically recognize the biotinylated PECAM antibody. (c) CLSM+DIC (overlay) microscopy images depicting the degree of orientation induced by the binding of the bioprobes onto the cells.

Imaging and therapeutic properties can also be combined in a unique JPs. This approach was developed by Hu and Gao.[44] They used fluorescent JPs (diameter ca. 100−300 nm) containing a hemisphere of superparamagnetic NPs. The authors studied the performance for optical imaging as a function of orientation of the magnetic caps. When placed on the stage of an inverted microscope, in which both incident light and fluorescence travel through objectives on the bottom, fluorescence was found to be significantly reduced when the magnetic caps were oriented to the bottom/in the direction of the objective. Both exciting beam and emitted light were efficiently blocked through the inorganic layer. On the contrary, strong fluorescence could be seen once the magnetic caps were switched up and thus out of the light pathway. Further, the authors demonstrated that the magnetic particles can be quickly attached to cells. Subsequent application of a spinning magnetic field (50 rpm) for a short time (15 min) sufficed to kill the majority of the cells due to mechanical disruption of their cell walls. Modification of the beads may allow high biocompatibility, targeting of specific cells, and combined imaging and magnetolytic therapy (**Figure 19**).[44]

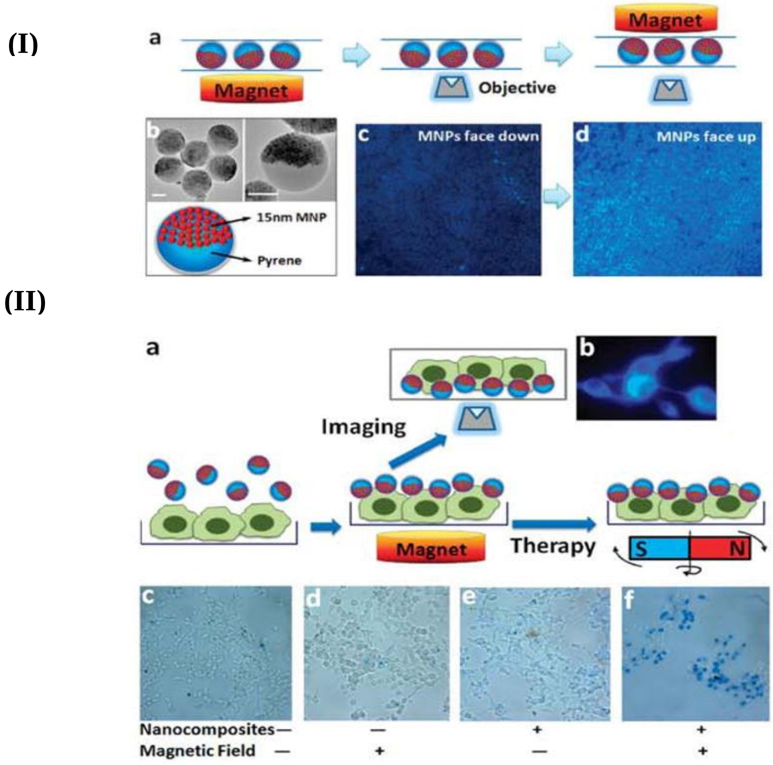

Figure 19. Combined imaging and therapeutic use of superparamagnetic JPs loaded with fluorescent dyes. (I) Orientation-dependent fluorescence of magneto-optical JPs, depicting (a) microscopy setup, (b) TEM images and schematic of the JPs (scale bar: 100 nm), and (c,d) fluorescence images of JPs of opposite orientations. (II) Simultaneous imaging and treatment of cancer cells using JPs. (a) Schematic illustration of the experimental conditions and magnetolytic therapy. The JPs are first brought to the cell surface by magnetic attraction. (b) Fluorescence imaging of cells coated with JPs. (c−f) Magnetolytic therapy on tumor cells with spinning magnetic fields. In comparison with the controls, missing either magnetic fields or JPs, the viability of cells exposed to both is significantly reduced (dead cells appear blue due to Trypan blue staining).

2. **Janus metal@MOF particles**

2.1. State of the art

The large majority of JPs described so far are composed by inorganic particles and/or polymers. Recently, researchers have tried to combine the intrinsic porosity of MOFs with other materials in JPs. However, only a few have been recently reported.[45,46]

In 2014, Bradshaw and Kuhn *et al.* reported the synthesis of metallic Janus MOF materials using a electrochemical approach (**Figure 20**a-c). They used bipolar electrochemistry (BE) to produce Janus-type MOF composites inducing the site selective ZIF-8 or HKUST-1 crystallization on a polarized metallic wire under an electric filed. In BE, a conducting object is exposed to an electric field established between two electrodes in a solution, including this induces a positive and negative polarization between the two opposite sides of the object and a redox reactions can occur.[47]

The same year, Lahann *et al.* described a new type of hierarchically functionalized colloidal composite particles, where MOF nanocrystals are spatio-selectively grown on the surface of compositionally anisotropic microparticles. The patchy seed particles were initially prepared *via* electrohydrodynamic co-jetting of two distinct polymer solutions with differently functionalized polymers, P(nBMA-co-CEMA) and P(nBMA-co-CEMA) and P(tBMA-co-CEMA) (3.5:1); this latter containing carboxylic group to direct the growth of a MOF such as HKIST-1. Then, they selectively growth HKUST-1 crystals alternatingly immersing microparticles in an ethanol solution of $Cu(OAc)_2$ and benzene-1,3,5-tricarboxylic acid. XRPD and SEM analysis confirmed that HKUST-1 crystaks were successfully grown on the particle hemisphere (**Figure 20**d).[48]

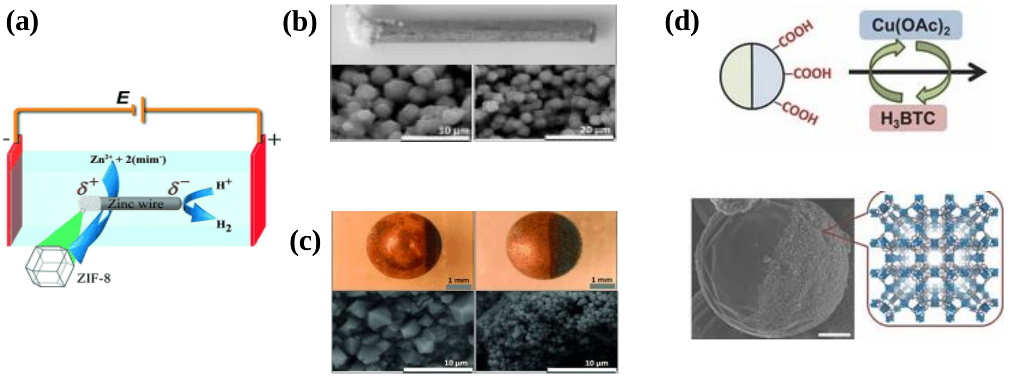

Figure 20. (a) Mechanism of the formation of ZIF-8. Crystal growth on the anodically polarized side of a zinc wire is triggered by indirect bipolar electrodeposition (IBED), (b) Optical image of the site-selective modification of a zinc wire with ZIF-8, and SEM images of ZIF-8 morphology, (c) Optical image of site-selective modification of a copper bead (3 mm diameter) with HKUST-1, and SEM images of HKUST-1 as-synthesized by IBED on one side of the copper bead, (d) Schematic representation of selective growth of HKUST-1 on the surface of compartmentalized polymer microparticles.

Thus, the attempts carried out by Bradshaw *et al.* and Lahann *et al.* confirmed the possibility to combine MOFs with other materials leading to JPs at the micrometre scale. However, to date, no suitable methods for the preparation of submicron-sized metallic Janus particles comprising single MOF particles have been described. Thus, in this chapter we will study a general strategy to synthesize porous metallic Janus MOF particles, has been developed based on direct evaporation of metals on the surface of colloidal MOF pre-immobilized onto planar surfaces.

2.2. Selection and synthesis of colloidal MOFs crystals

The selected MOFs to make the Janus metal@MOF particles were ZIF-8,[49,50,51] UiO-66,[52] and UiO-66-SH.[53] A schematic representation of each one of these MOFs is given in **Figure 21**.

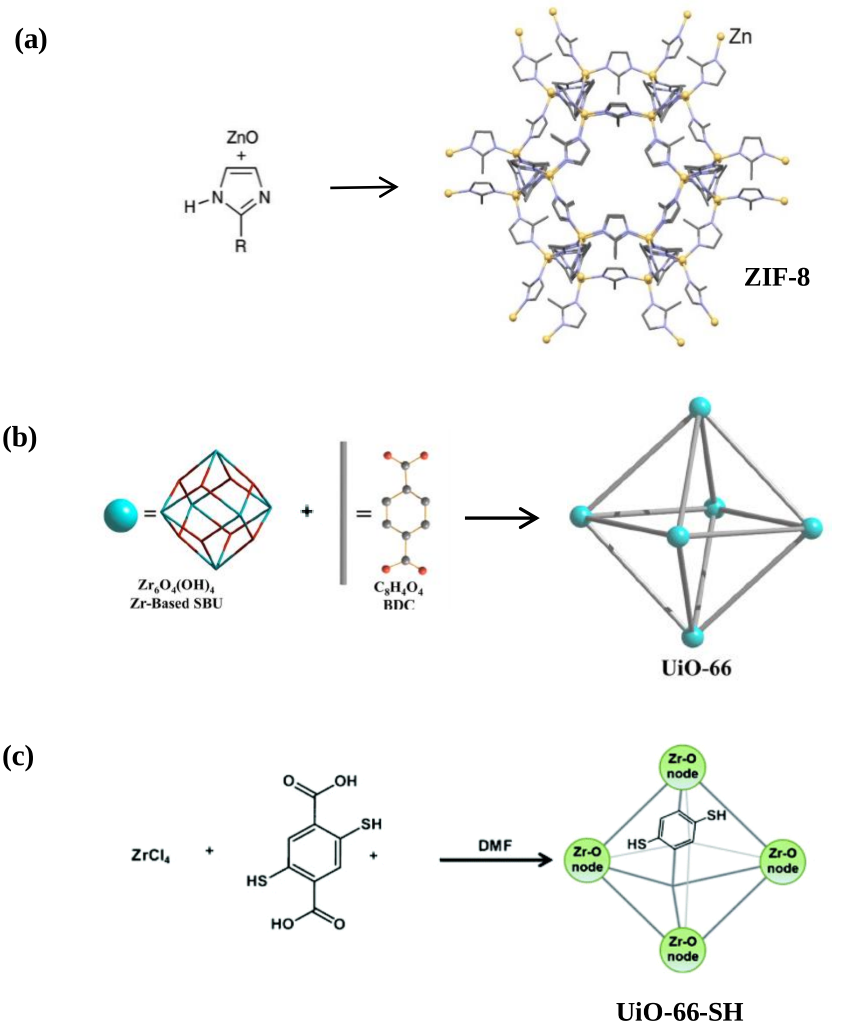

Figure 21. Schematic representation showing a) ZIF-8, b) UiO-66 and C) UiO-66-SH.

ZIF-8 **(**ZIFs family for Zeolitic Imidazole Framework) is among the most important porous MOF material known today. ZIF-8 is structurally isomorphous with zeolites as a consequence of the bridging metal-imidazole-metal angle of ~145° which is equivalent to the average Si–O–Si angle in zeolites. ZIF-8 features sodalite (SOD) topology and shows large cavities (11.6 Å) and small apertures (3.4 Å). ZIF-8 presents a high specific surface area ($S_{BET} \approx 1600$ m^2/g [49]), high thermal stability ≈ 400 ºC, and high control in size and shape that can be reached using different synthetic strategies. In the last years, ZIF-8 has been widely studied in membranes for gas separation ((H_2, CO_2, O_2, N_2 and CH_4),[54,55,56] as supports for metallic nanoparticles in catalytic processes,[57,58,59,60] and used to remove heavy metal ions, such as As (III) and As (IV),[55] Cu^{2+}, Ni^{2+}, Co^{2+}, and Cd^{2+}.[56]

UiO-66 (UiO stands for University of Oslo)[52] is formed by twelve-connected $Zr_6O_4(OH)_4(CO_2)_{12}$ clusters that are linked by linear 1,4-benzenedicarboxylic acid (bdc) linkers. The main characteristics of UiO-66 are its high specific surface area of 1376 m^2/g,[52] its high chemical and thermal stability (≈ 500 ºC),[61] for all these reasons, it shows high promise for catalysis,[62] encapsulation drugs,[63] gas adsorption (CH_4, CO, and CO_2),[64] and toxic metal removal from wastewater.

UiO-66-SH is obtained by replacing bdc by mercapto 1-4-benzenedicarboxylic (bdc-SH). The main characteristic of this MOF is the presence of mercapto moieties on the pore walls that bind selectively mercury ions, making UiO-66-SH a perfect candidate to remove Hg^{2+} from waste water.[53]

Once selected colloidal particles of each MOF were synthesized by adjusting the conditions of the previously reported methods. [49,50,51,52]

Synthesis of ZIF-8-a Particles (size = 1.3 ± 0.2 µm). A solution of 2-methylimidazole (Hmim; 810.6 mg; 9.9 mM) and 1-methylimidazole (1-Hmim; 810.6 mg (9.9 mM) in 50 mL of MeOH was poured into a solution of $Zn(NO_3)_2 \cdot 6H_2O$ (734.4 mg; 2.5 mM) in 50 mL of MeOH under magnetic stirring. Stirring was stopped just after both solutions had been mixed. The resulting mixture was kept at room temperature for 24 h. A white precipitate was collected by centrifugation (16775 x g), washed with MeOH, and dried under reduced pressure.[49] *For ZIF-8-b Particles (size = 201 ± 9 nm).* A solution of $Zn(NO_3)2 \cdot 6H_2O$ (1116 mg; 15.0 mM) in 250 mL of MeOH was added into a solution of Hmim (308 mg; 15.0 mM) in 250 mL of MeOH.[57] The mixture was heated at 50 °C for 2 h, and then cooled down to room temperature. The resulting white precipitate was collected by centrifugation (16775 x g), washed with MeOH, and dried under reduced pressure. *For Synthesis of ZIF-8-c Particles (size = 101 ± 10 nm).* The mixture was heated at 50 °C for 1 h, and then cooled down to room temperature. The resulting white precipitate was collected by centrifugation (16775 x g), washed with MeOH, and dried under reduced pressure.

Synthesis of UiO-66 Particles. A mixture of $ZrCl_4$ (34.9 mg; 15.0 mM), terephthalic acid (24.9 mg; 15.0 mM) and acetic acid (0.69 mL; 1.2 M) in 8 mL of DMF was heated at 120 ºC for 12 h. The resulting solid was collected by centrifugation (16775 x g), washed three times with DMF and MeOH, and dried under reduced pressure.[52] *For synthesis of UiO-66-SH Particles.* 2,5-dimercapto-1,4-benzenedicarboxylic acid (BDC-SH) was synthesized as previously reported.[65] Then, a mixture of $ZrCl_4$ (18.5 mg; 19.3 mM), BDC-SH (9.3 mg; 10.0 mM) and acetic acid (1.3 mL; 2.4 M) in 8 mL of DMF was heated at 120 °C for 12 h.[52] The resulting solid was collected by centrifugation (16775 x g), washed three times with DMF and MeOH, and dried under reduced pressure.

The samples were characterized by scanning electron microscopy (FESEM), X-ray powder diffraction (XRPD) and N_2 sorption measurement (S_{BET}).

Characterization by FESEM

Field-emission scanning electron microscopy (FESEM) images were collected on a scanning electron microscope (FEI Magellan 400L XHR) at acceleration voltage of 2.0 kV, the samples were prepared using aluminium as support.

The size of crystals was calculated from FESEM images by averaging the diameter of at least 200 particles from images of different areas of the same samples.

Characterization by XRPD

X-ray powder diffraction (XRPD) measurements were done on an X'Pert PRO MPDP analytical diffractometer, using a λCu = 1.5406 Å (PANalytical), and λCo = 1.79. Sample preparation was carried out by the dispersion of powder on silicon substrates, then the measurement conditions were; start and end angle 2θ° (5°-40°), step size; 0.06648, time per step; 250.190, scan speed (°/s): 0. 03393, number steps; 973, total time; 33 min.

Characterization by N_2 adsorption

N_2 sorption measurement was used to evaluate the adsorption capacity of MOFs and their composites. Volumetric N_2 sorption isotherms were collected at 77 K using a Quantachrome instrument; the sample weight used for measurement was ≈ 40 mg.

An adsorption isotherm is obtained by measuring the amount of gas adsorbed across a wide range of relative pressures (P/P_0) at a constant temperature (typically liquid N_2, 77K). Conversely desorption isotherms are achieved by measuring gas removed as pressure is reduced.

The measurement consists in two steps; I) sample activation, were the sample is under the degas conditions in order to eliminate, volatile organic molecules and water molecules. In this step there is a heating ramp which gradually increases the temperature. II) After sample activation is carried out the N_2 adsorption under relative pressures.

The selected MOFs were ZIF-8 (particles size = 101 ± 10 nm, 201 ± 9 nm, and 1.3 ± 0.2 μm); UiO-66 (crystal size = 190 ± 22 nm) and UiO-66-SH (crystal size = 208 ± 54 nm). The quality of each synthesized MOF was evaluated by determining their porosity by measure of N_2 adsorption. The obtained values for ZIF-8 were (S_{BET} = 1272 $m^2 \cdot g^{-1}$, 1123 $m^2 \cdot g^{-1}$ and 1272 $m^2 \cdot g^{-1}$, for ZIF-8 particles size = 101 ± 10 nm, 201 ± 9 nm, and 1.3 ± 0.2 μm respectively; for UiO-66 was S_{BET}= 1332 $m^2 \cdot g^{-1}$ and for UiO-66-SH was S_{BET}= 306 $m^2 \cdot g^{-1}$ (**Figure 22**). Finally, the experimental XRPD pattern showed perfect match with the pattern simulated from the atomic positions extracted from the crystallographic file of the reported structure for ZIF-8, UiO-66 and UiO-66-SH (**Figure 23**).

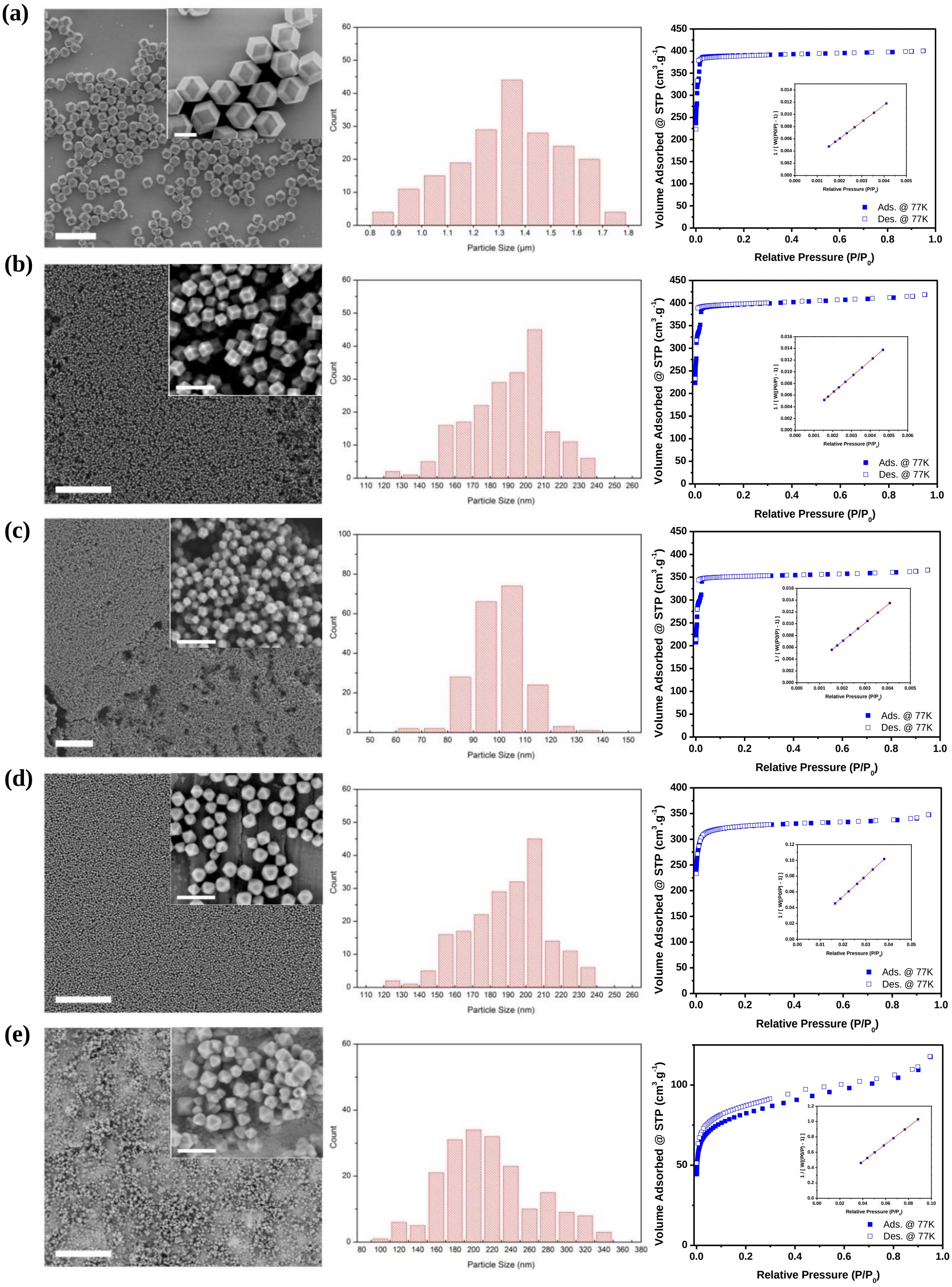

Figure 22. Representative FE-SEM images of the synthesized colloidal MOFs, the corresponding plot of the statistical analysis of their crystal size and N_2 adsorptions S_{BET} values. (a) ZIF-8 (size = 1.3 ± 0.2 µm; S_{BET} = 1271.611 m^2/g), (b) ZIF-8 (size = 201 ± 9 nm; S_{BET} =1122.986 m^2/g), (c) ZIF-8 (size = 101 ± 10 nm; S_{BET} =1271.824 m^2/g), (d) UiO-66 (size = 190 ± 22 nm; S_{BET} =1332 m^2/g), (e) UiO-66-SH (size = 208 ± 54 nm; S_{BET} =306 m^2/g). Scale bars for a (10 µm, 3 µm), b, c, d and e (10 µm and 500 nm).

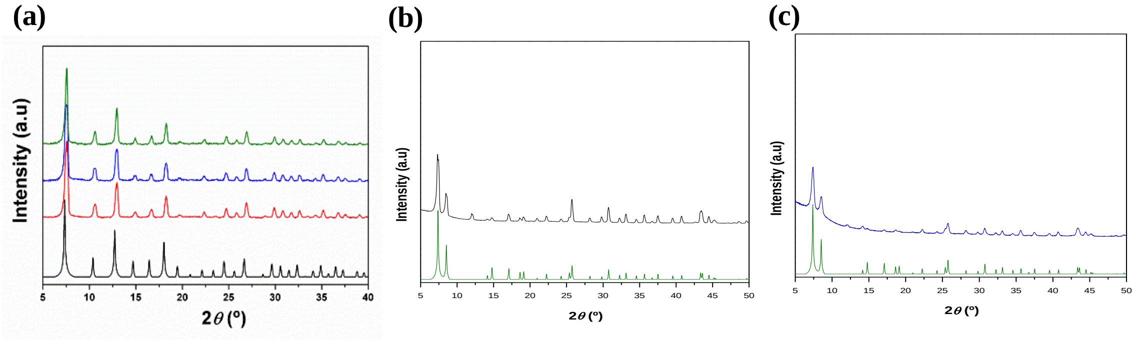

Figure 23. (a) XRPD patterns of the ZIF-8 (size = 1.3 ± 0.2 µm, green), ZIF-8 (size = 201 ± 9 nm, blue), ZIF-8 (size = 101 ± 10 nm, red), compared with the simulated XRD pattern of ZIF-8 (black). (b) XRPD patterns of the UiO-66 (size = 190 ± 22 nm, black), and (c) XRPD pattern of the UiO-66-SH (size = 208 ± 54 nm, blue) compared with the simulated XRD pattern of UiO-66 (green).

2.3. Preparation of Janus particles

In a typical experiment, each synthesized colloidal MOF was deposited onto Au surfaces that had been pre-functionalized with 4-mercaptobenzoic acid and treated with NaOH to deprotonate the carboxylic groups. This process started with the formation of colloidal dispersions of the different MOF particles. These colloids were prepared by sonicating the synthesized MOF particles (60 mg) in DMF (100 mL) for 15 min. Note that, in the case of UiO-66,[52] these particles (122 mg) were first exposed to polyvinylpyrrolidone (PVP, Mw = 40000, 230 mg) in H_2O (15 mL) under stirring overnight, collected by centrifugation (16775 x g), washed four times with H_2O, once with MeOH, and finally, dried under reduced pressure. In parallel, polycrystalline Au films were prepared by E-beam evaporation (ATC-Orion-8E UHV) of 5 nm of Ti on SiOx surfaces (4 cm^2) at a rate of 1 Å/s followed by 40 nm of Au at a rate of 3 Å/s, and a base pressure better than $1x10^{-6}$ Torr. Then, a monolayer of 4-mercaptobenzoic acid (MBA) was fabricated on top of these substrates by immersing them in a 0.1 mM ethanol solution overnight followed by copious rinsing with ethanol. Deprotonation of MBA was achieved by immersing the substrates in an aqueous solution of NaOH (0.1 % w/w) for 20 min, washed several times with H_2O and air-dried. Finally, to deposit these MOF particles, a colloidal MOF solution in DMF (0.15 mL) was spread onto the surfaces, which were then heated at 60 °C until the DMF had evaporated. Here, we made a strategic decision to carefully cover the surface with a true monolayer (even though some areas remained uncovered) rather than to fully cover the surface and risk forming MOF aggregates or multilayers, as any MOF particles underneath the resultant top layer would not be covered in the subsequent next stage.

In the next step, the surface-deposited MOF particles were coated with a metal (M = Au, Co or Pt; metal film thickness = 5 nm to 50 nm) using an E-beam evaporator. In this process, polycrystalline Au, Co and Pt films were prepared on the MOF particles by E-beam evaporation (ATC-Orion-8E UHV) of these metals at a rate of 1 Å/s (for thicknesses of 5 nm, 10 nm and 20 nm) or 3 Å/s (for thicknesses of 30 nm or 50 nm) and a base pressure greater than 1x10^{-6} Torr (**Figure 24**).

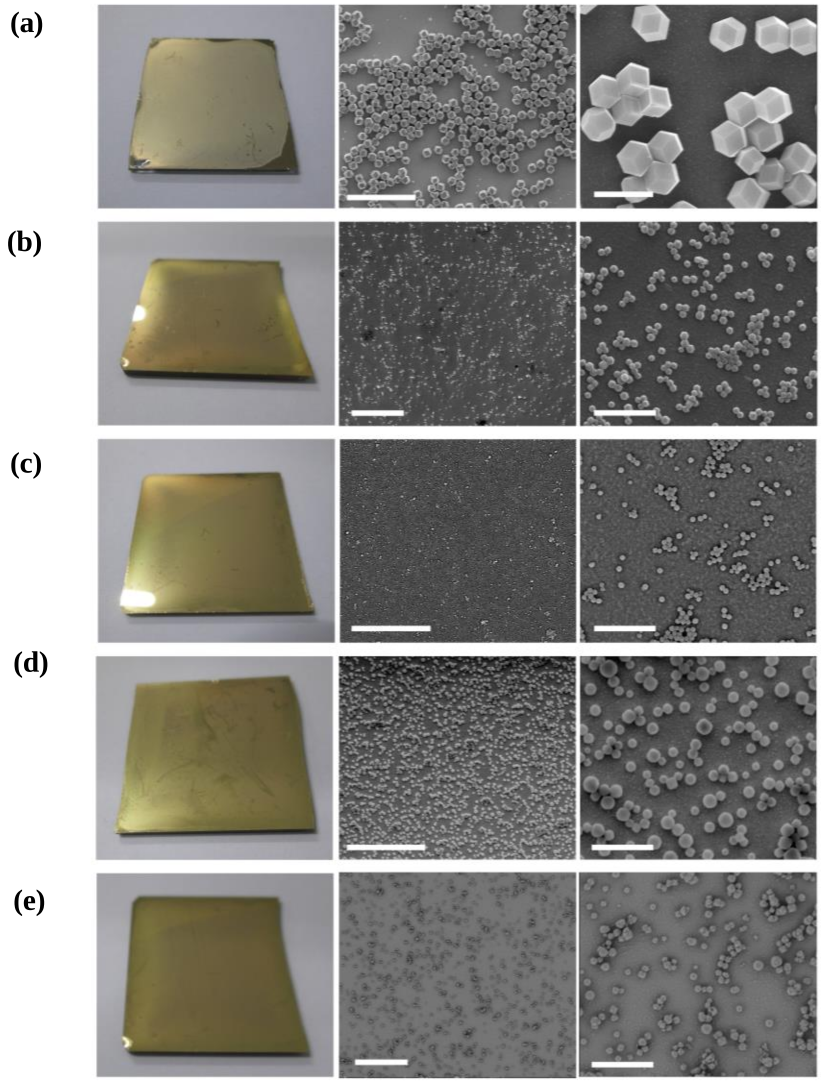

Figure 24. Representative FE-SEM images of the immobilized MOF´s on the glass Ti/Au-thiol substrates (≈ 2 cm * 2 cm), (a) ZIF-8 (size =1.3 µm ± 0.2 µm), (b) ZIF-8 (size = 201 ± 9 nm),(c) ZIF-8 (size = 101 ± 10 nm), (d) UiO-66 (size = 190 ± 22 nm), (e) UiO-66-SH (size = 208 ± 54 nm). Scale bars: 20 µm and 3 µm.

Finally, the resultant Janus M@MOF particles were detached by ultrasonication of the surfaces for 30 s in MeOH. In this final step, the synthesized Janus M@MOF particles were detached from the surfaces by ultrasonication (37 KHz, Elma S 30 H Elmasonic) of the surfaces in MeOH for 30 s.

Detached diverse Janus Au@MOF particles that varied with MOF (ZIF-8 and UiO-66), particle size (particle sizes = 101 ± 10 nm, 201 ± 9 nm, and 1.3 ± 0.2 µm, for ZIF-8 and 190 ± 22 nm for UiO-66) and Au film thickness (5 nm, 10 nm, 20 nm, 30 nm or 50 nm) were created. The Scanning Electron Microscopy (SEM) images of all synthesized MOF based JPs revealed their asymmetry by the partial coverage of the external surface of each MOF crystal with an Au thin film (**Figure 25**).

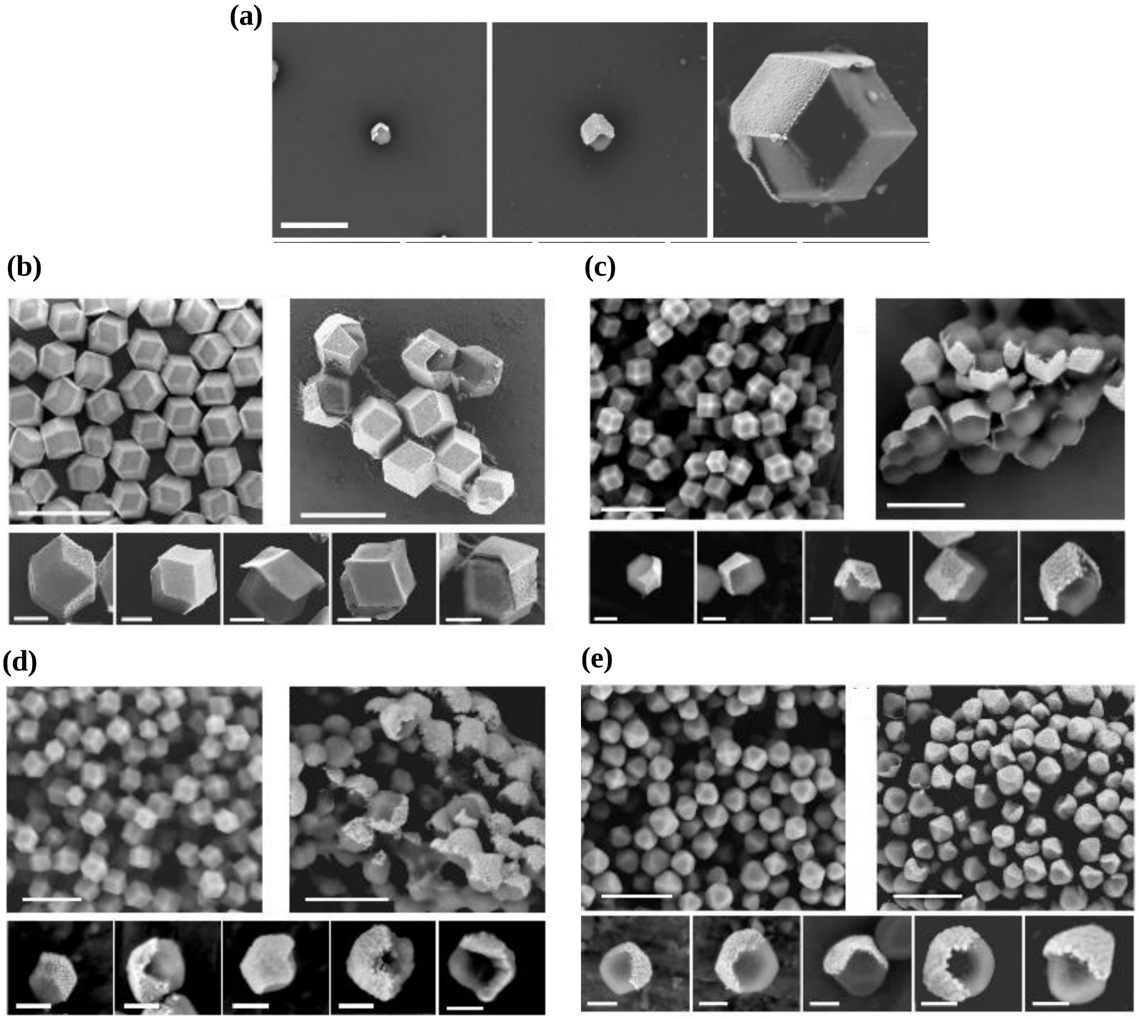

Figure 25. (a) FESEM images of individual Au@ZIF-8 particles (Au thickness = 50 nm), showing different ZIF-8 sizes (from left to right: 101 ± 10 nm, 201 ± 9 nm and 1.3 µm ± 0.2 µm). (b,c,d) Representative FESEM images showing general views of ZIF-8 particles before and after Au thin film evaporation and the different Au thicknesses (from left to right: 5 nm, 10 nm, 20 nm, 30 nm and 50 nm). (e) FESEM images of general views of UiO-66 particles (size = 190 ± 22 nm) before and after Au thin film evaporation, and individual Au@UiO-66 particles, showing different Au thicknesses (from left to right: 5 nm, 10 nm, 20 nm, 30 nm and 50 nm). Scale bars (a): 500 nm, (b): 3 µm, 2 µm, and 500 nm. (c): 500 nm, 300 nm, and 100 nm, (d): 500 nm, 400 nm, and 100 nm, (e): 500 nm and 100 nm.

The asymmetric structure of these particles was further confirmed by elemental mapping using energy dispersive X-ray spectrometry (EDX) of single particles. High angle annular dark field (HAADF) scanning transmission electron microscope (STEM)-(HAADF-STEM) images and EDX composition profile were collected by a Transmission Electron Microscopy (TEM) (FEI Tecnai G2 F20) at 200 KV. Which revealed a uniform distribution of Au atoms in approximately half of the particle surface (**Figure 26**a-c). Additionally, the increase in thickness was further corroborated by EDX analyses, which indicated that the Au:Zn or Au:Zr ratio consistently increased with the increasing Au film thickness (**Figure 26**d-g).

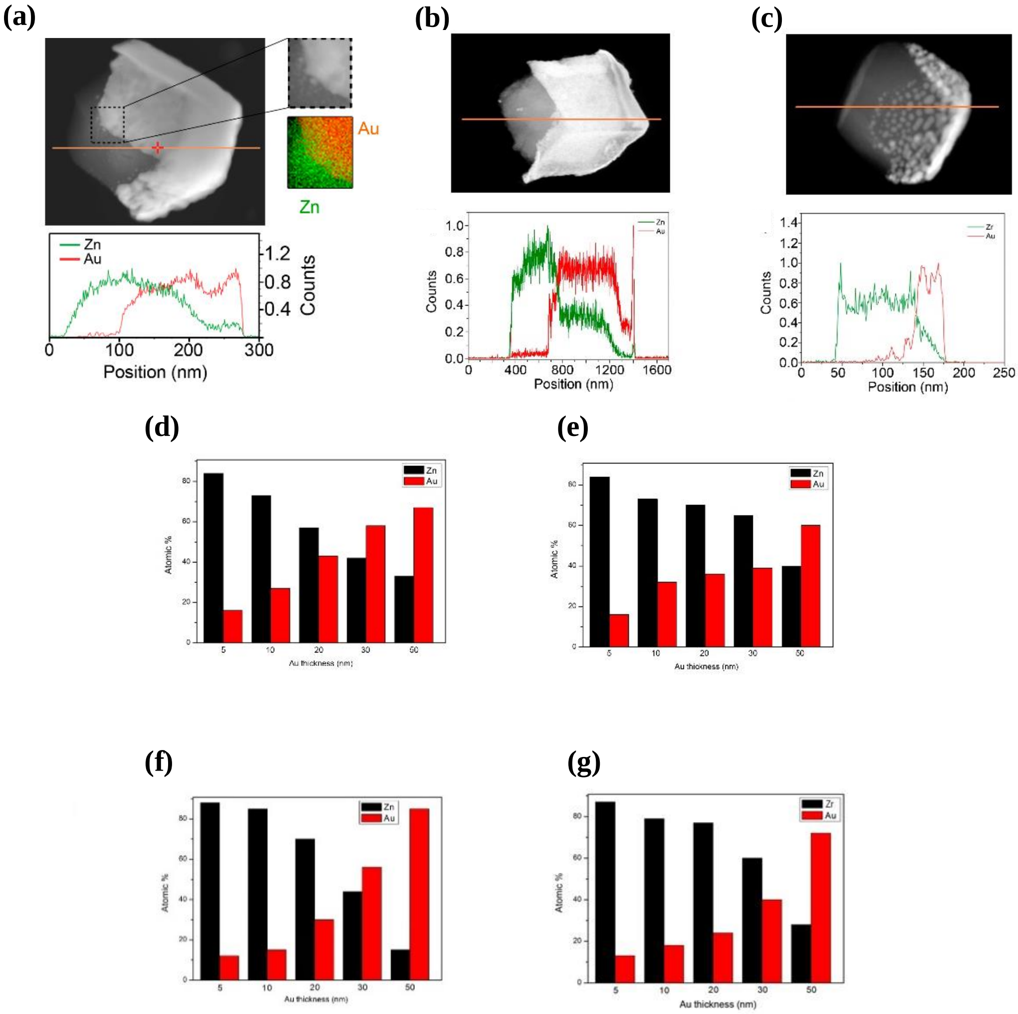

Figure 26. (a) EDX mapping of a single Au@ZIF-8 particle (size = 201 µm ± 9 nm), showing the distribution of Zn (green) and Au (red). Representative STEM-HAADF images and EDX composition analysis profile at 200 kV. (b) EDX mapping of a Janus Au@ZIF-8 (size =1.3 µm ± 0.2 µm), with 50 nm of Au thickness. (c) EDX mapping of a Janus Au@UiO- particle (size = 190 ± 22 nm), with 50 nm of Au thickness.(d-g) Plots showing the average (n = 5) of the atomic percentage (measured by EDX) between Zn and Au in the Janus Au@ZIF-8 particles of different Au film thicknesses (5 nm, 10 nm, 20 nm, 30 nm and 50 nm) of individual Au@ZIF-8 particles size (d); (1.3 µm ± 0.2 µm), (e); (size = 201 µm ± 9 nm), and (f); (size = 101 ± 10 nm), and (g) Au@UiO-66 particles (size = 190 ± 22 nm), showing different Au thicknesses (5 nm, 10 nm, 20 nm, 30 nm and 50 nm).

One might expect that the many synthetic steps required for the JPs would affect the initial crystalline integrity and adsorption capabilities of the MOFs; however, we did not observe any loss in these properties. Indeed, for all JPs, the simulated (derived from the single crystal structure) and experimental X-ray powder diffraction (XRPD) patterns were consistent, confirming that the ZIF-8 or UiO-66 in the JPs were structurally identical to the corresponding starting MOF particles. As expected, characteristic peaks for crystalline Au were also observed (**Figure 27**a-d).

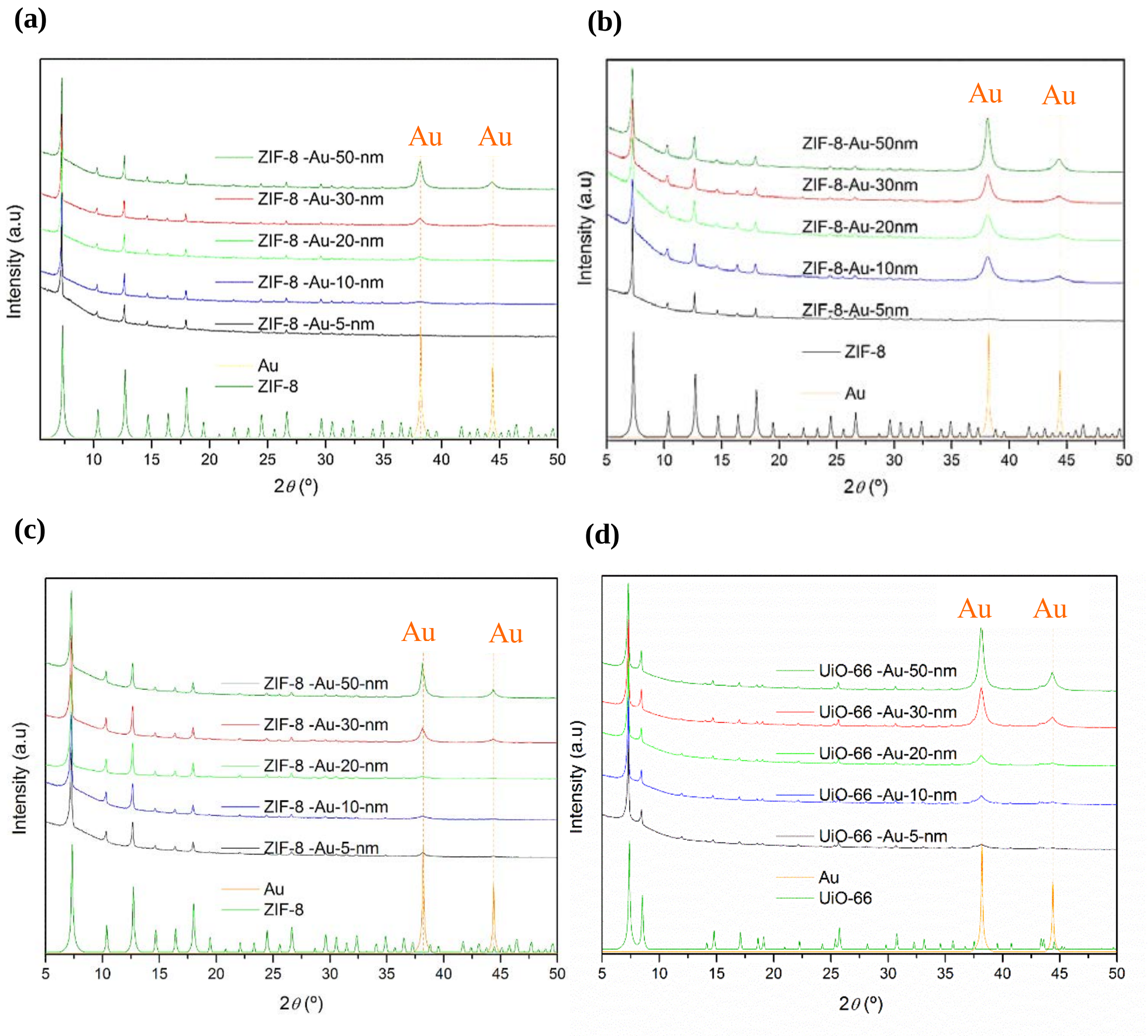

Figure 27. XRPD diffractograms of (a) Janus Au@ZIF-8 (size = 1.3 ± 0.2 μm), (b) Janus Au@ZIF-8 (size = 201 ± 9 nm), (c) Janus Au@ZIF-8 (size = 101 ± 10 nm), and (d) Janus Au@UiO-66 (size = 190 ± 22 nm) particles fabricated with different Au film thicknesses (5 nm, 10 nm, 20 nm, 30 nm, and 50 nm), and compared to the simulated powder pattern for ZIF-8, UiO-66 and Au.

Additionally, N_2 sorption measurements taken at 77 K up to 1 bar of Au@ZIF-8 (ZIF-8 size = 201 ± 9 nm; Au film thickness = 50 nm) and Au@UiO-66 (Au film thickness = 5 nm) particles proved that the sorption capacities of these particles were equivalent to that of the initial MOF particles (**Figure 28**). Thus, the S_{BET} values were determined to be 456 $m^2 \cdot g^{-1}$ for Au@ZIF-8 and 560 $m^2 \cdot g^{-1}$ for Au@UiO-66. Given that the Au thin film is non-porous to N_2, we attributed the sorption exclusively to ZIF-8 or UiO-66. Therefore, these S_{BET} values could be expressed in m^2 per gram of ZIF-8 ($S_{BET} = 1037\ m^2 \cdot g^{-1}$) or UiO-66 ($S_{BET} = 982\ m^2 \cdot g^{-1}$), once we had calculated the amount of Au present in each sample (56% w/w for Au@ZIF-8; 43% w/w for Au@UiO-66). The latter step was completed by selectively dissolving the MOF component using an aqueous HCl solution (pH < 1) for ZIF-8 and an aqueous H_2SO_4 solution (pH < 1) for UiO-66. From the calculated S_{BET} values, we found that the sorption performance of both MOFs in the JPs remains unaltered.

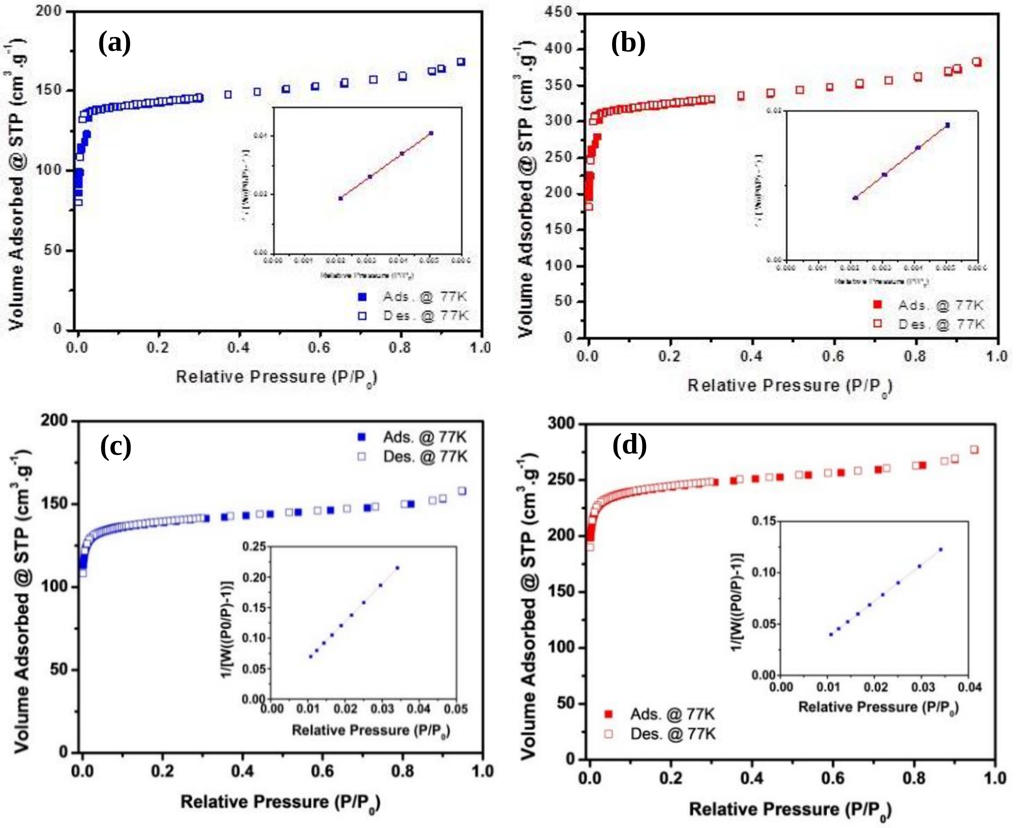

Figure 28. N_2 adsorption isotherms at 77 K and BET linear fit for Janus Au@ZIF-8 (size = 201 ± 9 nm); (Au film thickness = 50 nm) particles as expressed in m^2 per grams (a) Au@ZIF-8 and (b) ZIF-8 once calculated the amount of Au present in the samples (56 % w/w) by selectively dissolving the ZIF-8 component using an aqueous HCl solution (pH < 1). (c) N_2 adsorption isotherms at 77 K and BET linear fit of Au@UiO-66 (Au film thickness = 5 nm) particles expressed in m^2 per grams, and (d) UiO-66, once the amount of Au present in the sample (43% w/w) had been calculated upon selectively dissolving the UiO-66 component using an aqueous H_2SO_4 solution (pH < 1).

2.4. Introducing functionalities to the Janus metal@MOF particles

2.4.1. Anisotropic attachment of fluorescent dye in Janus metal@MOF particles

Once the formation of metallic Janus @MOF particles was confirmed, the possibility to take advantage of their asymmetric functionalization was explored as a first proof-of-concept of the properties that metallic Janus MOF particles can incorporate, we explored their asymmetric functionalization. To this end, we selectively attached the green fluorophore fluorescein isothiocyanate polyethylene glycol thiol (FITC-PEG-SH) onto the Au thin film. The asymmetric functionalization was performed by incubating Au@ZIF-8 particles in an aqueous solution of FITC-PEG-SH at 4 °C for 24 h. The resulting FITC-PEG-S-Au@ZIF-8 particles were then collected by centrifugation, cleaned twice with methanol, and imaged using confocal laser scanning microscopy. Confocal fluorescence images were collected in a Confocal microscope (Olympus Fluoview 1000), in mode hybrid detector, stage; x and z, with two channels; green (excitation; 488 λ, emission; 500-550 λ) and blue (excitation; 405 λ, emission; 420-490 λ). (**Figure 29**). The results clearly show two different fluorescent regions corresponding to ZIF-8 (blue)[66] and to FITC-PEG-SH (green) that are selectively attached onto the Au surfaces. Our successful demonstration of asymmetric functionalization of metallic Janus MOF particles suggests that, in the future, such particles can be vectorized for biomedical and sensing applications. Furthermore, our approach could be advantageous modulating certain properties (e.g. hydrophobicity, hydrophilicity) of the base MOF without altering its porosity.

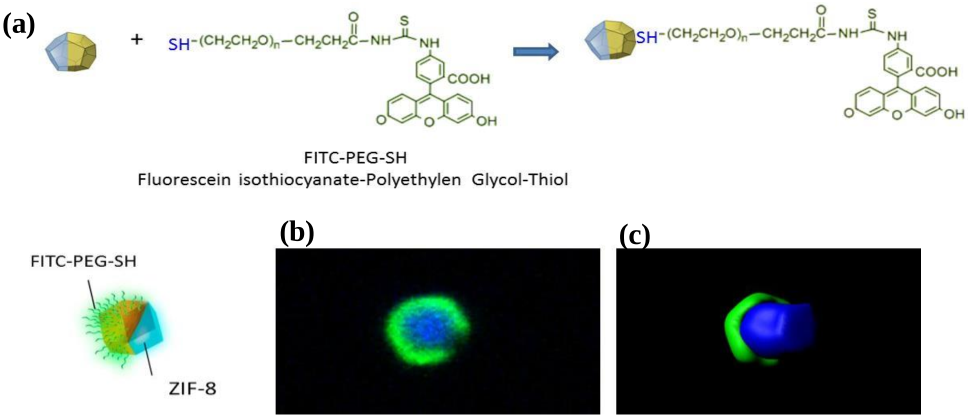

Figure 29. (a) Scheme of the Au functionalization with FITC-PEG-SH on the Janus Au@ZIF-8 particles. (b) Representative confocal image (with two channels: ZIF-8, blue (λ excitation = 405 nm, λ emission = 420 nm to 490 nm); FITC-PEG-SH, green (λ excitation = 488 nm, λ emission = 500 nm to 550 nm). (c) Corresponding 3D image showing the asymmetric functionalization of a single Janus FITC-PEG-S-Au@ZIF-8 (size =1.3 µm ± 0.2 µm) particle. Image was treated in Imaris 3D software, version 6.1.0.

2.4.2. Magnetic functionality to Janus metal@MOF particles

We next sought to create magnetically guidable porous particles. To this end, we reproduced the synthesis of metallic MOF JPs, except that Au was replaced with Co in order to confer the particles with magnetism. **Figure 30(**a-d**)** show the resultant Janus Co@ZIF-8, Co@UiO-66 and Co@UiO-66-SH particles (size = ca. 200 nm; Co film thickness = 20 nm). In all cases, EDX and XRPD analyses confirmed the desired asymmetric structure, the presence of crystalline Co, and that the crystalline integrity of all three MOFs had been fully conserved (**Figure 30**e-g).

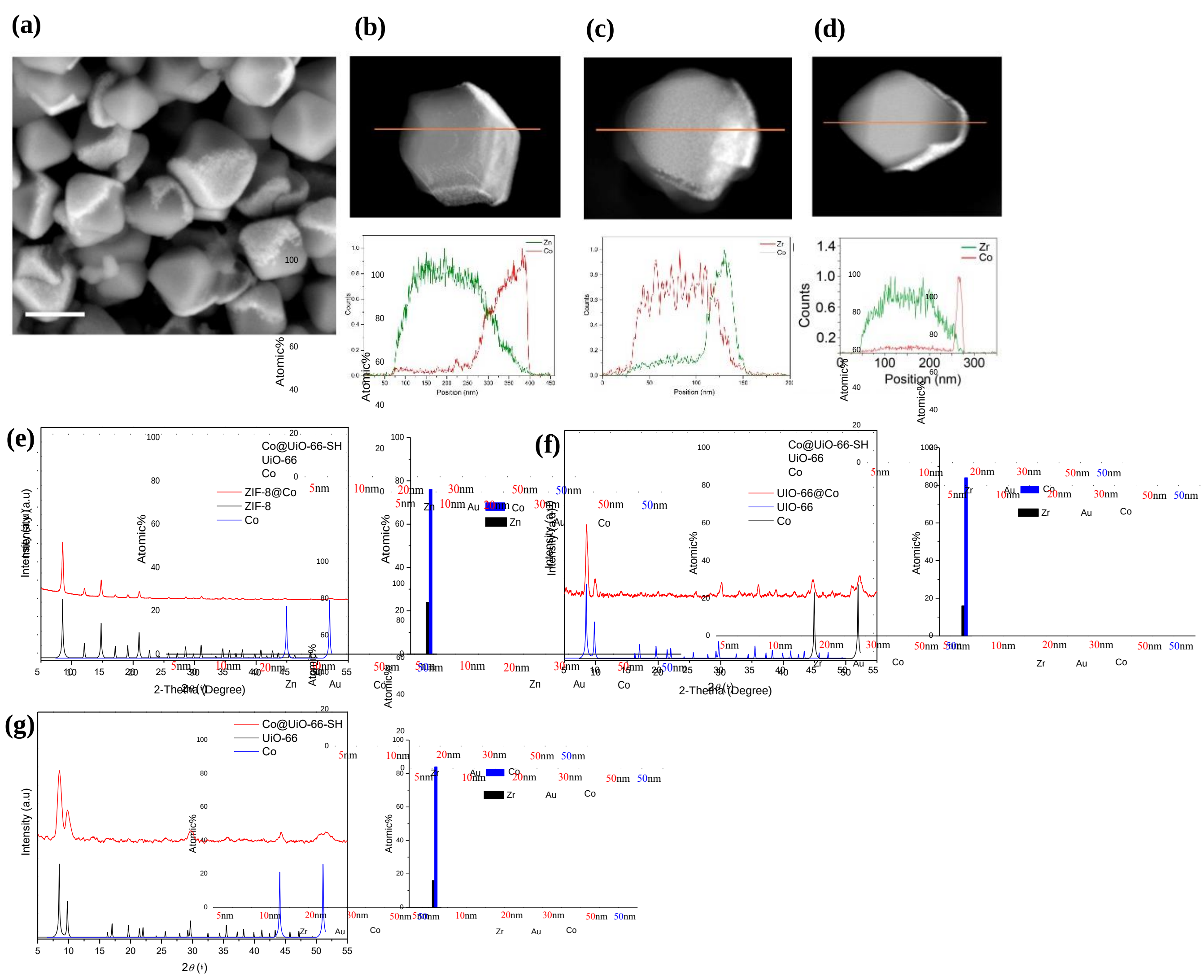

Figure 30. (a) Representative FESEM images of Co@UiO-66-SH (Co film thickness = 20 nm). (b-d) Representative STEM-HAADF images and EDX composition analysis profile at 200 kV of (b) Janus Co@ZIF-8 (size = 201 ± 9 nm) with 50 nm of Co thickness, (c) Janus Co@UiO-66 (size = 190 ± 22 nm) with 50 nm of Co thickness, and (d) Janus Co@UiO-66-SH (size = 208 ± 54 nm). (e-g) XRPD diffractograms, and plot showing the average (n = 5) of the atomic percentage (measured by EDX) between MOF and Co film thicknesses of (e) Janus Co@ZIF-8, (f) Co@UiO-66 nm, and (g) Co@UiO-66-SH.

More importantly, all the JPs incorporated the magnetic properties of the Co component, as demonstrated by the fact that they could be easily guided by a magnet (**Figure 31**a). Magnetic measurements by Superconducting Quantum Interference Device (SQUID), and they were recorded on a Quantum design MPMS XL-7T (SQUID 7T) instrument at 300 K. Also confirmed the magnetism of the particles, which exhibited a characteristic hysteresis loop with coercive field values of 181 Oe (Co@ZIF-8), 350 Oe (Co@UiO-66) and 23 Oe (Co@UiO-66-SH) at room temperature (**Figure 31**b-d).

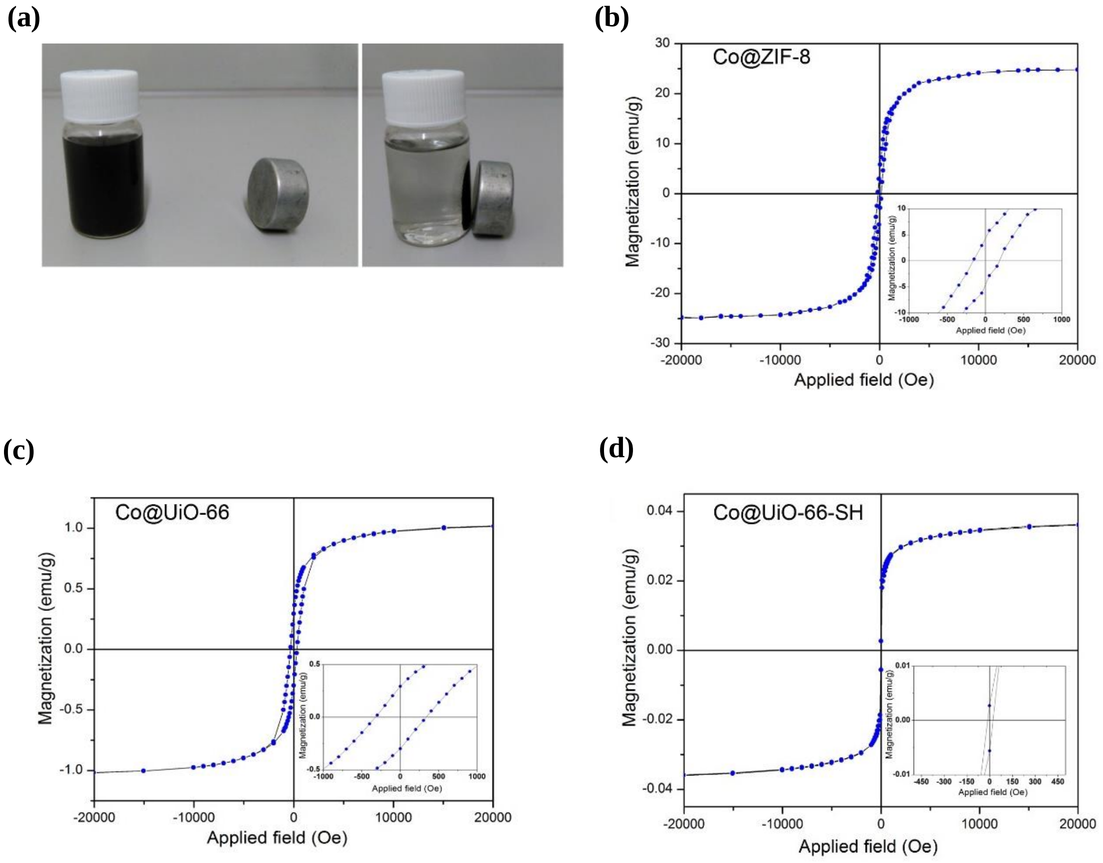

Figure 31. (a) Photographs showing the magnetic attraction of Co@UiO-66-SH particles dispersed in an aqueous solution of mercury before (left) and during (right) exposure to a magnet. (b-d) Magnetic hysteresis loop measured by SQUID at 300 k of (b) Janus Co@ZIF-8 (size = 201 ± 9 nm), (c) Co@UiO-66 (size = 190 ± 22), and (d) Co@UiO-66-SH (size = 208 ± 54 nm) particles.

To demonstrate that these JPs could be employed to adsorb target substances and subsequently recovered magnetically, we tested the performance of Co@UiO-66-SH particles in magnetic solid-phase removal of mercury. To this end, Co@UiO-66-SH particles (2 mg) were dispersed in a solution of 10 ppm Hg^{2+} in water (4 mL) at room temperature. After 30 min of incubation, the mercury content adsorbed by the JPs was determined by ICP-MS. The extraction was observed to be highly efficient: the particles had sequestered 99% of the mercury from the solution, and could then be easily removed using a small magnet (**Figure 32**).

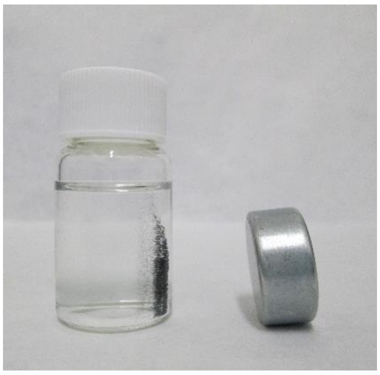

Time (h)	Concentration of Hg^{2+} (ppm)
0.5	0.086
1	0.090
2	0.108
4	0.129
8	0.109

Figure 32. Photograph showing the magnetic attraction of Co@UiO-66-SH particles dispersed in an aqueous solution of mercury when they were exposure to a magnet, and the resulting ICP values of Hg^{2+} concentrations after each period.

In addition, we tested our method for the fabrication of polymetallic Janus MOF particles, which we carried out by sequentially evaporating different metals on the surface of the colloidal MOF crystals.

Thus, UiO-66 crystals were first coated with Co (thickness = 20 nm) and then, with Au (thickness = 5 nm). The resulting particles were confirmed by EDX elemental mapping to be polymetallic Au@Co@UiO-66 particles, as also demonstrated by XRPD and magnetic measurements (**Figure 33**a-c**)**. Finally, the polymetallic Janus Au@Co@UiO-66 were functionalized with FITC-PEG-SH, resulting in the Janus FITC-PEG-SH-Au@Co@UiO-66 particles, and demonstrating that the particles can be attracted by a magnet (**Figure 33**d,e).

Therefore, these latter Janus MOF particles were designed to combine the porosity properties of UiO-66, the magnetic properties of Co and the easy chemical functionalization of the external Au layer.

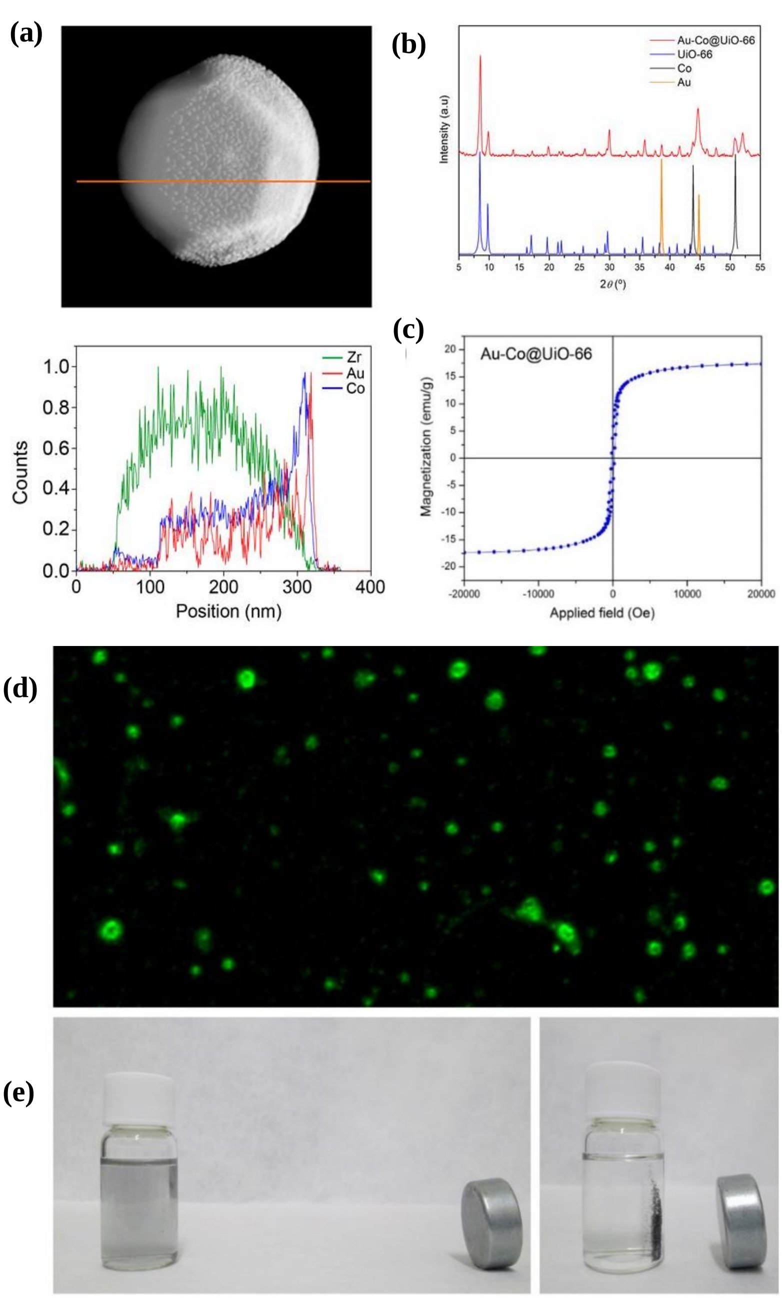

Figure 33. (a) EDX elemental mapping of Janus AuCo@UiO-66 particle (size = 190 ± 22 nm). (b) XRPD diffractogram of the Janus AuCo@UiO-66 (Co = 20nm and Au =5 nm of thickness). (c) Magnetic hysteresis loop measured by SQUID at 300 k of Janus AuCo@UiO-66particles. (d) Confocal image and (e) photographs showing the magnetic attraction of Janus AuCo@UiO-66 particles.

2.4.3. Motorized functionality to Janus Pt@ZIF-8 particles

As mentioned in the first section of this Thesis, Pt promotes the catalytic process of decomposition of H_2O_2. Thus, by incorporating Pt to a Janus particle, it becomes a chemically powered motor exhibiting autonomous propulsion. In this sense, once we had demonstrated that MOF particles could be asymmetrically metallized, we then sought to explore the development of motorized MOFs powered by electrochemistry, using Pt as the metal. To this end, we fabricated Janus Pt@ZIF-8 particles of a size of = 1.3 ± 0.2 µm, and 8 µm (for better visualization using optical microscopy) and with a Pt film thickness of 60 nm. The EDX elemental mapping of one of these particles revealed the presence of Pt (red) and Zn (green), and XRPD showed the main peaks for ZIF-8 and Pt, thereby confirming the formation of Janus Pt@ZIF-8 particle (**Figure 34**a,b). these particles were dropped onto the surface of an aqueous/ethanol solution containing sodium cholate and H_2O_2. The Pt@ZIF-8 moved, and its motion was recorded using optical microscopy. As shown in **Figure 34**c, the 8 µm-in-diameter particles behaved as motors, moving around the surface at a maximum speed of 1.65 $mm \cdot s^{-1}$ (measured using ImageJ software with 20 frames).

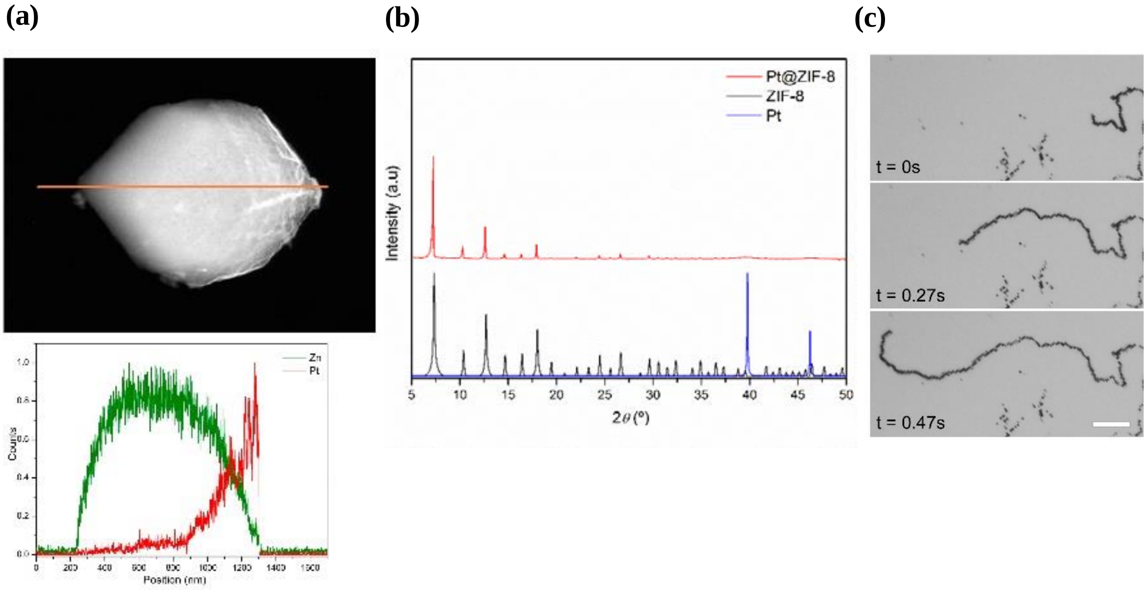

Figure 34. (a) Representative STEM-HAADF images and EDX composition analysis profile at 200 kV of Janus Pt@ZIF-8 (size = 1.3 µm ± 0.2 µm) particles, with 20 nm of Pt thickness. (b) XRPD patterns for the Janus Pt@ZIF-8 (size = 1.3 µm ± 0.2 µm), particles synthesized with a Pt thickness of 20 nm and compared with patterns of simulated ideal powder of ZIF-8 and Pt (lower). (c) Optical microscopy images revealing the movement sequence of a motorized Pt@ZIF-8 particle. Scale bar: 100 µm.

3. Conclusions

In conclusion, we have described a collection of monometallic and polymetallic Janus MOF particles fabricated by partially coating colloidal MOF crystals with the desired metal(s). We consider this approach to be a novel method for imparting new functionalities to MOFs, as evidenced by our preparation of asymmetrically functionalized MOFs, magnetically guidable MOFs and electrochemically motorized MOFs. Our findings should facilitate the development of MOFs for numerous practical applications, including drug delivery, theranostics, sensors, pollutant removals and catalysis.

4. References

1 A. Walther and A. H. E. Müller, *Chem. Rev.*, 2013, **113**, 5194–5261.

2 A. Walther and A. H. E. Muller, *Soft Matter*, 2008, **4**, 663–668.

3 Y. Yi, L. Sanchez, Y. Gao and Y. Yu, *Analyst*, 2016, **141**, 3526–3539.

4 G. Loget and A. Kuhn, *J. Mater. Chem.*, 2012, **22**, 15457–15474.

5 J. Hu, S. Zhou, Y. Sun, X. Fang and L. Wu, *Chem. Soc. Rev.*, 2012, **41**, 4356–4378.

6 F. Liang, C. Zhang and Z. Yang, *Adv. Mater.*, 2014, **26**, 6944–6949.

7 A. Perro, S. Reculusa, S. Ravaine, E. Bourgeat-Lami and E. Duguet, *J. Mater. Chem.*, 2005, **15**, 3745.

8 M. Lattuada and T. A. Hatton, *Nano Today*, 2011, **6**, 286–308.

9 A. H. Gröschel and A. H. E. Müller, *Nanoscale*, 2015, 11841–11876.

10 R. Erhardt, A. Böker, H. Zettl, H. Kaya, W. Pyckhout-Hintzen, G. Krausch, V. Abetz and A. H. E. Müller, *Macromolecules*, 2001, **34**, 1069–1075.

11 Liu, V. Abetz and A. H. E. Müller, *Macromolecules*, 2003, **36**, 7894–7898.

12 A. Walther, X. André, M. Drechsler, V. Abetz and A. H. E. Müller, *J. Am. Chem. Soc.*, 2007, **129**, 6187–6198.

13 C. Vilain, F. Goettmann, A. Moores, P. Le Floch and C. Sanchez, *J. Mater. Chem.*, 2007, **17**, 3509.

14 H. Takei and N. Shimizu, *Langmuir*, 1997, **13**, 1865–1868.

15 J. C. Love, B. D. Gates, D. B. Wolfe, K. E. Paul and G. M. Whitesides, *Nano Lett.*, 2002, **2**, 891–894.

16 S. Ye and R. L. Carroll, *ACS Appl. Mater. Interfaces*, 2010, **2**, 616–620.

17 A. M. Yake, C. E. Snyder and D. Velegol, *Langmuir*, 2007, **23**, 9069–9075.

18 Y. Gao and Y. Yu, *Langmuir*, 2015, **31**, 2833–2838.

19 O. Cayre, V. N. Paunov and O. D. Velev, *J. Mater. Chem.*, 2003, **13**, 2445–2450.

20 C. C. Ho, W. S. Chen, T. Y. Shie, J. N. Lin and C. Kuo, *Langmuir*, 2008, **24**, 5663–5666.

21 M. Lattuada and T. A. Hatton, *J. Am. Chem. Soc.*, 2007, **129**, 12878–12889.

22 X. Xu, N. L. Rosi, Y. Wang, F. Huo and C. A. Mirkin, *J. Am. Chem. Soc.*, 2006, **128**, 9286–9287.

23 F. Huo, A. K. R. Lytton-Jean and C. A. Mirkin, *Adv. Mater.*, 2006, **18**, 2304–2306.

24 S. U. Pickering, *J. Chem. Soc. Trans.*, 1907, **91**, 2001–2021.

25 H. Gu, Z. Yang, J. Gao, C. K. Chang and B. Xu, *J. Am. Chem. Soc.*, 2005, **127**, 34–35.

26 L. Hong, S. Jiang and S. Granick, *Langmuir*, 2006, **22**, 9495–9499.

27 H. Gu, R. Zheng, X. Zhang and B. Xu, *Extrapolation*, 2004, 5664–5665.

28 K.-W. Kwon and M. Shim, *J. Am. Chem. Soc.*, 2005, **127**, 10269–10275.

29 S. T. Selvan, P. K. Patra, C. Y. Ang and J. Y. Ying, *Angew. Chem. Int. Ed.*, 2007, **46**, 2448–2452.

30 P. Mulvaney, M. Giersig, T. Ung and L. M. Liz-Marzán, *Adv. Mater.*, 1997, **9**, 570–575.

31 T. Tanaka, M. Okayama, Y. Kitayama, Y. Kagawa and M. Okubo, *Langmuir*, 2010, **26**, 7843–7847.

32 A. Misra and M. W. Urban, *Macromol. Rapid Commun.*, 2010, **31**, 119–127.

33 J.-W. Kim, D. Lee, H. C. Shum and D. A. Weitz, *Adv. Mater.*, 2008, **20**, 3239–3243.

34 M. Yoshida, K.-H. Roh, S. Mandal, S. Bhaskar, D. Lim, H. Nandivada, X. Deng and J. Lahann, *Adv. Mater.*, 2009, **21**.

35 T. Nisisako, T. Torii, T. Takahashi and Y. Takizawa, *Adv. Mater.*, 2006, **18**, 1152–1156.

36 N. K. Sheridon, *patent*, 1978, **4**, 854.

37 N. K. Sheridon, E. A. Richley, J. C. Mikkelsen, D. Tsuda, J. M. Crowley, K. A. Oraha, M. E. Howard, M. A. Rodkin, R. Swidler and R. Sprague, *J. Soc. Inf. Disp.*, 1999, **7**, 141–144.

38 S. J. Ebbens and J. R. Howse, *Soft Matter*, 2010, **6**, 726–738.

39 R. Golestanian, T. B. Liverpool and A. Ajdari, *Phys. Rev. Lett.*, 2005, **94**, 220801.

40 B. Jurado-Sánchez, S. Sattayasamitsathit, W. Gao, L. Santos, Y. Fedorak, V. V. Singh, J. Orozco, M. Galarnyk and J. Wang, *Small*, 2015, **11**, 499–506.

41 Y. Zhu, H. Ohtani, M. L. Greenfield, M. Ruths and S. Granick, *Tribol. Lett.*, 2003, **15**, 127–134.

42 A. Kirillova, C. Schliebe, G. Stoychev, A. Jakob, H. Lang and A. Synytska, *ACS Appl. Mater. Interfaces*, 2015, **7**, 21218–21225.

43 A. Synytska, R. Khanum, L. Ionov, C. Cherif and C. Bellmann, *ACS Appl. Mater. Interfaces*, 2011, **3**, 1216–1220.

44 S.-H. Hu and X. Gao, *J. Am. Chem. Soc.*, 2010, **132**, 7234–7237.

45 P. Falcaro, R. Ricco, A. Yazdi, I. Imaz, S. Furukawa, D. Maspoch, R. Ameloot, J. D. Evans and C. J. Doonan, *Coord. Chem. Rev.*, 2016, **307**, **Part**, 237–254.

46 G. Lu, S. Li, Z. Guo, O. K. Farha, B. G. Hauser, X. Qi, Y. Wang, X. Wang, S. Han, X. Liu, J. S. DuChene, H. Zhang, Q. Zhang, X. Chen, J. Ma, S. C. J. Loo, W. D. Wei, Y. Yang, J. T. Hupp and F. Huo, *Nat. Chem.*, 2012, **4**, 310–316.

47 S. Yadnum, J. Roche, E. Lebraud, P. N??grier, P. Garrigue, D. Bradshaw, C.

Warakulwit, J. Limtrakul and A. Kuhn, *Angew. Chem. Int. Ed.*, 2014, **53**, 4001–4005.

48 J. He, Y. Liu, T. C. Hood, P. Zhang, J. Gong and Z. Nie, *Nanoscale*, 2013, **5**, 5151.

49 J. Cravillon, R. Nayuk, S. Springer, A. Feldhoff, K. Huber and M. Wiebcke, *Chem. Mater.*, 2011, **23**, 2130–2141.

50 J. Cravillon, C. a. Schröder, H. Bux, A. Rothkirch, J. Caro and M. Wiebcke, *CrystEngComm*, 2012, **14**, 492.

51 N. Yanai, M. Sindoro, J. Yan and S. Granick, *J. Am. Chem. Soc.*, 2013, **135**, 34–37.

52 G. Lu, C. Cui, W. Zhang, Y. Liu and F. Huo, *Chem. Asian J.*, 2013, **8**, 69–72.

53 K.-K. Yee, N. Reimer, J. Liu, S.-Y. Cheng, S.-M. Yiu, J. Weber, N. Stock and Z. Xu, *J. Am. Chem. Soc.*, 2013, **135**, 7795.

54 Q. Song, S. K. Nataraj, M. V Roussenova, J. C. Tan, D. J. Hughes, W. Li, P. Bourgoin, M. A. Alam, A. K. Cheetham and S. A. Al-Muhtaseb, *Energy Environ. Sci.*, 2012, **5**, 8359–8369.

55 T. Bae, J. S. Lee, W. Qiu, W. J. Koros, C. W. Jones and S. Nair, *Angew. Chemie Int. Ed.*, 2010, **49**, 9863–9866.

56 S. R. Venna and M. A. Carreon, *J. Am. Chem. Soc.*, 2009, **132**, 76–78.

57 L. Chen, Y. Peng, H. Wang, Z. Gu and C. Duan, *Chem. Commun. (Camb).*, 2014, 1–4.

58 T. Zhang, X. Zhang, X. Yan, L. Kong, G. Zhang, H. Liu, J. Qiu and K. L. Yeung, *Chem. Eng. J.*, 2013, **228**, 398–404.

59 U. P. N. Tran, K. K. A. Le and N. T. S. Phan, *ACS Catal.*, 2011, **1**, 120–127.

60 C.-H. Kuo, Y. Tang, L.-Y. Chou, B. T. Sneed, C. N. Brodsky, Z. Zhao and C.-K. Tsung, *J Am Chem Soc*, 2012, **134**, 14345–14348.

61 K. Hendrickx, D. E. P. Vanpoucke, K. Leus, K. Lejaeghere, A. Van Yperen-De Deyne, V. Van Speybroeck, P. Van Der Voort and K. Hemelsoet, *Inorg. Chem.*, 2015, **54**, 10701–10710.

62 L. Shen, R. Liang, M. Luo, F. Jing and L. Wu, *Phys. Chem. Chem. Phys.*, 2015, **17**, 117–121.

63 X. Zhu, J. Gu, Y. Wang, B. Li, Y. Li, W. Zhao and J. Shi, *Chem. Commun.*, 2014, 8779–8782.

64 A. D. Wiersum, E. Soubeyrand-Lenoir, Q. Yang, B. Moulin, V. Guillerm, M. Ben Yahia, S. Bourrelly, A. Vimont, S. Miller, C. Vagner, M. Daturi, G. Clet, C. Serre, G. Maurin and P. L. Llewellyn, *Chem. Asian J.*, 2011, **6**, 3270–3280.

65 L. Field and P. R. Engelhardt, *J. Org. Chem.*, 1970, **35**, 3647–3655.

66 S. Liu, Z. Xiang, Z. Hu, X. Zheng and D. Cao, *J. Mater. Chem.*, 2011, **21**, 6649.

Chapter 4

Synthesis of functional molecules@MOFs composites

1. Incorporation of functional molecules into the MOFs

The careful choice of the building blocks in the synthesis of Metal-Organic Frameworks (MOFs) has strongly contributed to their rapid development in the past 20 years. Over this period, a vast catalogue of MOFs with a great variety of structures and properties has been reported, which have been proposed for myriad applications such as gas sorption and catalysis. Beyond the improvements that an adequate design can induce in the MOF properties, the optimization and the presence of MOFs in new applications is also coming from their combination with other type of materials, thereby creating composites. As we reported in the first chapter of this manuscript, much efforts have been dedicated last years to the integration of the synthesis of composites based on MOF and metal nanoparticles (NPs), nanowires (NWs), quantum dots (QDs), carbon nanotubes (CNTs), oxides, nanofibers, polymers, polyoxometalates (POMs). The resulting MOF composites were synthesized through different approaches and showed an improvement in their properties for final applications.[1,2,3,4] We have also demonstrated in the previous chapter that for example Janus metal@MOF particles can be synthesized and used in different applications, for example the heavy metal removal. But new functionalities can also come by incorporating new active organic molecules in MOFs. These molecules can modify the physical environment of the pores and cavities within MOFs and tailor the properties, the chemical stability and/or reactivity of the framework. In this context, at least two different strategies have been employed to achieve MOF functionalization. The first approach aims to chemically modify MOFs after the crystalline materials have already been formed promoting a chemical reaction between the MOF and the molecule that we want to incorporate. The second involves the adsorption of functionalized molecules inside the pores of the MOFs. The MOFs are put in the presence of the desired molecules that is adsorbed in the channels (**Figure 1**).

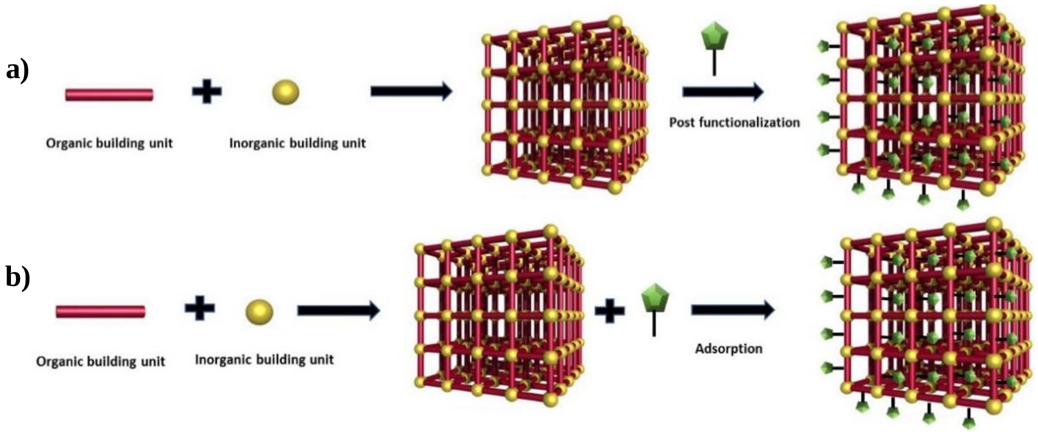

Figure 1 Schematic representation of the integration of functional molecules to the MOFs via: a) Post functionalization, b) Adsorption, and c) In situ.

1.1. Post synthetic modification of the MOFs by coordination interaction

In principle, there exists at least two different approaches for Post-synthetic modification (PSM) of MOFs with metal-ligand interaction. The first targets of the exposed metal sites of MOFs, whereas the second explores the coordination chemistry of the organic components. Several research groups have recently applied both approaches and demonstrated their utility and versatility in incorporating a variety of complex functionalities into the MOFs.

In MOFs structures auxiliary ligands or coordinated solvents could be detached from the metal ions nodes leading to the generation of coordinatively unsaturated metal centers able to coordinate new functional molecules in order to functionalize the MOF. In 1999, Williams *et al.* reported the well-known HKUST-1 compound, which is highly porous 3D MOF derived from dimeric Cu(II) paddle-wheel building units (SBUs) and BTC (1,3,5-benzentricalboxylate) ligands. Their study indicated that the lability of axial aqua ligands on the paddle-wheel SBU in HKUST-1 permits their replacement by other molecules. Treatment of the dehydrated HKUST-1 with dry pyridine, for example, resulted in a different formulation of the MOF, with pyridine as the new axial ligands. Interestingly, Williams et al. suggested that the pyridine-decorated HKUST-1 cannot be obtained directly from a reaction of C(II) salts, BTC, and pyridine.[5]

The creation of unsaturated metal ions was also extended to other MOFs. Férey *et al.* applied this approach in their materials MIL-100 and MIL-101, which are porous 3D MOFs constructed from Cr(III) trimers bridged by BTC and BDC (BDC=1,4-benzenedicaboxylate) ligands, respectively. In both MOFs, there are potential open metal sites at the Cr(III) trimers, which are occupied by water molecules in their as-synthesized forms. Férey and coworkers first studied how the water can be detached from the Cr(III) trimer. Then, the introduction of excess deuterated methanol to dehydrated MIL-100 sample at room temperature was sufficient to introduce the new axial ligands.[6] The same authors treated MIL-101 with a number of organic multifunctional amines such as ethylene-diamine (ED), diethylenetriamine (DETA), and 3-amino-propyltrialkoxysilane (APS).[7] They demonstrated, coupling infrared with x-ray and porosity studies that ED and DETA can be grafted to the Cr(III) cluster to produce the amine-grafted MIL-101, exhibiting the remarkably high activities in the Knoevenagel condensation. Amines were also used by Long *et al.* to improve the CO_2 adsorption profiles of MOF-74. They functionalized the framework by grafting of ED onto dehydrated Mg/DOBDC in anhydrous toluene under reflux for 12h to substantially improving its CO_2 adsorption properties at low and at ultradilute CO_2 partial pressures and increasing stability/regenarability.[8]

Beyond the use of unsaturated metallic clusters, the incorporation of unbound, and thereby available ligands into the organic components of MOF can also lead to the coordinative modification of MOFs. For example, Lin et al. designed a 3D homochiral porous MOF associating Cd(II) and a BINOL (BINOL = 1,10-bi-2-naphthol) type chiral bridging ligand that contains pyridyl and orthogonal dihydroxy functionalities. In this MOF while the pyridyl groups coordinate to the Cd(II) centers as part of the framework backbone, the dihydroxy substituents are not involved in coordinative interactions during the formation of the MOF and are therefore accessible for further chemical functionalization (PSM). Once the MOF was formed was treated with Ti(O´Pr)$_4$ a complex known to coordinate to BINOL (**Figure 2a**).[9] The authors used the resulting MOF for the heterogeneous asymmetric catalysis for the addition of diethylzinc to aromatic aldehydes to afford chiral secondary alcohols at up to 93% enantiomeric excess (ee). Control experiments with dendritic aromatic aldehydes of different sizes indicated that the heterogeneous asymmetric catalyst derived from the post functionalized MOF were both highly active and enantioselective as a result of the creation of readily accessible and uniform active catalyst sites inside the porous. PSM by coordination is not so exploited due to its difficulty, however, specific organic reactions ready tested has been reproduced and adapted to the PMS of the MOFs, as in the case of benzene rings that are able to react with this kind of active molecules (M(CO)$_3$ (M=Cr, Mo, W)) and to obtain active molecules on the MOF after the PSM. This PSM was carried out on IRMOF-1, which is a cubic lattice composed of octahedral Zn$_4$O(RCOO)$_6$ nodes bridged by linear BDC, and fragments (M(CO)$_3$) are known to bind to benzene rings and to generate arene organometallic ‘piano stool’ complexes (**Figure 2b**).[8]

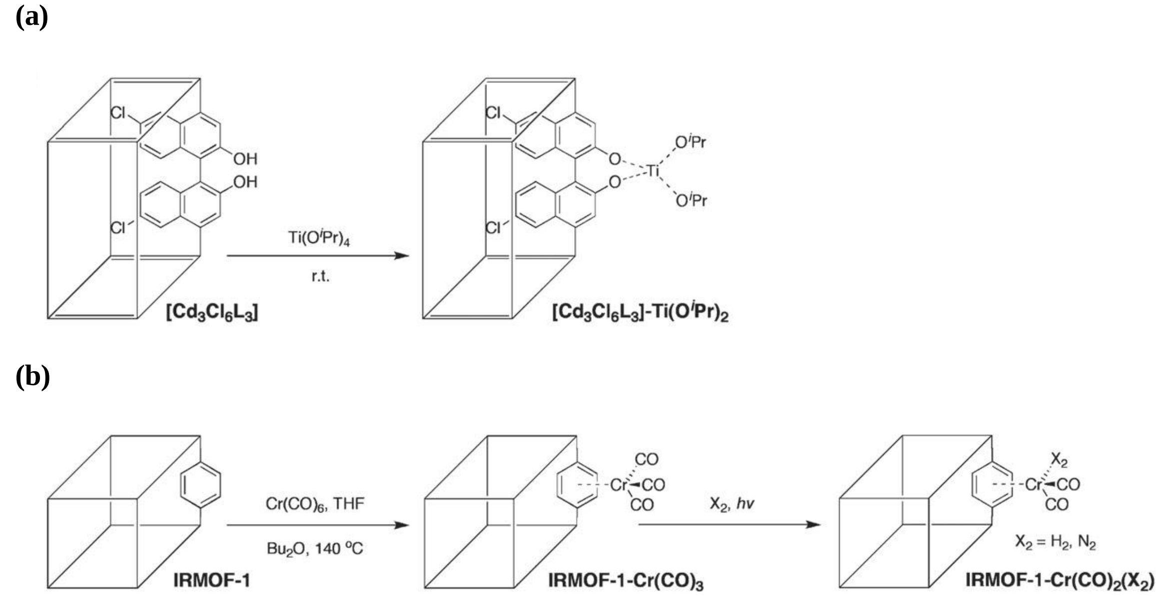

Figure 2 Scheme of the post synthetic modification of each of these MOFs with metal ion complexes.

Similarly, Cohen *et al*. carried out the PSM of one derivate of UiO-67, with bipyridyl moieties that incorporated ruthenium complex. The maximum coordinative post synthetic modification reached was 15%. Not in all PSM examples the authors show the percentage yield of the modification, but in this case the modification was around of 15% based on ruthenium (**Figure 3**).[10,11] The authors showed that this resulting UiO-67-Ru(bpy) shows efficient and recyclable catalytic activity for the aerobic oxidation of arylboronic acids under near-UV and visible light irradiation, and very recently Doonan *et al*. followed this metalation process by single crystal X-ray diffraction.[12] They sinthesized a new three-dimensional MOF possessing pore cavities that are lined with vacant di-pyrazole groups poised for post synthetic metalation, the [Mn_3(L)2(L′)(1)], where L and L′ are crystallographically unique forms of the deprotonated ligand bis (4-(4-carboxyphenyl)-1H-3,5-dimethylpyrazolyl)methane, LH_2. The metallations with different metal ions and $[Rh(CO)_2Cl]_2$ occur quantitatively without appreciable loss crystallinity, thereby enabling examination of the products by single-crystal diffraction. Furthermure, to illustrate the potential of this platform to garner fundamental insight into the metal catalysed reactions in porous solids the authors used single-crystal X-ray diffraction studies to structurally elucidate the reaction products of consecutive oxidative addition and methyl migration steps that occur within the pores of the Rh-metallated MOF, 1·$[Rh(CO)_2CL_2]$.

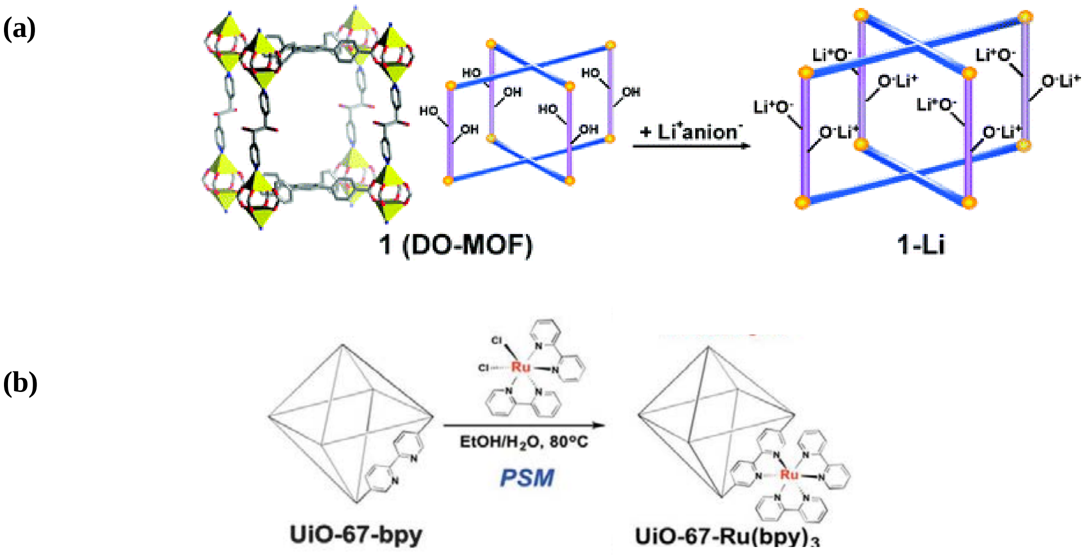

Figure 3. Scheme of the post synthetic modification by coordination of (a) DO-MOD and (b) UiO-67-Ru(bpy)3.

1.2. Post synthetic modification of MOFs by covalent bond

Synthetic methods that facilitate breaking and reforming covalent bonds represents the most powerful tool in modern synthetic chemistry. The covalent approach to the SPM may seem more challenging, when comparing the strength of covalent bonds relative to generally weaker coordinative interactions that sustain the MOF structure. However, the comparison of bonding strength may be true on individual basis, but the periodic architectures of MOFs can in fact afford remarkable thermal and chemical stability. The best proof of this statement is the large number of reports on the covalent modification of MOFs indicating that this approach is very powerful in MOF functionalization. Various types of covalent transformations, including amide coupling,[13] imine condensation,[14] urea formation,[15] N-alkylation,[16] bromination,[17] reduction,[18] click reactions,[19] and protonation[20] have been successfully applied to post synthetic MOFs modifications by a number of research groups.

The first example of covalent PSM of MOFs appeared in 2000 when Kim *et al.* reported a 2D homochiral MOF (POST-1).[21] The material was built from Zn(II) trimer SBU and an enantiopure tartrate derivative containing a pyridyl moiety. Although all the carboxylate groups coordinate to the Zn(II) trimers within the MOF, only half of the pyridyl units are engaged in coordinate bonding, with the other half exposed in the channels without any interaction with the framework metal ions, and that these free pyridyl groups were essential to the enantioselective catalytic activity of the MOF for the transesterification of 2,4-dinitrophenyl acetate by alkylation. Treatment of the crystalline, chiral MOF in DMF with excess CH_3I was shown to convert the free pyridyl groups to N-methylpyridinium ions. The MOF can be similarly modified by other reagents such as 1-iodohexane. Interestingly, in contrast to the unmodified MOF, the alkylated MOF showed very little catalytic activity for the same transesterification reactions, supporting the importance of free pyridyl groups for catalysis and confirming the successful PSM on the MOF (**Figure 4**a).

An interesting example of PSM by covalent interactions is the IRMOF-3, which is the amino-substituted version of IRMOF-1, and was chosen as a model system for the study of covalent PSM due to its highly porous, crystalline structure, and the presence of non-coordinating amino groups on the 2-aminobenzenedicarboxylate (NH_2–BDC) linker. The initial study focused on acetylation by targeting the amino groups of IRMOF-3 with acetic anhydride (**Figure 4**b).[22] In this case of MOF-LIC-1, after treating with ethylisocyanate, one of the amino groups was found to have transformed into urethane functionalities, while that the treatment with acetic acid under similar conditions led to formation of amide substituents on the same amino sites (**Figure 4**c).[23]

These examples with different MOFs showed the PSM by covalent interactions, and the flexibility that provide the free amine groups in to the MOFs to attach active molecules, in addition, the presence of the free aldehyde groups into the MOFs allow a post functionalization and the integration of active molecules, for example, the free aldehyde groups in ZIF-90 permits the covalent modification of ZIF-90 with ethanolamine via an imine condensation, as well was demonstrated the PSM of ZIF-90 by the reduction of the aldehyde to an alcohol functionality achieved by reacting ZIF-90 with $NaBH_4$ (**Figure 4**d).[24]

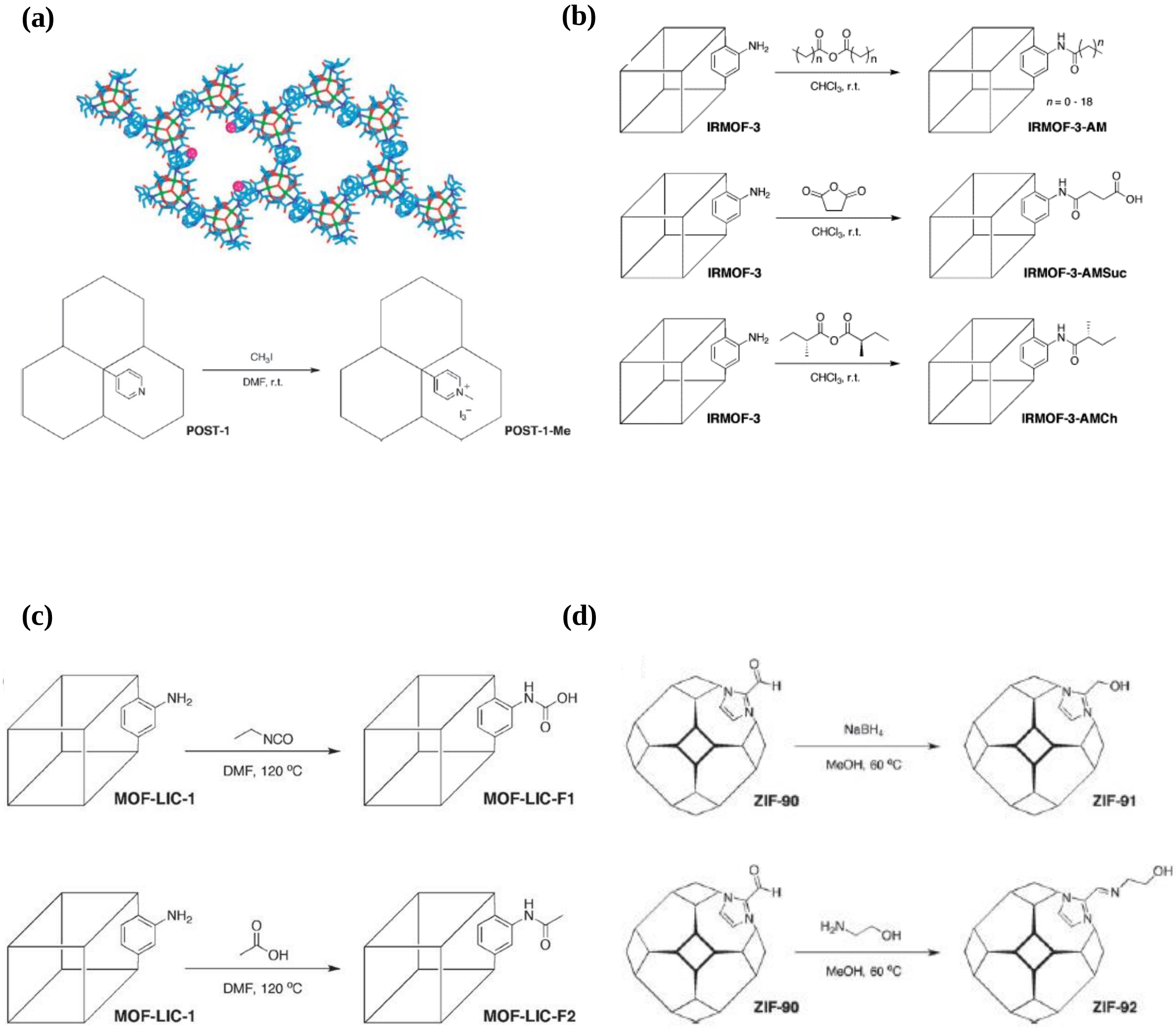

Figure 4. (a) Structural representations of POST-1 MOF (top); some sites of postsynthetic modification are highlighted with magenta spheres. Scheme of the postsynthetic modification (alkylation) of POST-1 (bottom). This example represents the earliest report of covalent postsynthetic modification of a MOF. (b) Scheme of representative postsynthetic modification reactions with IRMOF-3 and various anhydrides that have been performed and characterized. (c) Scheme of the postsynthetic modification reactions on MOF-LIC-1. (d). Scheme of the postsynthetic modification reactions for ZIF-90.

The MOFs involved in the PSM are chosen from their physical and chemical properties which can be potential to integrate active molecules for specific applications, for example, the immobilization of active molecules as DNA on the MOFs, this approach was developed by the PSM of UiO-66-N_3 and the DBCO functionalised DNA, the click reaction is between 2-N_3-1,4-bdc ligands of the MOF and DBCO-DNA, and showed the covalent PSM (**Figure 5**).[25] Biological active molecules are not the only interested to have in the MOFs, if not active molecules with response to an external field or at certain conditions for detection applications, for example, the integration of fluorescent active molecules in the MOFs by PSM through covalent bounds, in this address Fischer *et al.* provided evidence of surface selective PSM, when crystals of IRMOF-3 were reacted with the well-known biological tag Fluorescein IsoThioCyanate (FITC) (**Figure 5**).[26]

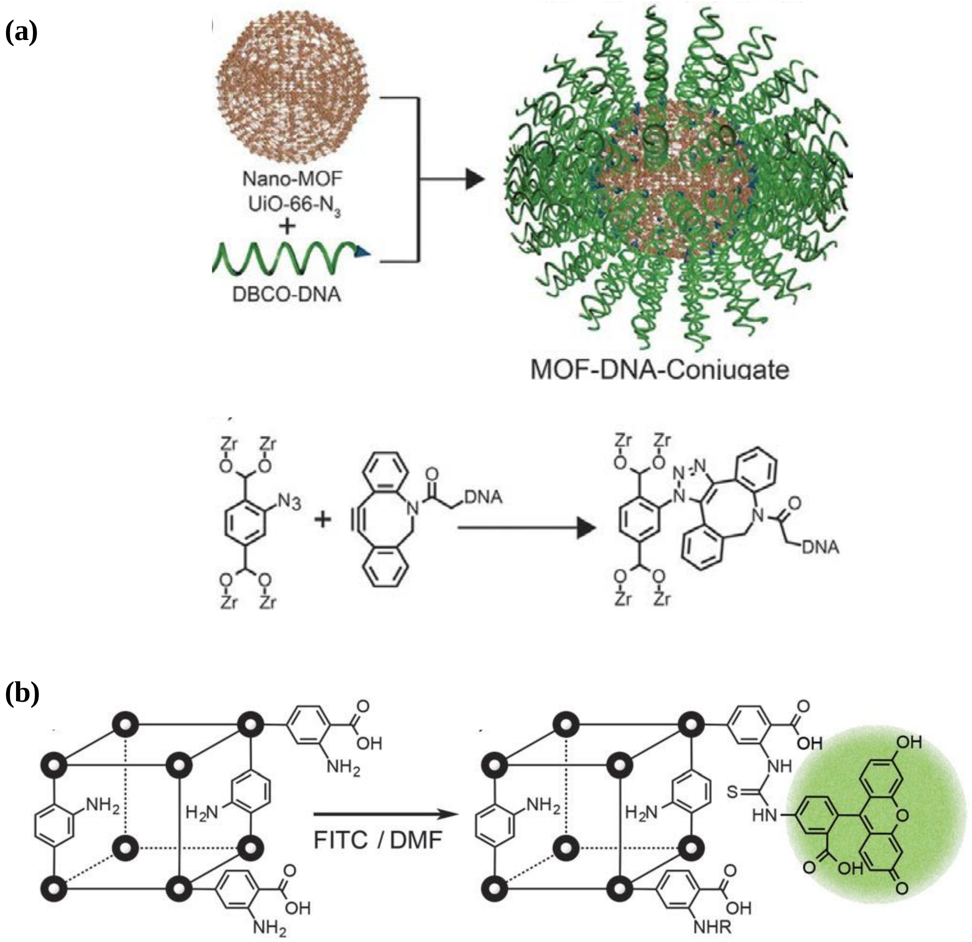

Figure 5. (a) Chemical structure of the strain-promoted click reaction between 2-N_3-1,4-bdc ligands of the MOF and DBCO functionalised DNA (b) Schematic of IRMOF-3, which can be surface functionalised. (b) at its amino groups, for example through bulky fluorescent FITC tagging.

The incorporation of active molecules in the MOFs by coordination and covalent bounds give the opportunities to integrate new functionalities of the MOFs by PSM, however, as we see, some key points as weak % yield of PSM, the stability and porosity of MOFs during PSM, take important place when the new functionalities look for close to real applications, in this sense, some strategies are prosed to keep the stability of the MOFs on this process, increasing the % yield and at the same time reduce the synthetic steps of PSM, and those strategies we will be detailed in the next section.

1.3. Adsorption of active molecules into the MOFs

MOF present voids that can physisorb external molecules if the initial guests (solvents) are removed. Removing guest species that occupy the free space of the lattice was detrimental to many earlier generation MOFs, and caused collapse of the frameworks; however, some systems were shown to maintain their crystallinity upon simultaneously exchange with other guests.

Lee *et al.* demonstrated that a 2D MOF based on 3-coordinated Ag(I) and tritopic 1,3,5-tris(3-ethynylbenzonitrile) benzene ligand could undergo a single-crystal-to-syngle-crystal transformation by partially releasing benzene guest upon heating at 110 ºC for 10 min. This process was reversible and the materials could reabsorb the same amount of benzene rather rapidly, indicating a zeolite-like behavior. Similar properties were also observed by Yaghi and co-workers in a 2D Co(II)BTC (BTC = 1,3,5-benzene-tricarboxylate) based MOF, which was stable upon loss of pyridine guests.[27] Quite significantly, the guest-free form of this latter MOF slectively absorbs aromatic molecules such as benzene, nitrobenzene, cyanobenzene, and chlorobenzene, but not acetonitrile, nitromethane, or dichloromethane. The laboratories of both kitagawa and Yaghi went a step further and independently confirmed the open framework structures of MOFs by using gas sorption isotherms. Their results unambiguosly established the true microporosity of MOF materials and largely responsible for initiating an exponential growth of studies on molecules absortion in porous MOFs.

Using the empty spaces created inside the channels different functionalities can be introduced in MOFs. Horcajada *et al.* had a great contribution in the field studying the adsorption of drugs into the MOFs, the structural influence of this encapsulation on the MOF, the study of the drug delivery.[28] In 2006 Horcajada *et al*, described the adsorption and delivery of a model analgesic and anti-inflammatory drug, Ibuprofen, by MIL-100 and MIL-101. Ibuprofen was adsorbed by the dehydrated powdered materials from a solution in hexane obtaining the active molecule (Ibuprofen) into the MOFs (**Figure 6**a).[28] After this pioneering work same authors extended the field to other MOFs and other drugs. They sued other MOFs as (MIL-53, MIL-58, MIL-100 and MIL-101) to incorporate drugs such as Busulfan, Azidothimidine triphosphate or Doxorubicin (**Figure 6**b).[29]

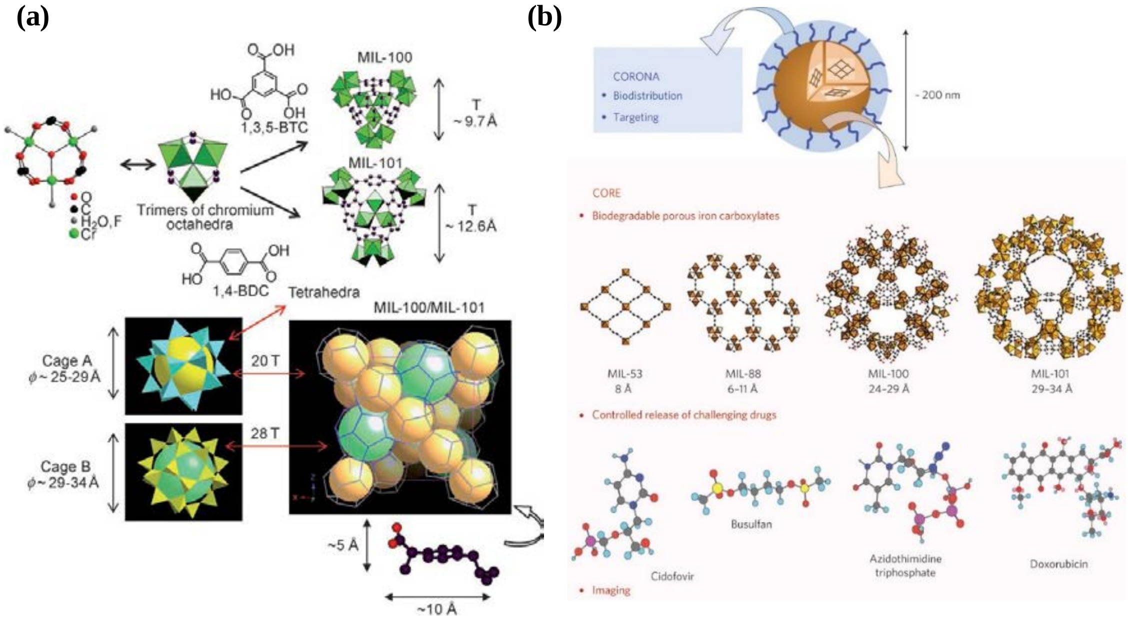

Figure 6. (a) Top: Schematic 3D representation of the tetrahedra (T) built up from trimers of chromium octahedra and 1,4-benzenedicarboxylate moieties or 1,3,5-benzenetricarboxylate groups in MIL-101 and MIL-100, respectively. Bottom: Schematic 3D representation of the mobil-39 (MTN) zeotype architecture of MIL-100 and MIL-101; left: the smaller A cages (yellow spheres with 20 T) and larger B cages (green spheres with 28 T); right: a unit cell (lines connect the T centers). (b) Scheme of engineered core–corona porous iron carboxylates for drug delivery and imaging.

The adsorption of some functional molecules can favour their activity as demonstrated by Ma *et al.* for example for enzymes. Enzymes as natural catalysts, feature high reactivity, selectivity, and specificity under mild conditions and contributing to green and sustainable processes in chemical, pharmaceutical, and food industries. Unfortunately, the use of enzymes for industrial applications has been hindered by their low operational stability, difficult recovery, and loss of activity under operational conditions. Immobilization of enzymes on a solid support can enhance their stability as well as facilitate ease of separation and recovery for reuse while maintaining activity and selectivity.[30,31] Ma *et al.* reported Tb-mesoMOF [$Tb_{16}(TATB)_{16}$] as an excellent platform for interaction between enzyme molecules and MOF pores.[32] Two nanoscopic cages of 3.9 and 4.7 nm in diameter are connected through pentagonal and hexagonal windows with diameters of 1.5 and 1.7 nm, respectively, which are large enough to allow the entry of microperoxidase-11 (MP-11) molecules and accommodate them in the mesopores of Tb-mesoMOF crystals (**Figure 7**a).

The adsorption of MP-11 was proven by the single crystal optical adsorption spectroscopy and a bathochromic shift of the encapsulated MP-11 in Tb-mesoMOF was observed (**Figure 7**b-c).[32]

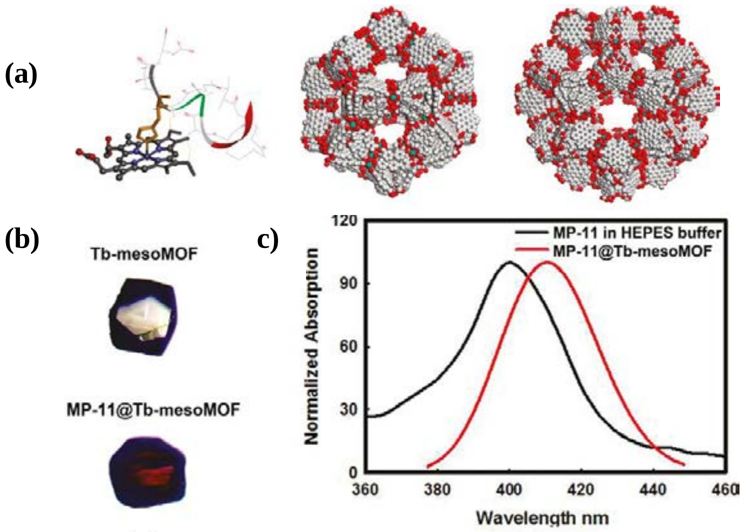

Figure 7. (a) Molecular structure of MP-11 and the nanoscopic cages in Tb-mesoMOF. (b) Optical images of Tb-mesoMOF and MP-11@Tb- mesoMOF. (c) Normalized single-crystal absorbance spectrum derived from specular reflectance for MP-11@Tb-mesoMOF (red) and solution optical spectrum for free MP-11 in buffer solution (black).

Yaghi and coworkers used a similar approach to the inmobilization/adsorption proteins on solids because it was of interest for biological applications. Furthermore, some studies demonstrated that the change of pH and salt concentrations strongly affects the electrostatic protein-support interactions and can lead to desorption of the protein.[33] Yaghi *et al.* immobilize proteins into IRMOF-74s with appropriate pore sizes specifically, vitamin B12 in IRMOF-74-IV, myoglobin (Mb) in IRMOF-74-VII, and green fluorescent protein (GFP) in IRMOF-74-IX (**Figure 8**).[34]

Vitamin-B12@IRMOF-74 Myoglobin@IRMOF-74-VI

MOP-18@IRMOF-74-V GFP@IRMOF-74-IX

Figure 8. Schematic representation of the active molecules in the series of IRMOF-74 (Vitamin-B12, mioglobyn, MOP-18 and GFP).

These, different examples show clearly that simply soaking MOF crystals in solution of a specific molecule can lead to a MOF with functionalized channels. Taking advantage of the simplicity of this method researchers absorbed a large panel of molecules, and functionalities on different MOFs. Thus many publications report the adsorption of dyes or molecules to capture heavy metals.[35,36,37,38]

Adsorption of various dyes in porous MOFs has been also investigated. Up to now, the adsorption of dye molecules has been established as a method to prove pore accessibility and to remove the dye pollutants.[39,40] For example, Rosi *et al.* reported the functionalization of the bio-MOF-1, $[Zn_8O(ad)_4(bpdc)_6\cdot 2Me_2NH_2]$ (ad; adeninate), by adsorption of the cationic pyridinium hemicyanine dye in an anionic bio-MOF-1, this adsorption was carried out by Chen *et al*, and they have presented a new two-photon-pumped micro laser based on the resultant dye into the bio-MOF-1, which exhibited two-photon fluorescence owing to the large absorption cross-section and the encapsulation-enhanced luminescence efficiency of the dye.[41] García *et al.* studied the adsorptive removal of azo-dye Orange II from aqueous solutions containing iron-benzenetricarboxylate (Fe(BTC)).[42] Another example is the Rhodamine B (RhB), which has been incorporated into the MOF-5 by adsorption, and its photoluminescence confirmed the existence of RhB in the pores of MOF-5. It showed strong fluorescence and obvious red-shift compared with RhB in $CHCl_3$. **Figure 9**a-b shows crystals before and after adsorption of rhodamine B.[43] Fluorescente properties was found as well in the adsorption of perylene into the ZJU-88, which showed a novel ratiometric thermometer and It can be used for physiological temperature sensing (**Figure 9**c).[44]

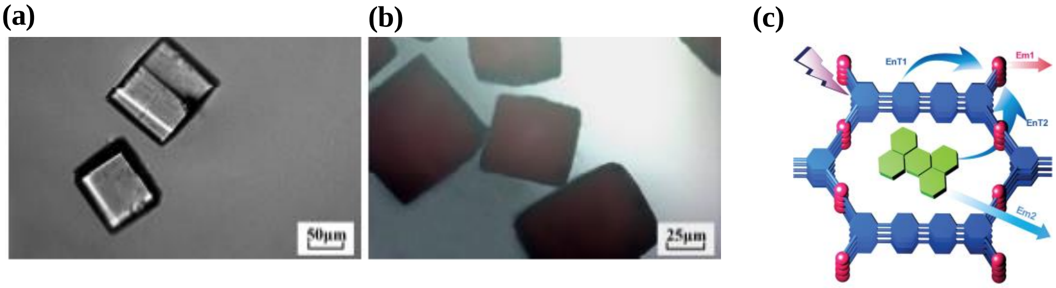

Figure 9. Optical micrographs of (a) MOF-5, (b) RhB@MOF-5, and (c) Design of dual-emitting perylene@ZJU-88 composite (EnT: energy transfer, Em: emission).

Matzger *et al*. demonstrated the adsorption of sulphur compounds and we will mention only for the adsorption of 4,6-dimethyldibenzothiophene (DMDBT) in different MOF; MOF-177, MOF-5, UMCM-150, HKUST-1, and MOF-505. In this study, for three of the five materials studied, the DMDBT adsorption capacity is larger at 300 ppmw-S. For example, UMCM-150 has capacities (g S/kg MOF, 300 ppmw S) 37 for DMDBT, and it was correlated that to larger guests lead to increased contact with the framework and this enhances interaction leading to higher adsorption for DMDBT. However, pore size was also a factor governing the adsorption capacity for a given organosulfur compound. For example, MOF-505, the MOF with the smallest pores studied, has its largest capacity at 300 ppmw S of 27 g S/kg for DMDBT, showing that DMDBT does not fit as well into the pores. These examples illustrate that MOFs are capable of readily removing the compound most challenging to eliminate by hydrodesulfurization thus making this an excellent complementary technique for the achievement of extremely low sulfur fuels (**Figure 10**a-e).[45] Latter, Mao et al. for example, reported adsorption isotherms of thiophene (T), benzothiophene (BT), and dibenzothiophene (DBT) in isooctane onto HKUST-1, and they were measured for (293.15 to 313.15) K and equilibrium sulfur concentrations up to 370 ppmw-S (ppmw of sulfur). The adsorption capacity followed the order of BT < T < DBT under the investigated sulfur concentrations and temperatures. The adsorption isotherms of T and DBT were highly favourable, and the isotherm data were well-correlated using a multitemperature Langmuir model, and it had a predictive ability for the adsorption of T, BT, and DBT within the sulfur concentration range and the temperature range studied (**Figure 10**f).[46]

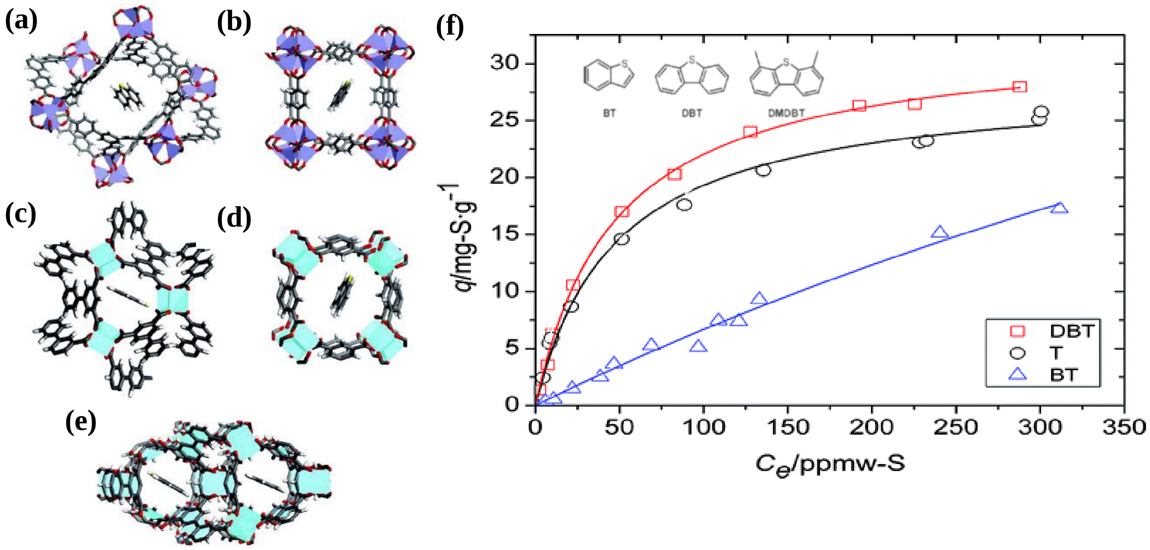

Figure 10. Crystal structures of (a) MOF-177 (b) MOF-5 (c) UMCM-150 (d) HKUST-1 (e) MOF-505 with one molecule of dibenzothiophene added in the pore of each MOF to represent scale. (f) Adsorption isotherms of T, BT, and DBT on HKUST-1: DBT at 295.15 K; T at 293.15 K; BT at 293.15 K; the solid lines are the Langmuir isotherm.

Recently Lin *et al.* reported the FITC@UiO-66 composite, where fluorescein isothiocyanate (FITC) is integrated into the network of UiO-66. In this case it represents a new class of nanosensors for intracellular pH sensing and provides an excellent tool for studying MOF-cell interactions (**Figure 11).**[47]

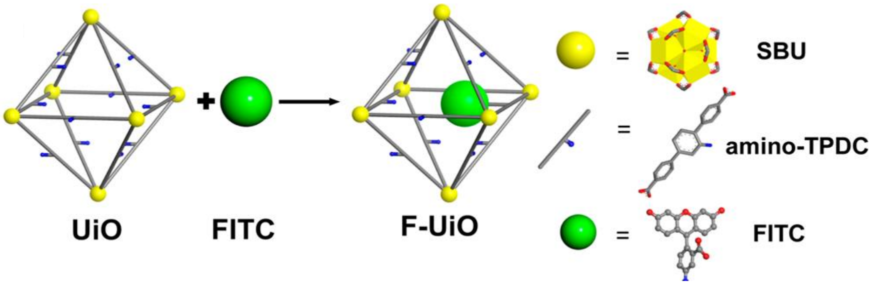

Figure 11. Schematic presentation of FITC@UiO composite.

Finally, Fujta et al. open very recently a new application of the absorption of functional molecules in MOF channels. They reported a protocol to determine the structure by single crystal X-ray diffraction of these molecules by absorbing them inside a MOF. In their method, tiny crystals of porous complexes were soaked in a solution of the target, such that the complexes can absorb the target molecules. Crystallographic analysis clearly determines the absorbed guest structures along with the host frameworks. In combination with other characterization techniques the reported protocol allows the direct characterization of multiple fraction, stablishing a prototypical means of liquid chromatography SCD analysis. The authors has been able to determine the structure of a scarce marine natural product.[48]

1.4. Incorporation of functional molecules to the MOFs via in situ

As we detailed above, the post synthetic functionalization of MOF is a powerfull approach to introduce new functionalities on MOFs. However, very recently, the embedment of external molecules in MOF situ during the synthesis have been envisaged. Similarly to the well known example of the encapsulation of inorganic nanoparticles in MOFs, this approach consists on mixing the guest molecule with MOF precursor to embed it in the resulting MOF crystals. This method has been called co-precipitation method.

The use of MOFs as molecular encapsulators takes advantage of the powerful confinement effect of MOFs, which is proposed as an efficient way to protect molecules from aggregation, heterogeneous distribution, and leaching.

For instance. Adhikari *et al.* recently reported the incorporation of drugs into the MOFs using the co-precipitation method.[49] The in situ formation of MOF-drug composites demonstrates high drug loading capacity compared to conventional methods. The authors used 1,3,5-Benzenetri-carboxylic acid (H_3BTC) as organic ligand and iron acetate and zinc nitrate as metal sources to synthesize Fe–BTC and Zn–BTC MOFs and incorporate Doxorubycin. This methodology is devoid of any extra steps for loading the drug after synthesis. Acoording to the author, the drug loading is also independent of pore size of the MOF as the drug molecules are embedded inside the MOF during their formation. Similarly, Falcaro *et al.* used the same strategy to encapsulate enzymes in ZIF-8 but using PVP as capping layer on enzyme to favour the ecapsulation.[50]

The use of this PVP revealed one of the possible limitation of this alternative strategy: the interaction between the MOF and guest. Indeed, the low attraction between the MOF and the guest could lead to low encapsulation efficiencies. For this reason, in our approach we try to adapt the co-precipitation method in order to guarantee higher encapsulation efficiencies. Our strategy tried to mix co-precipitation method and defect creation in MOFs.

In 2011, Behrens *et al.* showed that the use of modulators can affect the crystal growth of MOFs and lead to a bigger or smaller crystal. This occurs because they introduced molecules that can enter in competition with the used ligand to synthesis the MOF in coordination with metals. In this example Behrens *et al.* modulate growth of UiO-66, using acetic acid, benzoic acid, formic acid, all ligands that compete with benzenedicarboxylic acid. After this pioneering work many studies have been reported with the objective to define the role of the modulator, the effect on the crystal growth and in the final properties of the MOF. Behrens *et al.* demonstrated that the use of modulator lead to the formation of defective MOFs in which some of the metal clusters coordination spheres are surrounded, in addition to bridging ligands, by the molecules used as modulator. By consequence, in the final structure the creation of defects is accompanied by the presence on this external modulating agent.[51]

Thus, in this chapter we have explored the way to combine the co-precipitation method with the introduction of molecules that can act as modulator. More precisely, we used functional molecules that have carboxylic moieties to compete with the bridging ligand during the crystal growth process and other groups to introduce a new functionality in the MOF.

2. Incorporation of Xylenol Orange into the ZIF-8

In this Chapter the main objective was to incorporate Xylenol Orange (XO) inside a MOF. XO is an organic reagent, most commonly used as a tetrasodium salt as an indicator for metal titrations or as chelating agents. The molecules possess four carboxylic groups that can chelate metals. It turns from orange to purple color when is coordinated to metal.[52] Thus, XO is the perfect candidate to test our new approach because XO can simultaneously bind the metal cluster in the MOF and keep free carboxylic groups to chelate free heavy metals.

We initiated the study with the ZIF-8. In this case, the carboxylic groups from XO could bind to the free Zn ions into the ZIF-8 during the process of co-precipitation. **Figure 12**, shows a schematic representation of the expected interaction between XO and ZIF-8.

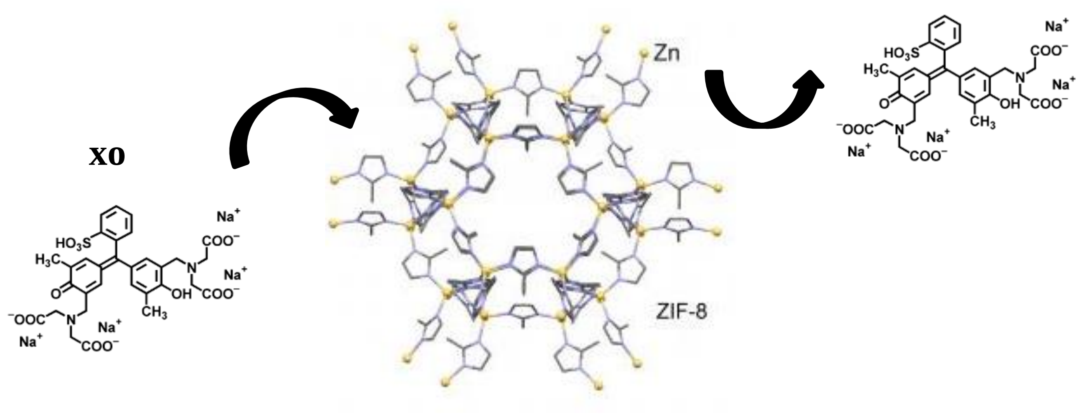

Figure 12. Schematic representation of Xylenol orange (3,3′-Bis[N,N-bis(carboxymethyl)aminomethyl]-o-cresolsulfonephthalein tetrasodium salt), and ZIF-8.

2.1. Synthesis of XO@ ZIF-8 composites

The synthesis of XO@ZIF-8 composites consisted on a mixture of the reactants of needed to synthesize ZIF-8 and different concentrations of XO. Six different synthesis were performed using 10 mg, 20 mg, 30 mg, 50 mg, 100 and 200 mg of Xylenol (Tabla 1).

Tabla 1 Screening of synthesis of XO@ZIF-8

Sample	**XO (mg)**	**2-mim (g)**	**$Zn(Ac)_2$ (g)**	**material (mg)**
a	10	1.12	0.3	301
b	20	1.12	0.3	295
c	30	1.12	0.3	285
d	50	1.12	0.3	263
e	100	1.12	0.3	250
f	200	1.12	0.3	160

More precisely, a solution of 0,3g (1.63 mM) of $Zn(OAc)_2$ is dissolved in 5 mL of H_2O, and it was added to a solution of 1,12 g (13.6 mM) of Hmim and X mg of Xylenol in 5 mL of H_2O. At this the solutions of XO turn from orange to purple indicating that the XO coordinate Zn^{2+}.[52] After 24 h a purple precipitate was recovered by centrifugation. To remove the unreacted Xylenol, the recovered precipitate was washed in H_2O and centrifugated repeatedly (15 times) until the supernatant become colourless, then rinsed with MeOH. The cleaned precipitate was then dried under reduced pressure at room temperature. Finally, we calculated the % yield of XO@ZIF-8 based on Zn^{2+} (Table 2).

Table 2 % yield of XO@ZIF-8 composites

Sample	**XO (mg)**	**Yield %**
a	10	100
b	20	98
c	30	95
d	50	87
e	100	83
f	200	53

Figure 13 Shows the representation of the resulting w% yield of XO@ZIF-8 (calculated in mg based on Zn) in function of the concentration of XO used in the synthesis. The increase of XO concentration in the synthesis lead to a decrease in the yield of XO@ZIF-8. Therefore, the plot shows clearly a high influence of the XO concentration in the synthesis of XO@ZIF-8. We can attribute this phenomena to the high chelating capacity of XO on Zn^{2+}.

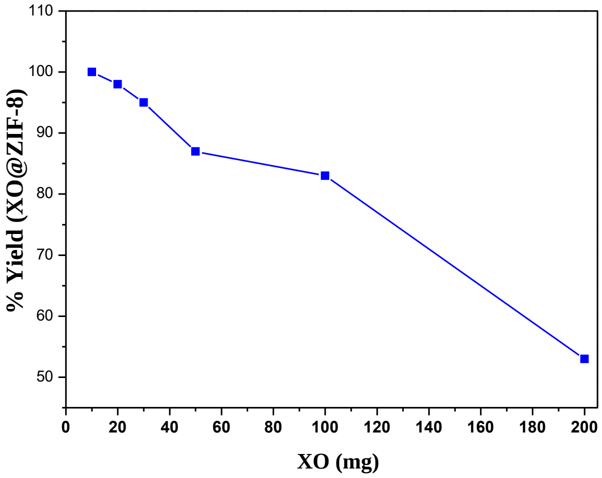

Figure 13. Representation of %yield of XO@ZIF-8 in function of XO using in the synthesis.

2.2. Characterization by FESEM of ZIF-8 and Xylenol@ZIF-8 composites

We evaluated the influence of the XO concentration in the morphology of XO@ZIF-8. The characterized powders showed a colour change from white (ZIF-8) to purple (XO@ZIF-8) (**Figure 14**) attributed to the presence of XO inside of ZIF-8 crystals. The FESEM images in **Figure 14**a showed that pristine ZIF-8 particles present a rhombic dodecahedra morphology as reported. When 10 mg of XO and 20 mg of XO are incorporated to the synthesis of ZIF-8 particles we observed the presence of truncated dodecahedra (**Figure 14**b-c). The presence of the truncated dodecahedra can be attributed to the partial etching of the ZIF-8 crystals provoked by the acidity of XO. This phenomenon was already reported When the amount of XO added increases the shape of the particles change dramatically. At 30 mg of XO, 50 mg of XO, and 100-200 mg of XO we observed the intergrowth of nanoscopic ZIF-8 crystals. We can infer that the excess of XO in the synthesis lead to the competition of XO and the Hmim for the formation of ZIF-8 crystals and increase the number of defects during the crystal growth of ZIF-8 the nucleation of ZIF-8 crystal limiting the formation of a dodecahedra morphology and increasing the number defects in ZIF-8 crystals that induce the growth of polycrystalline particles (**Figure 14**d-f).

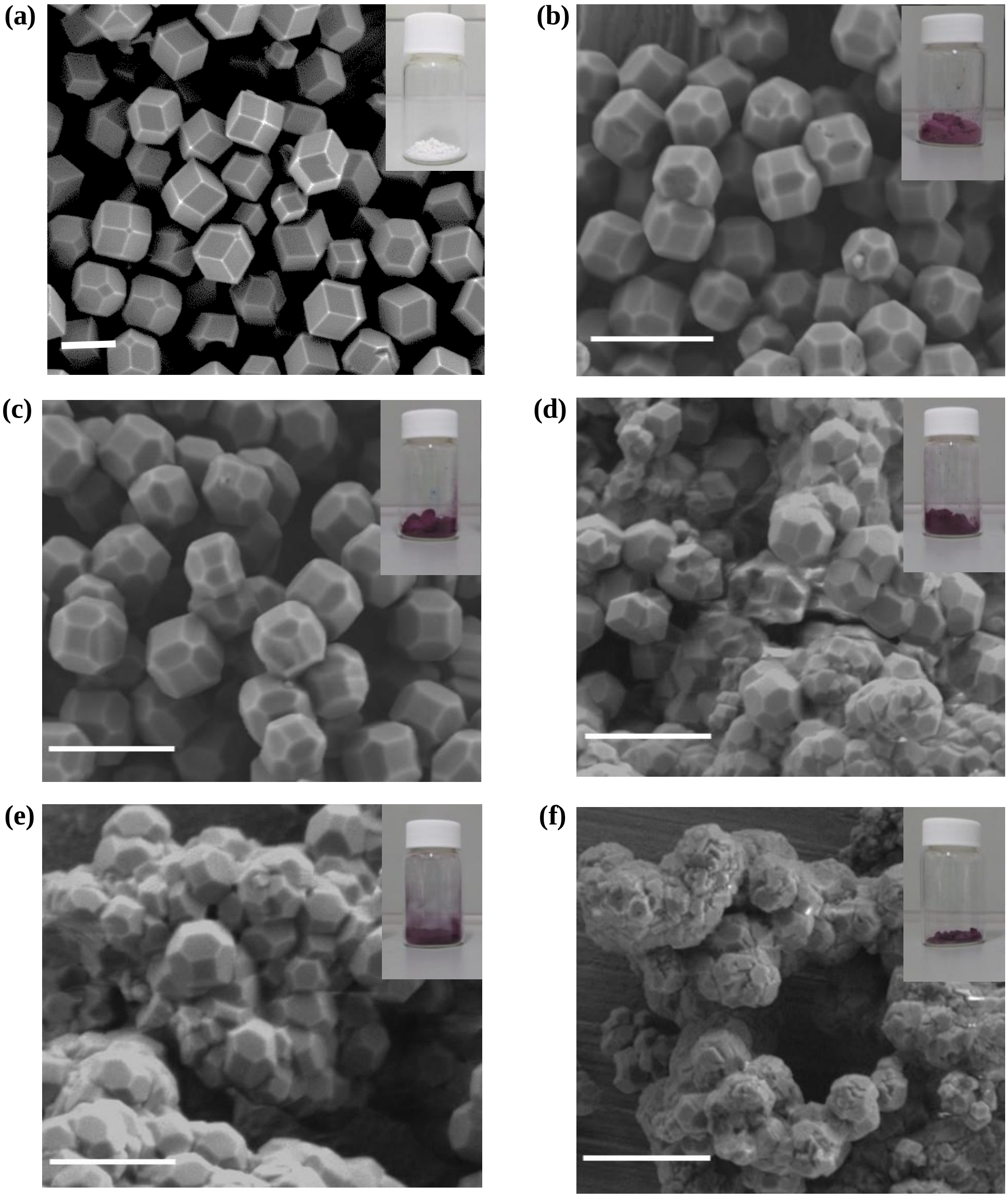

Figure 14. Representative FE-SEM images of the synthesized (a) ZIF-8, (b) XO@ZIF-8 (10mg XO), (c) XO@ZIF-8 (20mg XO), (d) XO@ZIF-8 (30mg XO), (e) XO@ZIF-8 (50mg XO), (f) XO@ZIF-8 (100-200 mg XO), scale bar; 1 µm.

2.3. Characterization by XRPD of ZIF-8 and XO@ZIF-8 composites

The crystallinity of the resulting composites was also evaluated in order to determine the quality of XO@ZIF-8. For this, ZIF-8 and the different XO@ZIF-8 samples were analysed by X-ray diffraction powder (XRPD), and compared to the simulated powder pattern from the crystalline structure of ZIF-8.[53]

The different powder patterns represented in **Figure 15** shows clearly that the position of the diffraction peaks of ZIF-8 (**Figure 14**b), and XO@ZIF-8 (**Figure 14**c-h) are in good agreement with the simulated powder pattern (**Figure 14**a). The main difference between the diffraction pattern of the different XO@ZIF-8 composites and ZIF-8 is the width of the diffraction peaks that is higher in the composites, and this is attributed to the excess of XO in the composites resulting in the introduction of defects on the ZIF-8 crystals that lead to crystal lattice imperfections, and we can infer that the crystalline structure of the composites is stable with different concentrations of XO incorporated in ZIF-8.

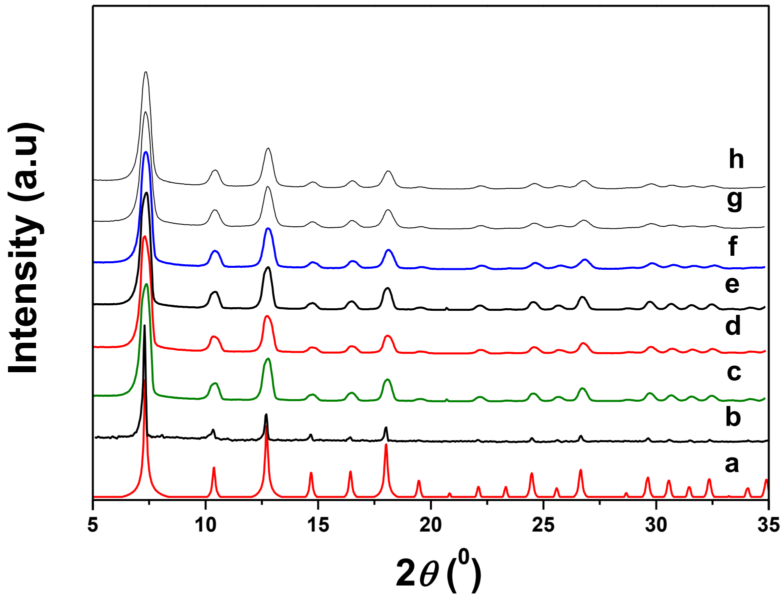

Figure 15. XRPD of (a) ZIF-8 pattern, (b) ZIF-8, (c) XO@ZIF-8 (10mg XO), (d) XO@ZIF-8 (20mg XO), (e) XO@ZIF-8 (30mg XO), (f) XO@ZIF-8 (50mg XO), (g) XO@ZIF-8 (100mg XO), and (h) XO@ZIF-8 (200mg XO).

2.4. Characterization by N_2 adsorption of XO@ZIF-8 composites

The adsorption capacity of the ZIF-8 is one of the main property that make it available for final applications, and taking into account that XO could limit the access to the ZIF-8 channels, we evaluated the effect of presence of XO by the nitrogen adsorption capacity of XO@ZIF-8. For this, we measured the N_2 adsorption and we determine the S_{BET} values.

All the XO@ZIF-8 composites showed a type I isotherm (**Figure 16**a-f**)**. The (S_{BET}) values; a) XO(10mg) 1525.027 m²/g, b) XO(20mg) 1477.952 m²/g, c) XO(30mg) 1423.099 m²/g, d)

XO(50mg) 1439.033 m^2/g, e) XO(100mg) 1470 m^2/g, and f) XO(200mg) 1450 m^2/g are in good agreement with previously reported BET values for ZIF-8 (≈ 1173 m^2/g,[54] 1600 m^2/g,[55,56] and 1700 m^2/g[57,53]). This indicates that even adding big amounts of XO in the ZIF-8 synthesis, the adsorption capacity of XO@ZIF-8 is not affected.

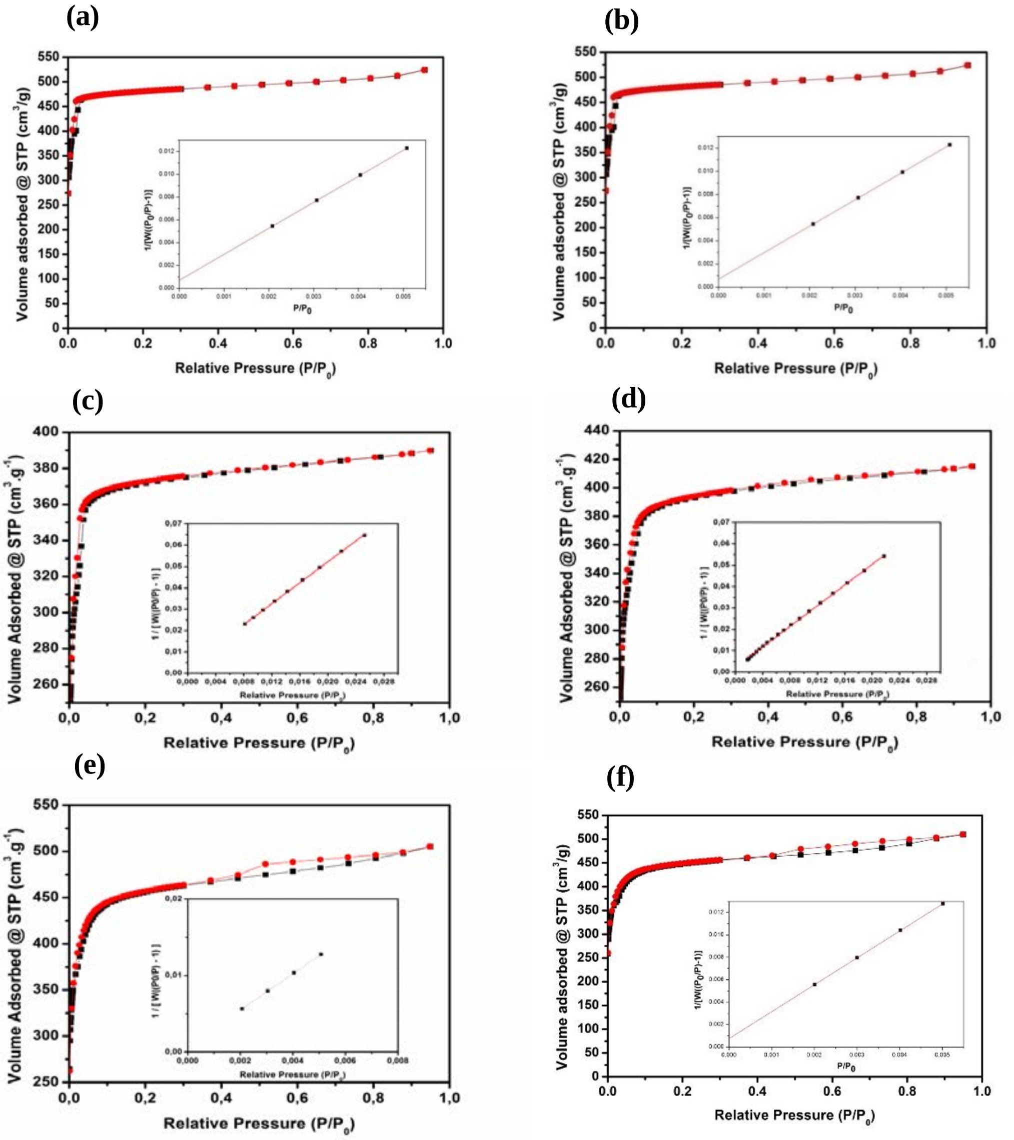

Figure 16. N_2 adsorption isotherms at 77 K and BET linear fit for a) Xo(10mg), b) Xo(20mg), c) Xo(30mg), d) Xo(50mg), e) Xo(100mg) and f) Xo(200mg).

2.5. Quantification of XO@ZIF-8 composites by UV-vis

Once the integrity of XO@ZIF-8 composites were confirmed, the next challenge consisted on determining the concentration of XO incorporated into the ZIF-8. Because the optical properties of XO we used UV-vis to determine the concentration of XO in the ZIF-8. We digest the different composites in acidic media and quantified the concentration of XO present in the composite. First, we prepared, a calibration curve of XO. The experiment was performed at constant acidic pH. Various concentrations of XO from 10 ppm to 50 ppm were prepared in aqueous solutions of 0.5% HNO_3. Finally, we recorded the absorbance for each sample by the UV-vis spectrophotometer and the calibration curve had a linear plot with a correlation coefficient of R=0.9999 (**Figure 17)**.

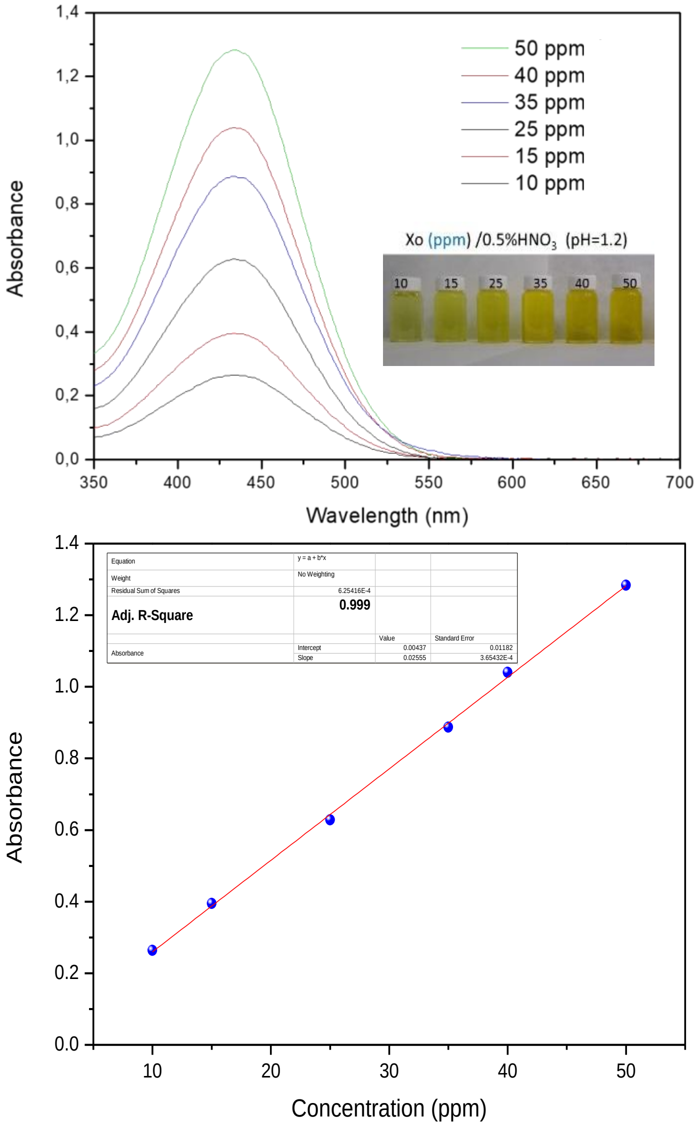

Figure 17. Calibration curve of XO and the linear plot.

Then, in order to know the concentration of XO in samples of XO@ZIF-8 composites, we digested the samples of XO@ZIF-8, then, the UV-vis spectra was recorded, the absorbance collected, and extrapolated in the calibration curve.

In this step, the digestion process consisted on dissolving the XO@ZIF-8 composite in acid (0.5% HNO_3) to dissolve the XO@ZIF-8 composite (**Figure 18**a**)**. The data for the calibration curve and the data for XO@ZIF-8 composite digested were collected under the same conditions. In this way, we could confidently draw inferences regarding the wavelength absorption of XO. Therefore, XO@ZIF-8 samples were diluted to be in the range of the calibration curve and finally they were measured by UV-vis (**Figure 18**b).

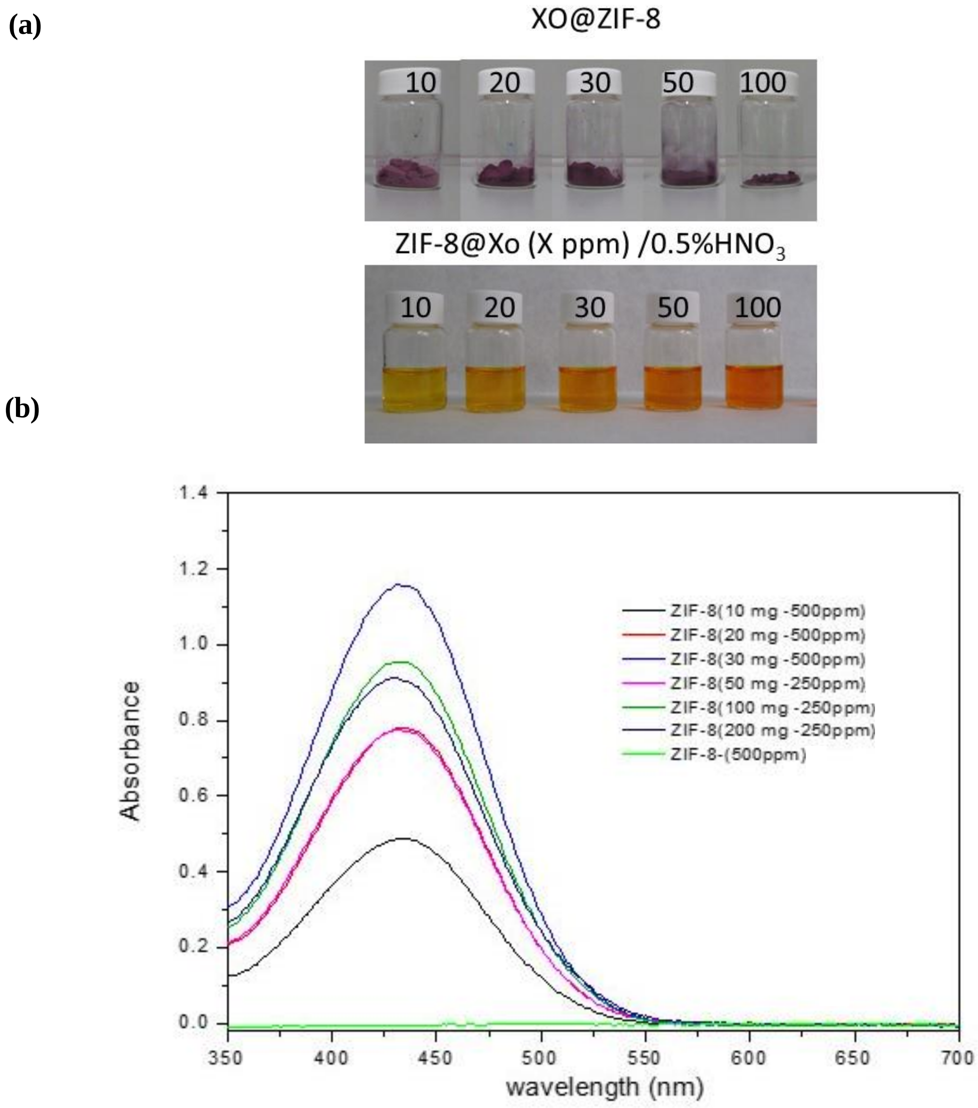

Figure 18. (a) Picture of XO@ZIF-8 before and after digestion, and (b) UV-vis spectra of XO@ZIF-8 from 10 to 100 mg of XO.

To ensure the accuracy of this method we digested twice the XO@ZIF-8 samples for reproducibility, and the recorded absorbance data were extrapolated in the calibration curve (**Figure 19**).

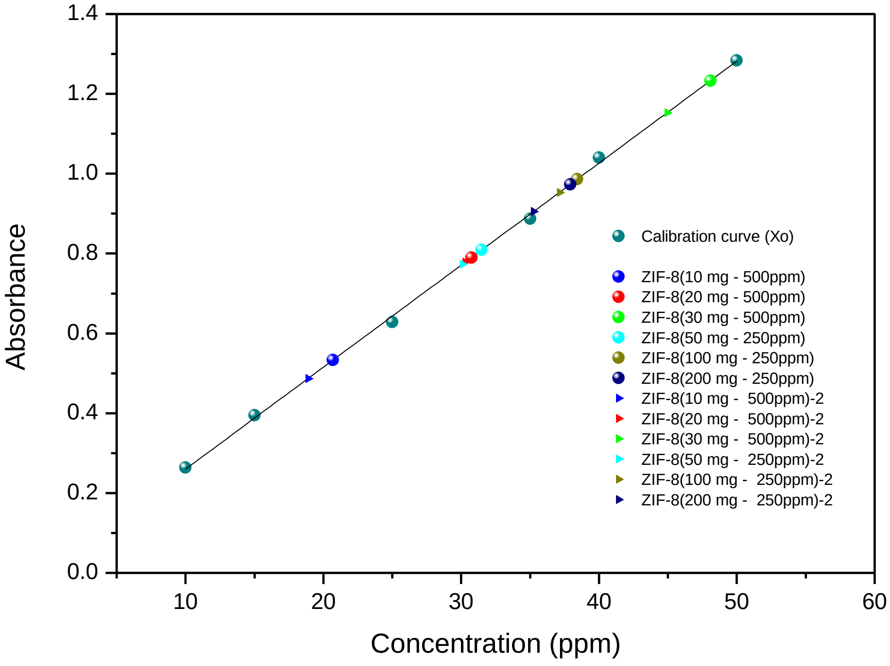

Figure 19. Extrapolated values for XO@ZIF-8 into the calibration curve.

Finally, the %XO incorporated in the XO@ZIF-8 composites were calculated from the concentrations of XO obtained by UV-vis (**Table 1).**

Table 1, %XO in XO@ZIF-8 composites

Sample	XO (mg)	% Xo in XO@ZIF-8
a	10	4
b	20	6
c	30	10
d	50	13
e	100	15
f	200	15

Finally, in order to select the best sample of XO@ZIF-8 for application in removal of heavy metal ions, we summarized the characterization information in (**Figure 20**)**.,** in which the percentage of XO in ZIF-8, the %yield of XO@ZIF-8 composite, and the milligrams of XO used in the synthesis are compared. The corresponding SEM images are inset (**Figure 20**).

In this plot (**Figure 20**), samples with 4% XO (10 mg XO) and 6% XO (20 mg XO) showed truncated dodecahedra morphology with an almost 100 % yield on the other hand, samples from 10% XO (30 mg XO), 13% XO (50 mg XO), and 15% XO (100 mg XO) into ZIF-8 show morphologic changes of ZIF-8, where these samples corresponds to the maximum amount of XO incorporated in ZIF-8, however, the morphology decrease when increasing the amount of XO into the ZIF-8. Therefore, the sample of 6 %XO (20 mg XO) into ZIF-8 was chosen as the best sample to measure the adsorption capacity of heavy metal ions. In this sample XO in ZIF-8 results in a high %yield XO@ZIF-8, a maximum %XO incorporated, a dodecahedral morphology, and an adsorption property of ZIF-8.

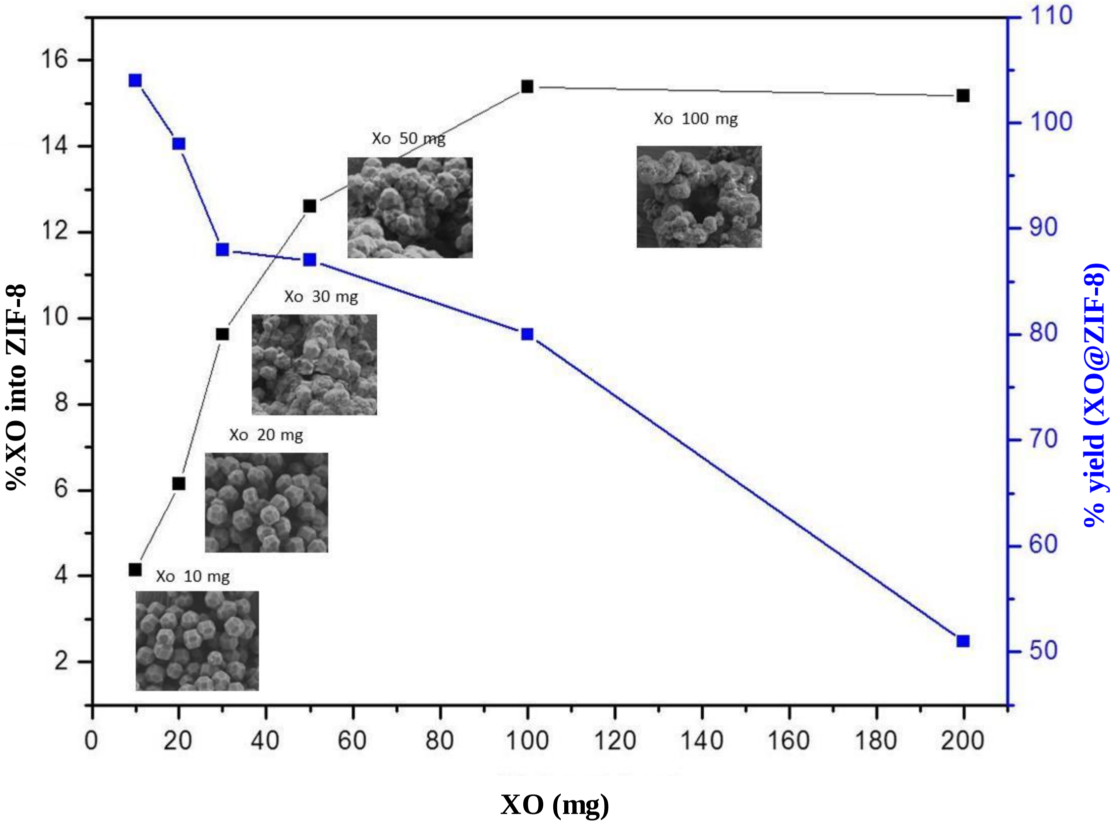

Figure 20. Representation of %XO in XO@ZIF-8 vs XO (mg), %Yield (XO@ZIF-8) vs XO (mg), and the inset SEM images.

2.6. Adsorption of Gd^{+3} by XO@ZIF-8 composite

The chemical bonds in Gadolinium-based contrast agents (GBCAs) are made of a gadolinium ion and a carrier molecule. A carrier molecule is called a chelating agent, which modifies the distribution of gadolinium within the body to overcome its toxicity while maintaining its contrast properties. These agents consist of a central paramagnetic Gd^{3+} chelated to a ligand to prevent direct toxicity by free Gd^{3+}. GBCAs are used intravenously to enhance the detail and clarity of diagnostic magnetic resonance imaging (MRI).

In the last years was believed that GBCAs are rapidly and completely excreted from the human body in an intact state. In recent years, however, there is a rapidly growing body of data that demonstrate that gadolinium accumulates in tissues (including brain, bone, and kidneys) of patients exposed to GBCAs during MRI. Retention of gadolinium increased in those who have repeated GBCA exposure, and they showed the onset of a series of symptoms (including neurological, musculoskeletal, and dermal). Regarding to these symptoms the U.S. FDA published a safety announcement in July 2015 that was investigated the risk of brain deposits associated with the repeated use of GBCAs in MRI.[58] Due to a lack of retrospective or prospective clinical cohort studies related to the association of post exposure medical conditions and recurrent GBCA exposure, the clinical significance of gadolinium tissue accumulation in patients without renal impairment is not fully known. Nonetheless, the potential for toxicity can be gleaned from published data of in vivo and in vitro studies of gadolinium toxicity, GBCA biochemistry, and differential gadolinium chelate stability.[59,60] However, the risk come from the fact when Gd^{3+} is released to the environment. Some studies in animals and humans have revealed that Gd^{3+} (free or chelated) is retained in a number of tissues in those without renal impairment.

One well-recognized factor related to the toxicity of Gd^{3+} is its size similarity and the resulting competition with Ca^{2+} in cellular and biochemical processes. It is capable of inhibiting stretch-activated and voltage-gated calcium channels. As such, Gd^{3+} can cause inhibition of vital physiologic processes associated with (but not limited to) muscle tissue and neurons.[61] In addition the free Gd^{3+} not only represents the risk after the exposure by MRI, if not also when the Gd^{+3} is released to the environment and is dissolved in water sources.

Therefore, alternatives to recover Gd^{3+} before to release to the environment could reduce the risk in a short and large time for the human health. For this reason, materials with the capacity of Gd^{+3} adsorption with a high stability and selectivity are needed. In this sense, we decided to study the Gd^{3+} adsorption in the XO@ZIF-8.

Our experiment consisted on determining the maximum Gd^{3+} adsorption capacity of XO@ZIF-8 composites Composite (25 mg of XO@ZIF-8) was immersed into a solution of Gd^{3+} with a high concentration of 2000 ppm. We start this high concentration in order to find when the composites reach the absorption saturation, each trial lasted for a distinct period of time: 0,5h, 1h, 2h, 4h, 8h, 12h, 24h, 48h, 72h, and 120h while stirring. After each period, the solids (XO@ZIF-8) were recovered by centrifugation and washed with methanol to remove the excess of Gd^{3+} attraped on the surface of the XO@ZIF-8 composites, and finally, the recovered solids were dried.

Once the solid separated from the supernatant, we observed that the supernatants showed color with different colors varying from pink to violet. (**Figure 21**). We attributed this to the partial decomposition of the XO@ZIF-8 (Gd^{3+} 2000 ppm/methanol). Indeed, at high concentration of Gd^{3+} the solution become acidic and degrade the composite it is not possible to specify values of pH because the solution is in methanol. For this reason, the XO@ZIF-8 composites under this condition is degraded and this process is different for each period of time of the Gd^{3+} adsorption process. The color changes in the supernatant could means that the XO is in a process of non-equilibrium system with a high concentration of Gd^{3+}, because in the first 24h the supernatant looks like a less purple color, this refers that XO is delivered from the XO@ZIF-8 and XO is coordinated with the free Gd^{3+} in the media, but as we know the ZIF-8 is one of the most easy system of MOF to synthesize, and their stability is weak in basic or acidic media, therefore, the ZIF-8 in any media reach to be in equilibrium in the system, for this if in the media there is Gd^{3+} at high concentrations, first happens the etching process of XO@ZIF-8, then the systems trends to be in equilibrium and the free XO could be incorporated into the etched XO@ZIF-8, describing a cycle of equilibrium-non equilibrium process, for this we assume that in the period of time between 48h and then 72 h, we found a clear supernatant which means that the XO has been incorporated into the ZIF-8 and finally, at 120 h with a less purple color of the supernatant could reach again to the non-equilibrium step and means that XO is being delivered to the media.

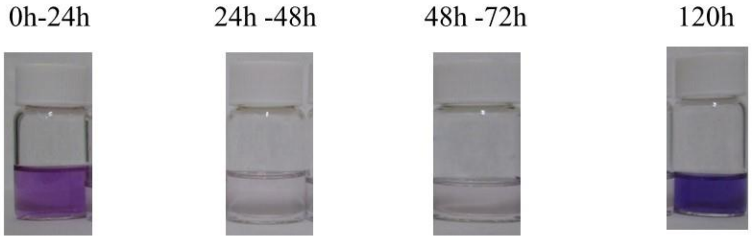

Figure 21. Representative images of supernatant of methanol, after adsorption [2000 ppm of Gd^{3+}] in XO@ZIF-8, in a period from 0h-120h.

To confirm this degradation, the different recovered solids of XO@ZIF-8 composites were analyzed by FESEM (**Figure 22**). FESEM images confirmed an aggressive etching of the ZIF-8 nanocrystals with the presences of attacked faces or holes.

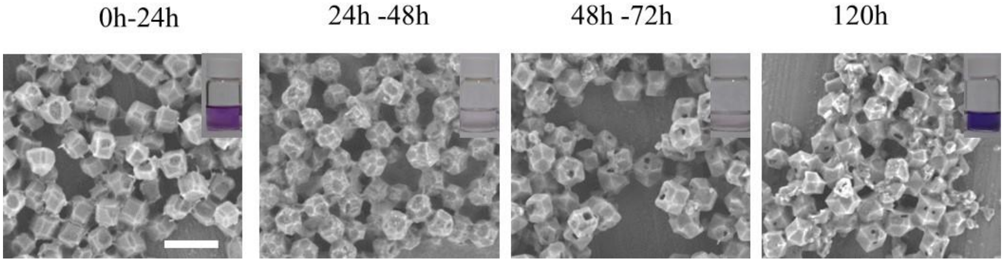

Figure 22. Representative SEM images of XO@ZIF-8 after adsorption [2000 ppm of Gd^{3+}] in a period from 0 h-120 h.

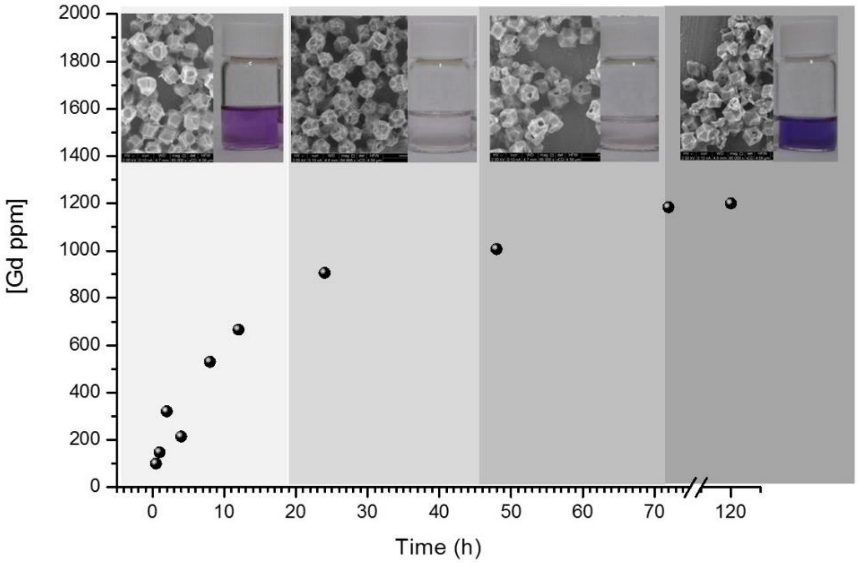

Figure 23. Plot of ICP analysis XO@ZIF-8 composites after Gd^{3+} adsorption process (2000 ppm/methanol), SEM and supernatants images.

In order to know if the XO@ZIF-8 composites had adsorbed Gd^{3+} besides the degradation process along Gd^{3+} adsorption, the recovered solids of XO@ZIF-8 composites were digested in 0.5% HNO_3 and analysed by ICP technique. The plott in **Figure 23** shows the resulting concentrations of Gd^{3+} adsorbed in the XO@ZIF-8 composite for each period of time of Gd^{3+} adsorption (0,5h, 1h, 2h, 4h, 8h, 12h, 24h, 48h, 72h, and 120h). The representative FESEM images, and the supernatant pictures after Gd^{3+} adsorption are also inset. The plot shows that Gd^{3+} adsorption is gradually increased over time, and the maximum adsorption of Gd^{3+} is 1200 ppm and it occurs from the 72h trial.

Although the results showed by ICP confirms that the adsorption of Gd^{3+} (2000 ppm) the degradation of composites lead us to work at lower concentrations and detect the maximum adsorption capacity of the XO@ZIF-8 maintaining the integrity of composites. In this sense was carried out a second attempt but decreasing the concentration of $Gd^{3+}$and fixing at 400 ppm in methanol. This test was carried out in a Gd^{3+} solution (400 ppm/methanol) for each period of time; 0,5h, 1h, 2h, 4h, 8h, 12h, 24h, 48h, and 72h under stirring.

In this second attempt to measure the adsorption capacity of XO@ZIF-8 composite in Gd^{3+} solution we observed that the recovered supernatants after solid separation by centrifugation were transparent (**Figure 24**), and we assumed that at relatively lower concentration of Gd^{3+} does not effect of the media, resulting that XO@ZIF-8 composites are stable in this adsorption condition and keeping the integrity of the XO@ZIF-8 composites along the Gd^{3+} adsorption process. Then, the recovered solids were digested in 0.5% HNO_3 and analysed by ICP technique.

Figure 24 shows the inset SEM images of XO@ZIF-8 composites after adsorption process, and reveals that the composite keeps the integrity of the morphology. The plot shows a maximum adsorption capacity of 400 ppm at 72h for XO@ZIF-8 composites. These results showed that XO@ZIF-8 composites under Gd^{3+} adsorption at 400 ppm are stable.

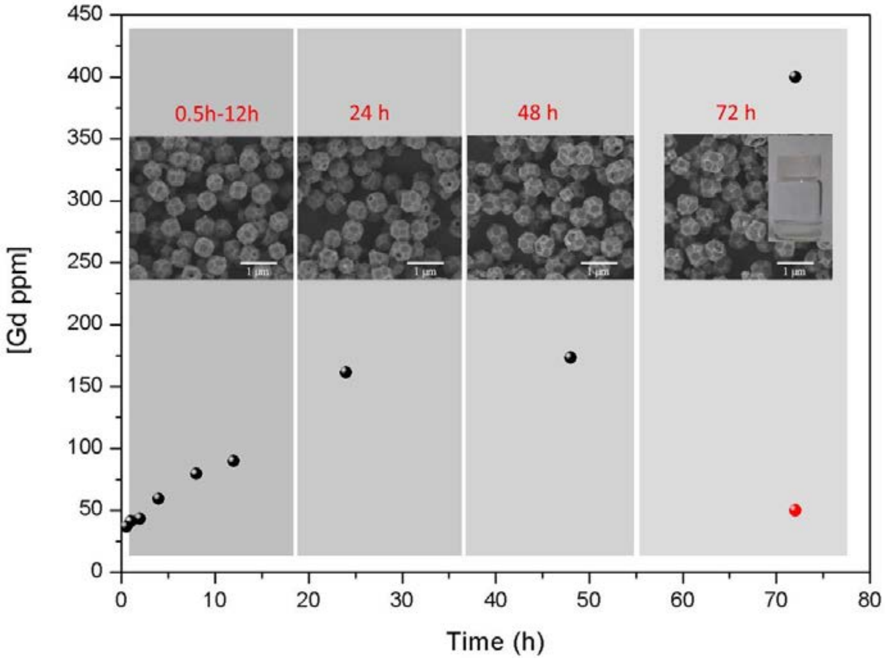

Figure 24. Adsorption of Gd^{3+} (400 ppm) in function of time, and the inset SEM images of solids and supernatant pictures after a period, XO@ZIF-8 (black dot) and ZIF-8 (red dot).

The samples of XO@ZIF-8 composites after Gd^{3+} adsorption (after 0.5h and 72h) were measured by XRPD **(Figure 25)**. The diffractogram shows clearly that the diffraction peaks of ZIF-8 and XO@ZIF-8 are in good agreement with the simulated powder pattern confirming the structural integrity of XO@ZIF-8 composites after Gd^{3+} adsorption process at 400 ppm.

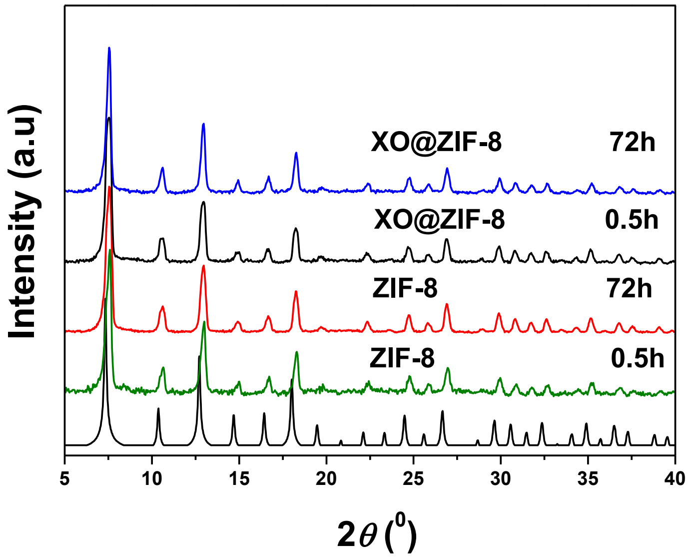

Figure 25. XRPD patterns of ZIF-8 and XO@ZIF-8 composites after Gd^{3+} adsorption for 0.5h and 72h.

2.7. Conclusions

In conclusion, the approach to in situ synthesis of ZIF-8 with XO as an auxiliary ligand was achieved by incorporation of XO the synthesis from 10 mg to 100 mg.

Once the screening of composites was synthesized, the best sample with the main properties of ZIF-8 was kept.

As a proof of concept, the XO@ZIF-8 (6%XO) composite was tested as means of heavy metal ion removal. The Gd^{3+} adsorption was carried out and showed that the maximum Gd^{3+} [400 ppm / methanol] adsorption is at 72h while maintaining the stability XO@ZIF-8 (6%XO) composite throughout the adsorption process.

2.8. Rereferences

1 J. Aguilera-Sigalat and D. Bradshaw, *Coord. Chem. Rev.*, 2016, **307**, **Part**, 267–291.

2 R. Ricco, L. Malfatti, M. Takahashi, A. J. Hill and P. Falcaro, *J. Mater. Chem. A*, 2013, **1**, 13033.

3 Q.-L. Zhu and Q. Xu, *Chem. Soc. Rev.*, 2014, **43**, 5648–5512.

4 S. Li and F. Huo, *Nanoscale*, 2015, **7**, 7482–7501.

5 S. S. Y. Chui, S. M. F. Lo, J. P. H. Charmant, a G. Orpen and I. D. Williams, *Science.*, 1999, **283**, 1148–1150.

6 A. Vimont, J.-M. Goupil, J.-C. Lavalley, M. Daturi, S. Surblé, C. Serre, F. Millange, G. Férey and N. Audebrand, *J. Am. Chem. Soc.*, 2006, **128**, 3218–3227.

7 Y. K. Hwang, D.-Y. Hong, J.-S. Chang, S. H. Jhung, Y.-K. Seo, J. Kim, A. Vimont, M. Daturi, C. Serre and G. Férey, *Angew. Chem. Int. Ed. Engl.*, 2008, **47**, 4144–4148.

8 S. S. Kaye and J. R. Long, *J. Am. Chem. Soc.*, 2008, **130**, 806–807.

9 C.-D. Wu, A. Hu, L. Zhang and W. Lin, *J. Am. Chem. Soc.*, 2005, **127**, 8940–8941.

10 X. Yu and S. M. Cohen, *Chem. Commun.*, 2015, **51**, 9880–9883.

11 K. L. Mulfort, O. K. Farha, C. L. Stern, A. a Sarjeant and J. T. Hupp, *J Am Chem Soc.*, 2009, **1**, 1–19.

12 J. D. Evans, C. J. Sumby and C. J. Doonan, *Chem. Soc. Rev.*, 2014, **43**, 5933–5951.

13 Z. Wang and S. M. Cohen, *Chem. Soc. Rev.*, 2009, **38**, 1315–1329.

14 A. H. Chughtai, N. Ahmad, H. A. Younus, A. Laypkov and F. Verpoort, *Chem. Soc. Rev.*, 2015, **44**, 6804–6849.

15 E. Dugan, Z. Wang, M. Okamura, A. Medina and S. M. Cohen, *Chem. Commun.*, 2008, 3366–3368.

16 F. M. Hinterholzinger, *Doctoral*, 2013, 243.

17 S. J. Garibay, Z. Wang, K. K. Tanabe and S. M. Cohen, *Inorg. Chem.*, 2009, **48**, 7341–7349.

18 W. Morris, C. J. Doonan, H. Furukawa, R. Banerjee and O. M. Yaghi, 2008, 12626–12627.

19 W. Zhu, C. He, X. Wu and C. Duan, *Inorg. Chem. Commun.*, 2014, **39**, 83–85.

20 Z. Wang and S. M. Cohen, *Chem. Soc. Rev.*, 2009, **38**, 1315.

21 J. S. Seo, D. Whang, H. Lee, S. I. Jun, J. Oh, Y. J. Jeon and K. Kim, *Nature*, 2000, **404**, 982–986.

22 Z. Wang and S. M. Cohen, *J Am Chem Soc*, 2007, **129**, 12368–12369.

23 J. S. Costa, P. Gamez, C. A. Black, O. Roubeau, S. J. Teat and J. Reedijk, *Eur. J. Inorg. Chem.*, 2008, **2008**, 1551–1554.

24 W. Morris, C. J. Doonan, H. Furukawa, R. Banerjee and O. M. Yaghi, *J. Am. Chem. Soc.*, 2008, **130**, 12626–12627.

25 W. Morris, W. E. Briley, E. Auyeung, M. D. Cabezas and C. A. Mirkin, *J. Am. Chem. Soc.*, 2014, **136**, 7261–7264.

26 M. Ma, A. Gross, D. Zacher, A. Pinto, H. Noei, Y. Wang, R. A. Fischer and N. Metzler-Nolte, *CrystEngComm*, 2011, **13**, 2828–2832.

27 O. M. Yaghi, G. Li and H. Li, *Nature*, 1995, **378**, 703–706.

28 P. Horcajada, C. Serre, M. Vallet-Regí, M. Sebban, F. Taulelle and G. Férey, *Angew. Chemie - Int. Ed.*, 2006, **45**, 5974–5978.

29 P. Horcajada, T. Chalati, C. Serre, B. Gillet, C. Sebrie, T. Baati, J. F. Eubank, D. Heurtaux, P. Clayette, C. Kreuz, J.-S. Chang, Y. K. Hwang, V. Marsaud, P.-N. Bories, L. Cynober, S. Gil, G. Ferey, P. Couvreur and R. Gref, *Nat. Mater.*, 2010, **9**, 172–178.

30 Q.-L. Zhu and Q. Xu, *Chem. Soc. Rev.*, 2014, **43**, 5468–5512.

31 X. Lian, Y. Fang, E. Joseph, Q. Wang, J. Li, S. Banerjee, C. Lollar, X. Wang and H.-C. Zhou, *Chem. Soc. Rev.*, 2017, **46**, 3386–3401.

32 V. Lykourinou, Y. Chen, X. Sen Wang, L. Meng, T. Hoang, L. J. Ming, R. L. Musselman and S. Ma, *J. Am. Chem. Soc.*, 2011, **133**, 10382–10385.

33 D. S. Raja, W.-L. Liu, H.-Y. Huang and C.-H. Lin, *Comments Inorg. Chem.*, 2015, **35**, 331–349.

34 O. M. Y. Hexiang Deng, Sergio Grunder, Kyle E. Cordova, Cory Valente, Hiroyasu Furukawa, Mohamad Hmadeh, Felipe Gándara Adam C. Whalley, Zheng Liu, Shunsuke Asahina, Hiroyoshi Kazumori, Michael O'Keeffe, Osamu Terasaki, J. Fraser Stoddart, *Science.*, 2012, **336**, 1018–1023.

35 T. Song, J. Yu, Y. Cui, Y. Yang and G. Qian, *Dalt. Trans.*, 2015, 4218–4223.

36 Q.-R. Fang, G.-S. Zhu, Z. Jin, Y.-Y. Ji, J.-W. Ye, M. Xue, H. Yang, Y. Wang and S.-L. Qiu, *Angew. Chemie Int. Ed.*, 2007, **46**, 6638–6642.

37 H.-N. Wang, F.-H. Liu, X.-L. Wang, K.-Z. Shao and Z.-M. Su, *J. Mater. Chem. A*, 2013, **1**, 13060–13063.

38 M.-J. Dong, M. Zhao, S. Ou, C. Zou and C.-D. Wu, *Angew. Chemie Int. Ed.*, 2014, **53**, 1575–1579.

39 Y.-Q. Lan, H.-L. Jiang, S.-L. Li and Q. Xu, *Adv. Mater.*, 2011, **23**, 5015–5020.

40 H. K. Chae, D. Y. Siberio-Perez, J. Kim, Y. Go, M. Eddaoudi, A. J. Matzger, M. O'Keeffe and O. M. Yaghi, *Nature*, 2004, **427**, 523–527.

41 J. Yu, Y. Cui, H. Xu, Y. Yang, Z. Wang, B. Chen and G. Qian, *Nat. Commun.*, 2013, **4**, 1–7.

42 E. Rojas-García, R. López Medina, M. May-Lozano, I. Hernández-Pérez, I. Hernández Pérez, M. Valero and A. Maubert-Franco, *Materials.*, 2014, **7**, 8037–8057.

43 H. J. Wang and G. S. Zhu, *Adv. Mater. Res.*, 2011, **345**, 245–249.

44 Y. Cui, R. Song, J. Yu, M. Liu, Z. Wang, C. Wu, Y. Yang, Z. Wang, B. Chen and G. Qian, *Adv Mater*, 2015, **27**, 1420–1425.

45 K. a. Cychosz, A. G. Wong-Foy and A. J. Matzger, *J. Am. Chem. Soc.*, 2008, **130**, 6938–6939.

46 B. Liu, Y. Zhu, S. Liu and J. Mao, *J. Chem. Eng. Data*, 2012, **57**, 1326–1330.

47 C. He, K. Lu and W. Lin, *J. Am. Chem. Soc.*, 2015, **12**, 19–22.

48 Y. Inokuma, S. Yoshioka, J. Ariyoshi, T. Arai, Y. Hitora, K. Takada, S. Matsunaga, K. Rissanen and M. Fujita, *Nature*, 2013, **501**, 262–262.

49 C. Adhikari and A. Chakraborty, *ChemPhysChem*, 2016, **17**, 1070–1077.

50 K. Liang, R. Ricco, C. M. Doherty, M. J. Styles, S. Bell, N. Kirby, S. Mudie, D. Haylock, A. J. Hill, C. J. Doonan and P. Falcaro, *Nat. Commun.*, 2015, **6**, 7240.

51 A. Schaate, P. Roy, A. Godt, J. Lippke, F. Waltz, M. Wiebcke and P. Behrens, *Chem. – A Eur. J.*, 2011, **17**, 6643–6651.

52 B. J. Colston and V. J. Robinson, 1997, **122**, 1451–1455.

53 K. S. Park, Z. Ni, A. P. Cote, J. Y. Choi, R. Huang, F. J. Uribe-Romo, H. K. Chae, M. O'Keeffe and O. M. Yaghi, *Proceeding Natl. Sci. Acadaemy*, 2006, **103**, 10186–10191.

54 Y. Pan, Y. Liu, G. Zeng, L. Zhao and Z. Lai, *Chem. Commun. (Camb).*, 2011, **47**, 2071–3.

55 M. Casco, Y. Cheng, L. L. Daemen, D. Fairen-Jimenez, E. V. Ramos Fernandez, A. J. Ramirez-Cuesta and J. Silvestre-Albero, *Chem. Commun.*, 2016, 3639–3642.

56 C. Liu, F. Sun, S. Zhou, Y. Tian and G. Zhu, *Cryst. Eng. Comm.*, 2012, **14**, 2–4.

57 T. Tian, M. T. Wharmby, J. B. Parra, C. O. Ania and D. Fairen-Jimenez, *Dalt. Trans.*, 2016, **45**, 6893–6900.

58 FDA, *https://www.fda.gov/Drugs/DrugSafety/ucm455386.htm*, 2015, 7–10.

59 T. Grobner, *Nephrol. Dial. Transplant.*, 2006, **21**, 1104–1108.

60 H. Blasco-Perrin, B. Glaser, M. Pienkowski, J. M. Peron and J. L. Payen, *Pancreatology*, 2017, **13**, 88–89.

61 M. Rogosnitzky and S. Branch, *BioMetals*, 2016, **29**, 365–376.

Conclusions

The main objective of this thesis has been the exploration of new methodologies to synthesis new MOF based composites and combine in a same material the intrinsic porosity related properties of MOFs and other functionalities coming from other materials such as magnetism, fluorescence or metal capture.

The first part of the thesis, have been focused on the synthesis of MOF based Janus particles using the desymmetrization at surfaces approach. This methodology, used to functionalize inorganic nanoparticles and create Janus nanoparticles, consists on the deposition of nanoparticles monolayers on a surface and the further evaporation on the exposed face of the deposited crystals of a layer of metal. We have demonstrated the versatility of this approach combining different MOFs (ZIF-8, UiO-66) with different metals (Gold, Cobalt, Platinum) and creating new Janus Particles composites that can be selectively functionalized by fluorescent molecules or catalytically propelled in aqueous solution improving heavy metal capture. The work done during this thesis open new avenues on designing and synthesizing multifunctional composites.

Once demonstrated the capacity to functionalize selectively MOF with metallic layers, the second part of the thesis has been dedicated to exploring a new way to incorporate functional molecules inside the MOF creating defects. The idea consists on using coordinative functional molecules that promote the formation of defects occupying coordination sites of the bridging ligands. The validity of the methodology has been demonstrated integrating the chelating agent Xylenol Orange into the MOF (ZIF-8). The Gd^{3+} removal capacity of the resulting composites have been evaluated showing very promising results. We expect that this strategy can be extended to other molecules and MOFs to create new multifunctional composites.

In conclusion, in this Thesis we have explored two new strategies to design and synthesise multifunctional MOF based composites imparting new functionalities to MOFs and opening avenues in new applications.